



LASER-INDUCED BREAKDOWN  
SPECTROSCOPY ON SOLUTION SAMPLES  
USING SURFACE EXCITATION

THESIS

Leonard M. Berman, Captain, USAF

AFIT/GAP/ENP/96D-03

DISTRIBUTION STATEMENT A

Approved for Public Release  
Distribution Unlimited

DEPARTMENT OF THE AIR FORCE  
AIR UNIVERSITY

**AIR FORCE INSTITUTE OF TECHNOLOGY**

Wright-Patterson Air Force Base, Ohio

19970122 121

DEPARTMENT OF THE AIR FORCE  
AIR UNIVERSITY

**AFIT/GAP/ENP/96D-03**

**LASER-INDUCED BREAKDOWN  
SPECTROSCOPY ON SOLUTION SAMPLES  
USING SURFACE EXCITATION**

**THESIS**

**Leonard M. Berman, Captain, USAF**

**AFIT/GAP/ENP/96D-03**

**Approved for public release; distribution unlimited**

### **Disclaimer Statement**

The views expressed in this thesis are those of the author and do not reflect the official policy or position of the Department of Defense or the U. S. Government.

**AFIT/GAP/ENP/96D-03**

**LASER-INDUCED BREAKDOWN  
SPECTROSCOPY ON SOLUTION SAMPLES  
USING SURFACE EXCITATION**

**THESIS**

**Presented to the Faculty of the Graduate School of Engineering  
of the Air Force Institute of Technology  
Air University in Partial Fulfillment  
of the Requirements for the  
Degree of Master of Science in Applied Physics**

**Leonard M. Berman, A.A.S, B.S.**

**Captain, USAF**

**December 1996**

**Approved for public release; distribution unlimited**

LASER-INDUCED BREAKDOWN  
SPECTROSCOPY ON SOLUTION SAMPLES  
USING SURFACE EXCITATION

Leonard M. Berman, A.A.S., B.S.

Captain, USAF

Approved:

  
Paul J. Wolf

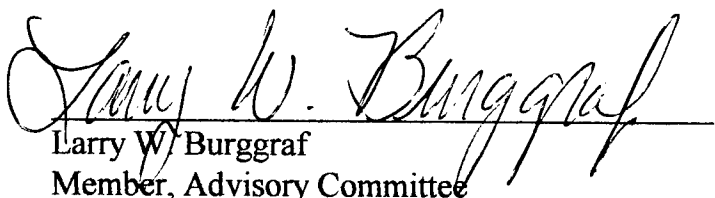
21 Nov 96

Paul J. Wolf, Lt Col, USAF  
Chairman, Advisory Committee

  
Glen P. Perram

21 Nov 96

Glen P. Perram, Major, USAF  
Member, Advisory Committee

  
Larry W. Burggraf

21 Nov 96

Larry W. Burggraf  
Member, Advisory Committee

## **Acknowledgements**

I would like to take this time and thank those people who have made this thesis possible. Without their talent and dedication, I might have not made it this far. The library staff were especially helpful in locating large volumes of obscure data. The laboratory technicians, Jim Reynolds, Greg Smith, and Belinda Johnson, always went that extra mile to help me out. My thesis committee members, Major Glen Perram and Dr. Larry Burggraf, were always there to lend a ear and point me in the right direction when I had gone astray. Additionally, I'd like to thank my thesis advisor, Lt Col Paul Wolf, who never questioned my abilities even when I had second thoughts. This thesis would not have been possible without his help.

Moreover, I would like to thank the U.S. Army Corps of Engineers at the Waterways Experiment Station in Vicksburg, MS. They generously provided the financial support needed for this research. With their help, we were able to purchase the necessary equipment/supplies in order to carry out this study.

Finally, I want to thank my parents, Israel and Arlene Berman, and Felix and Irene St. Louis, for their constant support. They have always been a rock that I could lean upon. I am truly blessed for all the love and encouragement they have given me throughout the years.

Leonard M. Berman

## Table of Contents

	<b>Page</b>
Acknowledgments . . . . .	iii
List of Figures . . . . .	vi
List of Tables . . . . .	x
Abstract . . . . .	xi
I. Introduction . . . . .	1
1.1 Overview . . . . .	1
1.2 Problem Foundation . . . . .	2
1.3 Research Objectives . . . . .	3
1.4 Sequence of Presentation . . . . .	3
II. Literature Review . . . . .	4
2.1 Background . . . . .	4
2.2 Theory Behind the Experiment . . . . .	6
2.3 Previous Work in the Field . . . . .	11
III. Experimental Design and Methodology . . . . .	20
3.1 Instrumentation . . . . .	20
3.2 Sample Preparation . . . . .	25
IV. Results . . . . .	27
4.1 Nickel in Solution (IR Excitation at 1064 nm) . . . . .	27
4.2 Nickel in Solution (UV Excitation at 355 nm) . . . . .	34
4.3 Pure Solvent Detection (UV Excitation) . . . . .	38
4.4 Saturated Solvent Detection (UV Excitation) . . . . .	45

V. Discussion . . . . .	.49
5.1 General . . . . .	.49
5.2 Nickel in Solution. . . . .	.51
5.3 Pure Solvent Detection . . . . .	.53
5.4 Saturated Solvent Detection . . . . .	.62
VI. Conclusions and Recommendations . . . . .	.65
Appendix A: Area/Noise Ratios. . . . .	.67
Appendix B: Systematic Error . . . . .	.68
Appendix C: Determination of Noise (N) at Various Concentrations . . . . .	.69
Appendix D: Spectra for Solvents Tested . . . . .	.70
Appendix E: Bond Dissociation Energy . . . . .	.91
References . . . . .	.92
Vita . . . . .	.97

## List of Figures

<b>Figure</b>	<b>Page</b>
3.1 Schematic of Experimental Apparatus . . . . .	21
3.2 Timing of the System . . . . .	24
4.1 Ni (1g/l - IR) at 50 $\mu$ s Gate Width and 8 $\mu$ s Time Delay . . . . .	27
4.2 Deionized Water (IR) at 50 $\mu$ s Gate Width and 8 $\mu$ s Time Delay . . . . .	29
4.3 Ni (1g/l - IR) at 50 $\mu$ s Gate Width and 4 $\mu$ s Time Delay . . . . .	30
4.4 Ni (1g/l - IR) at 50 $\mu$ s Gate Width and 1 $\mu$ s Time Delay . . . . .	30
4.5 S/N Ratio Versus Time Delay at 352.45 nm. . . . .	32
4.6 Calibration Curve for Ni (IR) at 352.45 nm . . . . .	33
4.7 Ni (1g/l - UV) at 10 $\mu$ s Gate Width and 3 $\mu$ s Time Delay. . . . .	34
4.8 Ni (1g/l - UV) at 10 $\mu$ s Gate Width and 1 $\mu$ s Time Delay. . . . .	36
4.9 S/N Ratio Versus Time Delay at 361.94 nm. . . . .	36
4.10 Calibration Curve for Ni (UV) at 361.94 nm . . . . .	37
4.11 CCl <sub>4</sub> Spectrum Covering 705 - 805 nm . . . . .	39
4.12 CCl <sub>4</sub> Spectrum Covering 585 - 685 nm (100 $\mu$ m slit width) . . . . .	41
4.13 C <sub>2</sub> Cl <sub>4</sub> Spectrum Covering 465 - 565 nm. . . . .	41
4.14 C <sub>2</sub> HCl <sub>3</sub> Spectrum Covering 465 - 565 nm. . . . .	43
4.15 CHCl <sub>3</sub> Spectrum Covering 345 - 445 nm (0.8 ND filter) . . . . .	44
4.16 C <sub>2</sub> HCl <sub>3</sub> (1.20 g/l) Spectrum Covering 665 - 765 nm. . . . .	46

<b>Figure</b>	<b>Page</b>
4.17 Water Spectrum Covering 665 - 675 nm (100 $\mu\text{m}$ slit width) . . . . .	46
4.18 S/N Ratio Versus Time Delay for N (UV) at 746.83 nm . . . . .	47
5.1 Cl Intensity Versus Cl Concentration at 725.66 nm . . . . .	58
5.2 CN Intensity Versus C Concentration . . . . .	59
5.3 Simulated Calibration Curve for $\text{CCl}_4$ . . . . .	62
5.4 Simulated Calibration Curve for $\text{CHCl}_3$ . . . . .	63
5.5 Simulated Calibration Curve for $\text{C}_2\text{Cl}_4$ . . . . .	63
5.6 Simulated Calibration Curve for $\text{C}_2\text{HCl}_3$ . . . . .	64
D.1 $\text{CCl}_4$ Spectrum Covering 705 - 805 nm . . . . .	71
D.2 $\text{CHCl}_3$ Spectrum Covering 705 - 805 nm . . . . .	71
D.3 $\text{C}_2\text{Cl}_4$ Spectrum Covering 705 - 805 nm . . . . .	72
D.4 $\text{C}_2\text{HCl}_3$ Spectrum Covering 705 - 805 nm . . . . .	72
D.5 $\text{CCl}_4$ Spectrum Covering 665 - 765 nm (100 $\mu\text{m}$ slit width) . . . . .	73
D.6 $\text{CHCl}_3$ Spectrum Covering 665 - 765 nm (100 $\mu\text{m}$ slit width) . . . . .	73
D.7 $\text{C}_2\text{Cl}_4$ Spectrum Covering 665 - 765 nm . . . . .	74
D.8 $\text{C}_2\text{HCl}_3$ Spectrum Covering 665 - 765 nm . . . . .	74
D.9 $\text{CCl}_4$ Spectrum Covering 625 - 725 nm (100 $\mu\text{m}$ slit width) . . . . .	75
D.10 $\text{CHCl}_3$ Spectrum Covering 625 - 725 nm (100 $\mu\text{m}$ slit width) . . . . .	75
D.11 $\text{C}_2\text{Cl}_4$ Spectrum Covering 625 - 725 nm . . . . .	76

<b>Figure</b>	<b>Page</b>
D.12 C <sub>2</sub> HCl <sub>3</sub> Spectrum Covering 625 - 725 nm . . . . .	76
D.13 CCl <sub>4</sub> Spectrum Covering 585 - 685 nm (100 µm slit width) . . . . .	77
D.14 CHCl <sub>3</sub> Spectrum Covering 585 - 685 nm (100 µm slit width) . . . . .	77
D.15 C <sub>2</sub> Cl <sub>4</sub> Spectrum Covering 585 - 685 nm . . . . .	78
D.16 C <sub>2</sub> HCl <sub>3</sub> Spectrum Covering 585 - 685 nm . . . . .	78
D.17 CCl <sub>4</sub> Spectrum Covering 545 - 645 nm (100 µm slit width) . . . . .	79
D.18 CHCl <sub>3</sub> Spectrum Covering 545 - 645 nm (100 µm slit width) . . . . .	79
D.19 C <sub>2</sub> Cl <sub>4</sub> Spectrum Covering 545 - 645 nm . . . . .	80
D.20 C <sub>2</sub> HCl <sub>3</sub> Spectrum Covering 545 - 645 nm . . . . .	80
D.21 CCl <sub>4</sub> Spectrum Covering 505 - 605 nm (100 µm slit width) . . . . .	81
D.22 CHCl <sub>3</sub> Spectrum Covering 505 - 605 nm (100 µm slit width) . . . . .	81
D.23 C <sub>2</sub> Cl <sub>4</sub> Spectrum Covering 505 - 605 nm . . . . .	82
D.24 C <sub>2</sub> HCl <sub>3</sub> Spectrum Covering 505 - 605 nm . . . . .	82
D.25 CCl <sub>4</sub> Spectrum Covering 465 - 565 nm (100 µm slit width) . . . . .	83
D.26 CHCl <sub>3</sub> Spectrum Covering 465 - 565 nm (20 µm slit width) . . . . .	83
D.27 C <sub>2</sub> Cl <sub>4</sub> Spectrum Covering 465 - 565 nm . . . . .	84
D.28 C <sub>2</sub> HCl <sub>3</sub> Spectrum Covering 465 - 565 nm . . . . .	84
D.29 CCl <sub>4</sub> Spectrum Covering 425 - 525 nm (100 µm slit width) . . . . .	85
D.30 CHCl <sub>3</sub> Spectrum Covering 425 - 525 nm (20 µm slit width) . . . . .	85

<b>Figure</b>	<b>Page</b>
D.31 C <sub>2</sub> Cl <sub>4</sub> Spectrum Covering 425 - 525 nm . . . . .	86
D.32 C <sub>2</sub> HCl <sub>3</sub> Spectrum Covering 425 - 525 nm . . . . .	86
D.33 CCl <sub>4</sub> Spectrum Covering 385 - 485 nm (20 μm slit width) . . . . .	87
D.34 CHCl <sub>3</sub> Spectrum Covering 385 - 485 nm (20 μm slit width) . . . . .	87
D.35 C <sub>2</sub> Cl <sub>4</sub> Spectrum Covering 385 - 485 nm . . . . .	88
D.36 C <sub>2</sub> HCl <sub>3</sub> Spectrum Covering 385 - 485 nm . . . . .	88
D.37 CCl <sub>4</sub> Spectrum Covering 345 - 445 nm (0.8 ND filter) . . . . .	89
D.38 CHCl <sub>3</sub> Spectrum Covering 345 - 445 nm (0.8 ND filter) . . . . .	89
D.39 C <sub>2</sub> Cl <sub>4</sub> Spectrum Covering 345 - 445 nm (0.8 ND filter) . . . . .	90
D.40 C <sub>2</sub> HCl <sub>3</sub> Spectrum Covering 345 - 445 nm (0.8 ND filter) . . . . .	90

## List of Tables

<b>Table</b>	<b>Page</b>
4.1 Spectrum Line Assignments for Figure 4.1 . . . . .	28
4.2 Results from Gate Width Experiment for Ni (IR) . . . . .	33
4.3 Spectrum Line Assignments for Figure 4.7 . . . . .	35
4.4 Results from Gate Width Experiment for Ni (UV) . . . . .	37
4.5 Calibration Curve Data for Ni (UV) . . . . .	38
4.6 Spectrum Line Assignments for Figure 4.11 . . . . .	39
4.7 Cl Line Intensities at 725.66 nm for Solvents Tested . . . . .	40
4.8 Spectrum Line Assignments for Figure 4.13 . . . . .	42
4.9 Spectrum Line Assignments for Figure 4.15 . . . . .	44
4.10 Spectrum Line Assignments for Figures 4.16 and 4.17 . . . . .	47
4.11 Results from Gate Width Experiment for CCl <sub>4</sub> (0.971 g/l) . . . . .	48
5.1 Concentration of Chlorine in the Solvent Tested. . . . .	57
5.2 Concentration of Carbon in the Solvent Tested . . . . .	58
5.3 CN Line Intensities at 359.04 nm for Solvents Tested . . . . .	59
5.4 Cl/CN Ratios for Solvents Tested. . . . .	60
5.5 Calibration Curve Data for Chlorine . . . . .	64
A.1 Area/Noise for Ni (UV) at 361.94 nm . . . . .	67
C.1 Noise Levels at Various Concentrations . . . . .	69

## Abstract

Laser-induced breakdown spectroscopy (LIBS) is a spectroscopic technique where output from a pulsed laser is focused onto a target in order to create an intense plasma. The optical emission is characteristic of the elements in the focal volume and can be used for elemental analysis. Research on the detection of nickel in solution in addition to solvent detection of  $\text{CCl}_4$ ,  $\text{CHCl}_3$ ,  $\text{C}_2\text{Cl}_4$ , and  $\text{C}_2\text{HCl}_3$  has been performed. Breakdown was formed at the sample surface via a Q-switched Nd:YAG laser. Initially, operation of the laser was at 1064 nm/repetition rate of 5 Hz. Experiments were also performed using the third harmonic (355 nm)/repetition rate of 20 Hz. Pulse energy was maintained at 60 mJ. The spark light was spectrally resolved and detected by a time-gated photodiode array. A 50  $\mu\text{s}$  gate width/8  $\mu\text{s}$  time delay gave detection limits of 56.1 mg/l for nickel in solution. In the UV, a 10  $\mu\text{s}$  gate width/3  $\mu\text{s}$  time delay lowered detection limits down to 29.4 mg/l. Concentrations spanned from 50 to 1000 mg/l. Using UV excitation (10  $\mu\text{s}$  gate width/1  $\mu\text{s}$  time delay), saturated solvent solutions as high as 7.71 g/l were not detectable.

Laser-Induced Breakdown Spectroscopy  
on Solution Samples Using Surface Excitation

**I. Introduction**

**1.1 Overview**

Interest in monitoring environmental contamination in and around waste disposal sites and research facilities has grown recently. There seems to be an ever-increasing need to quickly and accurately measure toxic-trace elements in our environment.<sup>1</sup> Several methods to do just that are based on optical spectroscopic techniques. Such examples are inductively-coupled plasma optical emission spectroscopy (ICP-OES), graphite furnace atomic absorption spectroscopy (GF-AAS), and spark discharge optical emission spectroscopy (SD-OES). Unfortunately, these methods are performed in a laboratory far removed from the contaminated site. Samples have to be prepared and then sent out to a laboratory for analysis. One has to contend with a time delay between preparing the sample and waiting for the analytical result to arrive back from the laboratory.<sup>2</sup> With the increasing cost of sample preparation, the demand for a better method is high. New methods are needed to perform these concentration measurements *in situ* while still maintaining comparable analysis capability. Laser-Induced Breakdown Spectroscopy (LIBS) is one potential method. LIBS uses a laser to vaporize,

atomize, and excite small quantities of a sample. The resulting optical emission can then be used for elemental analysis.<sup>1</sup>

## **1.2 Problem Foundation**

LIBS is of interest to the United States Air Force for use in the environmental monitoring of heavy metals (suspected carcinogens) in contaminated groundwater. With this in mind, this study will begin by looking at nickel in solution. Additionally, it will be determined whether or not LIBS is suitable for solvent detection. Specifically, this research will look at carbon tetrachloride ( $\text{CCl}_4$ ), chloroform ( $\text{CHCl}_3$ ), tetrachloroethylene ( $\text{C}_2\text{Cl}_4$ ), and trichloroethylene ( $\text{C}_2\text{HCl}_3$ ). These solvents are currently being used in Air Force centers worldwide where aircraft are cleaned and repainted.<sup>3</sup> Unfortunately, their toxicity is high and they maybe carcinogenic.<sup>4</sup> Inadequate waste disposal of these carcinogens has led to contaminated groundwater in and around many areas of the country.<sup>5</sup> As the Department of Defense (DoD) tries to effectively manage safe handling of and waste disposal of these carcinogens, LIBS may potentially allow for easy monitoring of these activities. Even now, under a Tri-Service Reliance Agreement, a joint U.S. Army, Navy, and Air Force effort is underway to develop and test optical sensing techniques for the detection of soil and groundwater contaminants of interest to DoD.

### **1.3 Research Objectives**

This study has three primary objectives. The first objective is to construct an apparatus that is able to perform Laser-Induced Breakdown Spectroscopy on solution samples. The second objective of this thesis is to determine if LIBS is able to detect the aforementioned suspected carcinogens and if so; the final objective of this study is to generate calibration curves of analyte signal versus concentration and then determine detection limits for these samples.

### **1.4 Sequence of Presentation**

Chapter 2 begins with some of the background leading up to the idea of LIBS. It also provides some of the theory behind LIBS. Chapter 3 focuses on the experimental apparatus used in this study. It also discusses sample preparation techniques used in this research. Chapter 4 presents the results of this experiment while Chapter 5 provides a discussion of the data inherent to this study. The final chapter reviews the objectives of this thesis and offers some recommendations for general improvement to the experimental apparatus as well as some conclusions representative of the results.

## **II. Literature Review**

### **2.1 Background**

As previously mentioned, ICP-OES, GF-AAS, and SD-OES are currently being utilized for elemental analysis. In ICP-OES, the sample is prepared as an aerosol which is then injected with an argon gas flow into a heated plasma torch. Temperatures of the resultant plasma are between 6000 and 8000 K, effectively atomizing and exciting the aerosol. Multi-elemental analysis is then performed with a polychromator. Detection limits are usually between 0.5 and 50 µg/l.

On the other hand, GF-AAS is based on absorption features of the elements. The sample is dissolved and a droplet of the solution is fed into a graphite furnace. The furnace effectively atomizes the droplet and a cloud of atoms is formed. The absorption of radiation of an element-specific lamp is observed to determine element concentration. Unfortunately, this method is only suitable for trace analysis of single elements. Limits of detection for this technique are between 0.001 and 30 µg/l.

In SD-OES, a ground sample is atomized and excited by a spark discharge from an electrode. Light from the resultant plasma is observed by a polychromator for multi-elemental analysis. SD-OES, however, is limited to only substances with

sufficient electrical conductivity to act as a counter electrode. One can expect detection limits to be between 9 and 170 ppm.<sup>2</sup>

Notwithstanding these conventional methods, recent interest has turned towards the laser for vaporization and excitation of the target sample. The feasibility of using lasers as excitation sources in atomic emission spectroscopy dates back to 1962 when Brech and Cross first demonstrated this capability.<sup>6</sup> Since then, LIBS has been used in the analyses of gases, liquids, solids, liquid and solid aerosols, and soil samples.<sup>1</sup> One of the major advantages to using the laser is speed and simplicity. Because of the small size of the plasma (around 20 mm<sup>3</sup>) as well as its low energy content (< 500 mJ), only small amounts of sample are needed for elemental analysis. Depending on the elements present, the atoms excited by the laser may be neutral or ionized. Species are identified by spectrally resolving the spark light.<sup>7</sup> Other advantages over conventional methods are:

- 1) No auxiliary analysis equipment is needed as the laser vaporizes and excites the sample in one step.
- 2) The absence of auxiliary analysis equipment makes this method very economical.
- 3) Since LIBS is an emission technique, direct analysis provides multielement analysis without increased complexity.
- 4) LIBS is useful in applications requiring noninvasive analysis because the laser spark can be generated in remote locations.<sup>8</sup>

Unfortunately, there are a couple of factors that can make the use of LIBS difficult as an analytical technique. One drawback is the possibility of inducing chemical reaction in the sample under analysis. Laser radiation destroys the molecular bonds of the pollutants and information on the original concentration should be determined stoichiometrically by studying their ionic and atomic lines. The atoms of the molecules tend to recombine at the end of the breakdown process, producing several different compounds whose concentrations may not be easily related to the initial concentration of the pollutant.<sup>9</sup> Secondly, spectral line intensities last for several microseconds after the laser pulse and then decay away in a complex manner. The optimal timing for spectral acquisition involves a tradeoff between large intensities immediately after the laser pulse and interferences due to Stark broadening and plasma blackbody radiation.<sup>10</sup>

## **2.2 Theory Behind the Experiment**

When a sufficient amount of energy from an energetic laser pulse is focused in a gas, a spark plasma is formed at the focus. This plasma appears as a bright flash of white light accompanied by a loud sound. The spectrally dispersed light emanating from the spark plasma usually exhibits an atomic line emission superimposed on a broadband continuum. Typical thresholds for gas breakdown are around  $10^6$  W/cm<sup>2</sup>.

There are two steps leading to the breakdown of this gas. The first step involves the generation of a few free electrons by multiphoton ionization of atoms and molecules. The second step is an avalanche ionization of matter in the focal volume to form a plasma. In the classical sense, electric fields of the optical pulse accelerate the free electrons causing them to collide with neutral atoms. This produces an isotropic electron energy distribution. Eventually, the electron energy becomes sufficiently high enough to collisionally ionize an atom. This produces other electrons that follow the same course and cause further ionization. This process of electron multiplication continues throughout the pulse and results in significant breakdown of the gas. Following this breakdown, the plasma expands radially outward in all directions from the focal volume.<sup>8</sup>

The laser spark can also be generated by vaporizing solid surfaces. Focusing a high-powered laser onto a solid sample causes a complex series of events to occur. The intense local heating experienced by the sample causes the surface temperature of the target to rise rapidly at a rate of  $10^{10}$  K/s. As heat is conducted to the interior of the target, a thin molten layer forms just below the surface. As thermal energy deposited at the surface increases, eventually a point is reached where this energy exceeds the latent heat of vaporization. Once this occurs, heat cannot be conducted away fast enough to prevent the surface from reaching its boiling point and evaporation occurs at the surface.

Once vaporization occurs, this plasma is governed by gas dynamic processes. For irradiances just above threshold ( $10^{10} - 10^{11} \text{ W/m}^2$ ), evaporation at the surface proceeds at the normal boiling point of the material. Conversely, at irradiances well above threshold ( $10^{15} \text{ W/m}^2$ ), extremely dense plasmas are formed. Plasmas produced by irradiances between the two extremes are usually the most conducive to LIBS work.<sup>11</sup>

For irradiances within the specified range above, vaporization occurs rapidly and only a small fraction of the sample is molten. At the proper wavelength (the plasma frequency), the vaporized material forms a luminous plume which extends up from the surface at which time can absorb a large fraction of the remaining incident pulse energy. Hence, the plume effectively shields the surface of the target from further interaction with the laser pulse.<sup>8</sup> After removal of the laser pulse, the plasma continues to expand radially outward, becoming weaker and diffuse in appearance.

Hot plasmas are rich sources of excited atoms and ions. The relative intensities of spectral emission lines will ultimately lead to a determination of the composition of the target.<sup>11</sup> One of the most important requirements for quantitative analysis is the concept of local thermodynamic equilibrium (LTE). Simple stated, it is the assumption that all temperatures in the plasma, i.e. ion, electron, and neutral, are all the same. Moreover, the condition of LTE means that

rather than having to wait for the whole system to come to full equilibrium, it is sufficient to characterize a localized section of the plasma for a given point in time. Assuming that LTE has indeed been established, the electron temperature defines the excitation state of the plasma and elemental concentrations may be determined from the intensities of the spectral lines.<sup>12</sup>

For LTE to occur, collisions must dominate over the other energy transfer processes such as radiative decay and recombination. This will establish a Boltzmann-like distribution among the bound energy levels. In a partially ionized vapor, collisions will be the dominant mechanism of energy transfer because of the electron's high velocities and their long-range coulomb interaction. However, radiative processes also establish the populations of resonance levels of the major constituents of the plasma. Nevertheless, the small concentrations of trace elements present in the plasma ensure that electron collisions dominate over radiative processes and LTE is established between resonance levels.

Experimental observation of emissions from laser-induced plasmas show that initially, an intense continuum is emitted close to the surface of the target sample. This corresponds to the emission of blackbody (Bremsstrahlung) radiation from the dense plasma and typically lasts out to two or three microseconds. Shortly thereafter, as the plasma cools and expands away, line emissions tend to dominate the spectrum, with the first ionized species being emitted close to the

target. Atomic lines soon appear being located in higher regions of the plume.

Much later, emissions from simple molecules become apparent.<sup>11</sup>

Even though gases and solids have been fully theoretically explained, there is very little information in the literature that describes the fundamental physical processes of laser-induced breakdown in liquids. These processes are not very well understood. From experiment, it follows that the optical breakdown of liquids differs from that of gases in its external manifestations. Whereas the breakdown of gases results in a single laser spark in the lens focus (irrespective of focal length), in the case of liquids, long focal lengths lead to the production of several laser sparks along the laser axis. This is known as "multiplex" breakdown. In fact, this has been observed in gases when strongly absorbing microparticles with high concentration were introduced into the laser beam. Because of this, it was once thought that the optical breakdown of a liquid was initiated by strongly absorbing particles suspended in it.

Recently, a new theory about optical breakdown not associated with the idea absorbing particles has surfaced. The mechanism considered here is the same as that in gases, namely, electron avalanche development. Such a process is possible if there are gas bubbles in the focal region of the laser beam. In a superheated liquid, gas bubbles can be generated spontaneously. The development of an electron avalanche will ultimately lead to a rise in pressure inside these

bubbles. Consequently, the bubbles expand and merge into one large bubble. This is known as stimulated optic coalescence (SOC) and is the basis for this new theory. This so-called SOC effect is also accompanied by the heating of gas particles in the bubble as well as the eventual evaporation of its liquid wall. What happens is that the large bubble continues to expand at the expense of its stored energy. The final size of the bubble corresponds to the size of “cavitation bubbles” rising to the surface of the liquid from the region of liquid optical breakdown.<sup>13</sup>

### **2.3 Previous Work in the Field**

To the author’s knowledge, one of the first applications of LIBS was in 1983. Cremers and Radziemski looked at the detection of gases in air, particularly chlorine and fluorine. The excitation source used in this study was a Nd:YAG laser operating at 1.06 μm. Emission from the plasma was spectrally resolved by a Czerny-Turner spectrometer and monitored by a thermoelectric cooled photomultiplier tube. Time resolution of the plasma light was performed by a boxcar averager. Detection limits were established at 8 ppm for chlorine and 38 ppm for fluorine.<sup>14</sup>

Another study in 1991 continued to investigate the application of LIBS to gases in air. Casini et. al. looked at the emission spectra of a variety of pollutants in the early stages of plasma development (< 400 ns). Again, a Nd:YAG laser

operating at 1.06  $\mu\text{m}$  was the excitation source. Light emitted by the plasma was focused onto the slits of a monochromator and the resulting signal was collected by a photomultiplier tube. Detection limits were estimated at 60 ppm for Cl II, 200 ppm for S II, 200 ppm for P II, 110 ppm for Na II, 50 ppm for Hg I, 130 ppm for Be II, and 130 ppm for As II.<sup>15</sup>

In 1994, Lazzari et. al. used LIBS to measure small traces of heavy metals in the atmosphere, particularly mercury. The experimental setup used a Nd:glass laser, pulse width 8 ns, to deliver intense 400 mJ pulses. Repetition rate of the laser was at 10 Hz. Laser radiation was focused onto a sample contained in a glass vessel through the use of a spherical lens. Light from the plasma was sent through an optical fiber to a spectrometer at which time the signal from the spectrometer was recorded by an optical multichannel analyzer (OMA). To attain well-resolved spectra, a typical averaging of 400 samples was used. To obtain precise determination of the concentration of the mercury involved, Lazzari et. al. started out with a small amount of liquid mercury inside an experimental cell. After a few minutes, an equilibrium concentration of gaseous mercury was realized. The liquid mercury was then removed and the sample was ready for analysis. The experiment was run and detection limits were obtained. Lazarri et. al. found that they were able to detect concentrations of mercury as low as 5 ppb. This is quite

good considering the fact that health danger thresholds for this pollutant is

12 ppb.<sup>9</sup>

Finally in 1996, Robert J. Nordstrom conducted a study to evaluate the LIBS spectral characteristics of the interference from N<sub>2</sub> and O<sub>2</sub> gas in air. A CO<sub>2</sub> laser was used as the excitation source. The spectral range investigated was from 350 to 950 nm. Spectra was collected by a grating spectrometer and recorded by a photodiode array. Analysis of the spectra indicated that over a large range of CO<sub>2</sub> laser fluence, all spectra could be correlated by a multiplication factor. This meant that changes in the relative spectral contributions from N<sub>2</sub> and O<sub>2</sub> were not occurring. Additionally, it indicated that the contribution of different atomic ionization levels in the spectra did not change appreciably. This result is important for future LIBS work where air interferences must be considered.<sup>16</sup>

In addition to trace elements in air, LIBS can be used in the analysis of solids. In 1985, Belliveau et. al. used LIBS to detect Cr and Mn in steel. This study employed a 10 Hz, 1.06 μm, pulsed Nd:YAG laser in addition to two echelle spectrometers to monitor analyte emissions. Data was taken and calibration curves were developed. Additionally, a correlation study between dc plasma emission spectroscopy and LIBS performed on Ni showed that the two methods gave very similar results.<sup>17</sup>

In 1987, Cremers expanded the range of elements to which LIBS had been applied to. He investigated Mo, Ni, Al, Ti, Cu, Fe, Pb, and In. The source of excitation for this experiment was a Q-switched Nd:YAG laser. This time, however, light was collected by means of a fiber optic cable and transmitted to a spectrograph for spectral resolution. Spectra was recorded by a diode array rapid scanning spectrometer (DARSS). This work demonstrated that metals could be detected via LIBS at up to distances of 2.4 m between the sample and the focusing lens-light collection optics.<sup>18</sup>

Work by Grant et. al. proved to be similar in nature to Cremers. In 1991, they used LIBS to perform elemental analysis on iron ore. Unlike previous experiments, an excimer laser was the excitation source. Again, a fiber optic cable was used to collect and transmit the light emitted by the plasma to a monochromator. A photomultiplier tube recorded the spectra. Calibration curves were generated by plotting the ratio of the intensity of each element (Ca, Si, Mg, Al, and Ti) to that of iron ore. Detection limits were on the order of 0.01%.<sup>6</sup>

In 1994, Alexander et. al. set out to measure detection limits for chromium. The experiment used a Q-switched Nd:YAG laser operating at 1064 nm with a pulse width of 10 ns as an excitation source. Light from the laser was focused onto the sample by a plano-convex BK7 lens. Next, light emitted by the plasma was focused into an optical fiber for transmission to an OMA consisting of a

spectrometer and a photodiode array. They were able to generate a calibration curve for chromium with a detection limit down to 100 ppb.<sup>1</sup>

That same year, Thiem et. al. used LIBS in a ultra-high vacuum to perform elemental analysis on NIST transition metal alloys. The second harmonic ( $\lambda = 532$  nm) of a Nd:YAG laser was used as the excitation source to ablate the surface of a standard metal sample. The sample was kept on an X-Y translation table that was constantly moving throughout the course of irradiation. Light emitted by the plasma was collected by means of a fiber optic bundle which then guided the light to the spectrograph and photodiode array. Data was taken and detection limits were established: 0.08% for Al, 1.45 % for Cr, 0.70% for Co, 0.01% for Cu, 0.54% for Fe, 0.07% for Mn, 0.001% for Ni, 0.04% for Si, 0.11% for Ti, and 0.44% for Zn.<sup>19</sup>

Two years later, Pakhomov et. al. used LIBS to detect lead in concrete. The breakdown was formed at the sample surface by a pulsed Nd:YAG laser operating at 1.06  $\mu\text{m}$ . Light from the plasma was imaged onto a quartz optical fiber. The opposite end of the fiber was attached to the entrance slit of a Czerny-Turner spectrograph. Light was detected by a gated photodiode array. Contamination levels were inferred from the ratio of the emission line of lead to a known reference line. Lead contamination was determined down to 10 ppm.<sup>20</sup>

Recent interest has turned towards the analysis of liquids via LIBS.

Cremers et. al. first looked at LIBS as a way to analyze liquids in 1984. They looked at the dielectric breakdown of several elements in water. They noted that this breakdown occurs with focused laser powers of  $10^{10}$  -  $10^{11}$  W/cm<sup>2</sup> as compared to that of  $10^7$  -  $10^8$  W/cm<sup>2</sup> in air.<sup>21</sup> However, this threshold value is affected by such factors as impurities contained in the medium, irradiation geometry, and laser pulse width.<sup>22</sup> Output from a Nd:YAG laser was focused into various samples by a pair of 5 cm focal length lenses. The pulses were focused into the cell from the side because pulses entering from the top intercepted bubbles from previous sparks thereby interfering with spark formation. Light emitted by the plasma was spectrally resolved and then detected by a photomultiplier tube (PMT). Detection limits were established for Li, Na, K, Rb, Cs, Be<sup>+</sup>, Mg<sup>+</sup>, Ca<sup>+</sup>, and B. For example, limits of detection for the alkali metals ranged from 0.006 to 1.2 µg/ml. On the other hand, detection limits for the nonalkali elements proved to be much higher, anywhere from 1 to 1200 µg/ml.<sup>21</sup>

In 1987, Wachter et. al. looked at uranium in solution. They note that previous work analyzed liquids by the formation of the laser spark in a bulk liquid. This avoided the problem of spark perturbation due to surface agitation and splashing of the liquid, but resulted in a lower temperature and hence reduced excitation capability as that compared to a gas. Previous work has shown that with

bulk excitation, uranium concentrations as high as 300 g/l could not be detected. However, with surface excitation, uranium was detected at concentrations at several orders of magnitude below 300 g/l. Detection limits are improved with surface excitation because the solution is vaporized into hot plasma formed above the liquid surface where the sample is more efficiently excited.<sup>23</sup> Other advantages associated with surface excitation are that light emitted by the plasma will not be absorbed by other substances in the solution and that particles suspended in the air will not perturb spark formation nor scatter plasma light to any great extent.<sup>24</sup> Wachter et. al. focused pulses from a Q-switched Nd:YAG laser onto the surface of a solution thereby generating the laser spark. The plasma light, viewed through the side of the glass vial containing the solution, was then focused onto the slit of a spectrograph. The spectrally resolved light was then recorded by a DARSS detector. Using surface excitation, Wachter et. al. were able to lower detection limits for uranium down to 0.1 g/l.<sup>23</sup>

In 1991, Vlasov et. al. studied the question of how the principal elements of salt water solutions change in time as a result of breakdown at the water surface. Their principal focus was on estimating the detection limits and accuracy to which trace elements present in sea water could be determined. A Nd:YAG laser was the excitation source. Spectra obtained were either time integrated or taken instantaneously. Comparison of the two show that with time, the continuum

background diminishes rapidly while the contrast of the line spectrum increases. For example, the N II lines emit only during the first few hundred nanoseconds. This means that for all practical purposes, the atmosphere does not penetrate into the plume and only the surface layer of air contributes to the emission from the plume. They also note that the H<sub>α</sub> line reaches maximum intensity within 2 µs and virtually disappears after 6 µs. However, Na remains strong even out to 8 µs. A calibration curve for Na reveals a linear dependence for concentrations between 0.004 - 0.2 % by mass.<sup>25</sup>

A few years later, Cespedes et. al. looked at the analysis of liquids via LIBS. A Nd:YAG laser ( $\lambda = 1064$  nm) operating at 10 Hz with a pulse duration of 9 ns was used as the excitation source. Light from the plasma was collected by a lens and imaged onto the entrance slit of a 0.64 m spectrometer. The dispersed light exited the spectrometer and was recorded by an intensified photodiode array. Aqueous solutions of Cd, Co, Cr, Cu, Fe, Mn, Ni, Pb, Tl, Zn, Ag, and Hg were prepared. Data was taken and detection limits were obtained: 70 ppm for Mn, 300 ppm for Pb, 6 ppm for Tl, 100 ppm for Cr, and 1500 ppm for Fe. All other solutions were not detectable even at very high concentrations (10,000 ppm).<sup>26</sup>

In 1996, Knopp et. al investigated LIBS as an analytical tool for the detection of metal ions in solution. An excimer ( $\lambda = 308$  nm) pumped dye-laser system was the excitation source. The dye-laser pulse was at 500 nm with an

output of  $22 \pm 2$  mJ/pulse. Plasma emitted light was monitored by a polychromator and detected by an intensified time gated photodiode array. Detection limits for the metal ions were 500 mg/l for Cd<sup>2+</sup>, 12.5 mg/l for Pb<sup>2+</sup>, 6.8 mg/l for Ba<sup>2+</sup>, 0.13 µg/l for Ca<sup>2+</sup>, 13 µg/l for Li<sup>+</sup>, and 7.5 µg/l for Na<sup>+</sup>. Hg<sup>2+</sup> and Er<sup>3+</sup> were not detectable in solution.<sup>27</sup>

To the author's knowledge, there has not been any research on solvent detection via LIBS. Solvents pose a great health hazard to humans and this area of work needs to be examined. This study will answer the question of whether or not LIBS is a viable method for solvent detection.

### **III. Experimental Design and Methodology**

#### **3.1 Instrumentation**

The experimental setup used in this study is shown in Figure 3.1. The output from a Nd:YAG laser (Spectra-Physics Quanta Ray DCR-3) operated in Q-switched mode was focused via a 10 cm plano-convex lens onto the surface of a liquid sample. A prism was used to direct the laser pulse downward into a cuvette where the solution sample was held. Initially, the laser was run at 1064 nm with a repetition rate of 5 Hz. But soon the choice was made to run the laser at the third harmonic ( $\lambda = 355$  nm). Repetition rate was now at 20 Hz (unless otherwise noted). The purpose of doing this was to look at wavelength dependencies on LIBS signal as well as detection limits. In both cases, the laser was set to deliver 60 mJ/pulse (unless otherwise stated). This meant that the laser fluence on target was approximately  $10^3$  -  $10^4$  J/cm<sup>2</sup>.<sup>3</sup> Not shown in Figure 3.1 is a pyroelectric detector (Scientech, Model 380101). This was used to monitor pulse energy. Pulse width of the laser was about 15 ns. An average of 75 laser pulses (50 at 1064 nm) was used to obtain sufficient signal-to-noise (S/N) ratios.

Fine tuning of the laser focus onto the surface of the solution sample was accomplished through the use of 2-dimensional translation stages. Both the lenses (plano-convex and convex) as well as the cuvette holder were mounted onto these

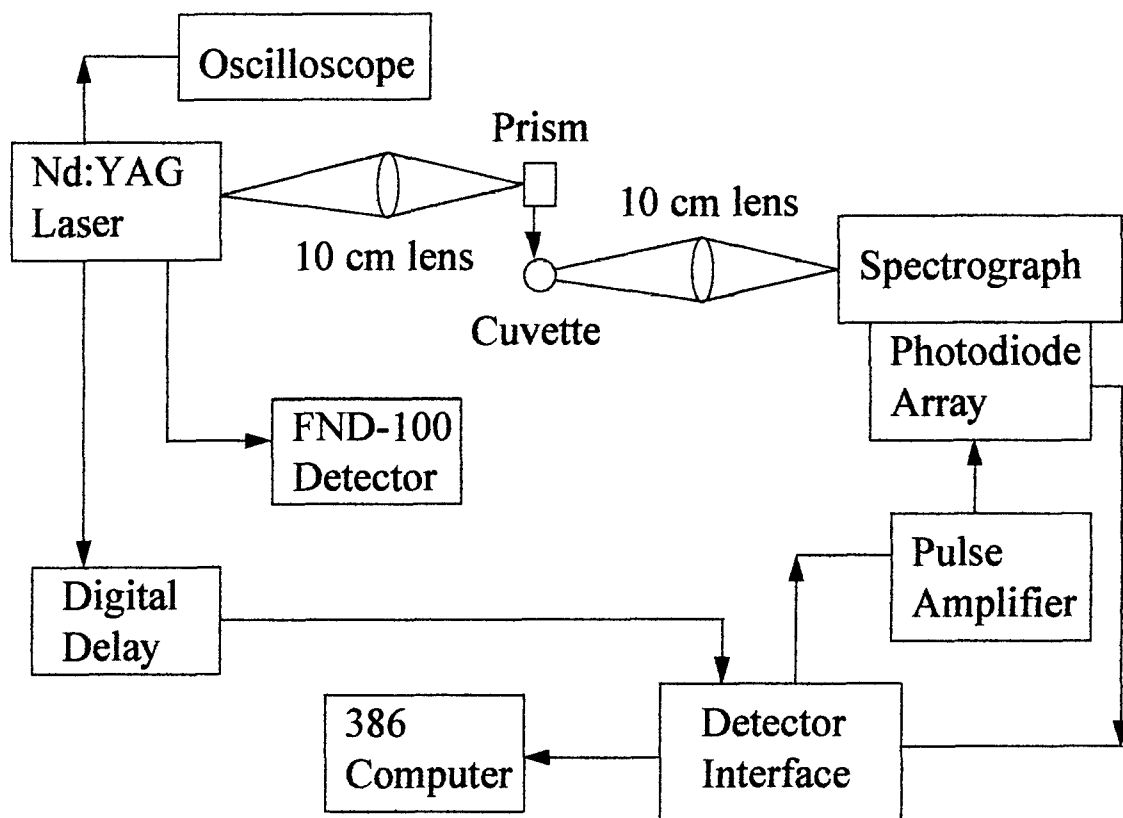


**Figure 3.1 Schematic of Experimental Apparatus**

translation stages. After completion of the adjustment, the slits of the spectrograph (Acton Research Corporation, Spectra-Pro 275) were aligned with respect to the location on the liquid surface where the laser was focused.

The spectrograph was oriented orthogonally to the laser axis in order to collect light emitted from the focal volume. A slit width of 100  $\mu\text{m}$  was used for nickel in solution while 50  $\mu\text{m}$  was used for solvent detection (unless otherwise noted). Wavelength region dictated what grating was to be used. The 1200

grooves/mm grating was blazed at 300 nm and was used for wavelengths less than 400 nm. The 600 grooves/mm grating was blazed at 500 nm and was used in the wavelength region of 400-760 nm. It was determined that the spectral resolution for the 1200 grooves/mm grating was 0.6 nm while it was 1 nm for the 600 grooves/mm grating. Once the spectrograph dispersed the light, the intensified photodiode array (EG&G PARC, Model 1420) would record this light as an analog signal. The detector interface (EG&G PARC, Model 1461) then would take this signal and convert it into a digital one where it would then be displayed on a computer monitor as intensity versus pixel number.

A wavelength calibration was used to convert the pixel number scale to one of a wavelength scale. This was done through the use of Ne, Hg, Ar, Kr, and Xe penlamps. It involved setting the spectrograph to a predetermined wavelength and capturing light from the penlamps. Spectra again was displayed as intensity versus pixel number. Wavelengths of these elements are well known and were used to match the peaks in the spectra with known wavelengths.<sup>28</sup> A linear fit of wavelength to pixel number produced a good calibration for the spectra. This was done every 20 nm (for both gratings). Calibration error was up to 0.2 nm for the 1200 grooves/mm grating while it was up to 0.5 nm for the 600 grooves/mm grating. Before all spectra were subject to analysis, the background generated by noise in the photodiode array and associated electronics would be recorded and then subtracted from the spectra.

So far, the FND-100 detector (EG&G PARC), the oscilloscope (LeCroy, Model 1420), the digital delay (Stanford Research Systems, Model DG535), and the pulse amplifier (EG&G PARC, Model 1304) have not been discussed. These were components of the equipment used in the timing of the system. The FND-100 detector was used to detect the laser pulse and initiate timing of the system. The oscilloscope was used to monitor this timing. It displayed voltage versus time. The digital delay generated a TTL (transistor-transistor logic) pulse that triggered the detector interface and associated electronics. Finally, the pulse amplifier sent a gating pulse to the photodiode array. Timing of the system is shown in Figure 3.2. This is a trace from the oscilloscope. As can be seen, the laser started at time  $t = 0$ . Ninety nanoseconds later, the digital generator generated a TTL pulse. One hundred and eighty nanoseconds after initiation of the laser trigger, the detector interface received that TTL pulse. Two hundred and twenty nanoseconds later, the pulse amplifier was triggered at which time the photodiode array was sent the gating pulse. The photodiode array then took its measurements at which time the system waited for the cycle to begin again. When the laser was operated at 5 Hz, a cycle was completed every 200 ms, while for 20 Hz, a cycle took 50 ms.

One also needed to choose a gate width and a time delay that would give rise to maximized S/N ratios. To do this, the experiment was run several times using a solution sample (1 g/l for Ni and 0.971 g/l for  $\text{CCl}_4$ ) at different gate

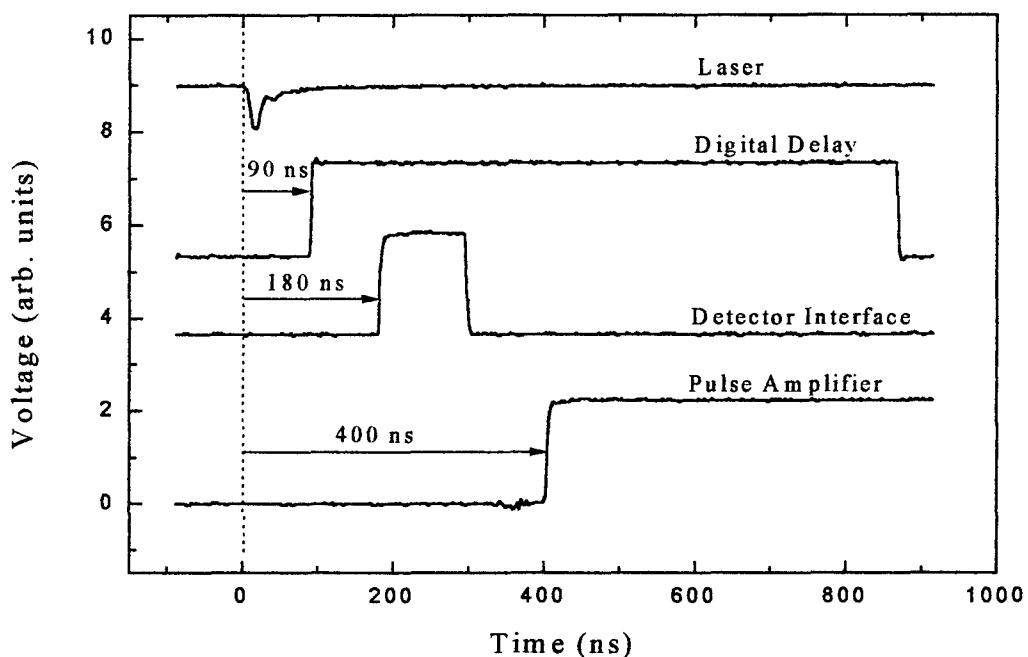


**Figure 3.2 Timing of the System**

widths and time delays. After looking over the results, a  $50\text{ }\mu\text{s}$  gate width and a  $8\text{ }\mu\text{s}$  time delay was chosen for use at the fundamental wavelength ( $1.06\text{ }\mu\text{m}$ ). However, for the third harmonic ( $\lambda = 355\text{ nm}$ ), a  $10\text{ }\mu\text{s}$  gate width and a  $3\text{ }\mu\text{s}$  time delay was used. For solvent detection ( $\text{CCl}_4$ ), a  $1\text{ }\mu\text{s}$  time delay was utilized.

### 3.2 Sample Preparation

In order to generate a calibration curve, one must run the experiment several times at differing concentrations. To accomplish this task, nickel in solution was diluted according to the following formula:

$$Molarity_{before} \times Volume_{before} = Molarity_{after} \times Volume_{after} \quad (3.1)$$

where molarity (M) is in units of moles/liter.

For example, if one had a solution with an initial concentration of 12 M, how much water must be added to decrease the molarity of the new solution down to 0.15 M and obtain 500 ml of the new batch? Using the formula above, one would need to measure out 6.25 ml of the 12 M solution and add enough water to the solution until the total volume reached 500 ml.<sup>29</sup>

Solvents, on the other hand, were prepared from concentrates. First one needed to determine their saturation limit, i.e., how much of the concentrate would the water absorb. The following formulas were used.<sup>30</sup> Conditions were at 25°C and units were in moles/liter (M):

$$\text{For CHCl}_3, \quad \log C_w = -1.19 \quad (3.2)$$

$$C_w = 0.0646 \text{ M} = 7.71 \text{ g/l}$$

$$\text{For CCl}_4, \quad \log C_w = -2.20 \quad (3.3)$$

$$C_w = 0.00631 \text{ M} = 0.971 \text{ g/l}$$

$$\text{For } \text{C}_2\text{HCl}_3, \quad \log C_w = -2.04 \quad (3.4)$$

$$C_w = 0.00912 \text{ M} = 1.20 \text{ g/l}$$

$$\text{For } \text{C}_2\text{Cl}_4, \quad \log C_w = -3.04 \quad (3.5)$$

$$C_w = 0.151 \text{ g/l}$$

One would prepare the base (saturated) solutions by first measuring out the proper amount of concentrate needed. A pan balance was used to perform this task.

Next, a liter of water was weighed out (density ~ 1000 g/l) and then added to the solvent. Once the base solutions were available, the dilutions were prepared in the same manner.<sup>31</sup>

## IV. Results

### 4.1 Nickel in Solution (IR Excitation at 1064 nm)

A typical spectrum covering the wavelength region from 335 to 385 nm for nickel in solution is shown below in Figure 4.1. Spectral line assignments are shown in Table 4.1.<sup>32</sup> (Transitions shown are from lower state to upper state.) All nickel lines were atomic in nature. Ions were not detected in this spectrum. As one can see, there are many discernible peaks to choose from for elemental analysis. In this case, the 352.45 nm line, labeled "D" in the figure, was chosen.

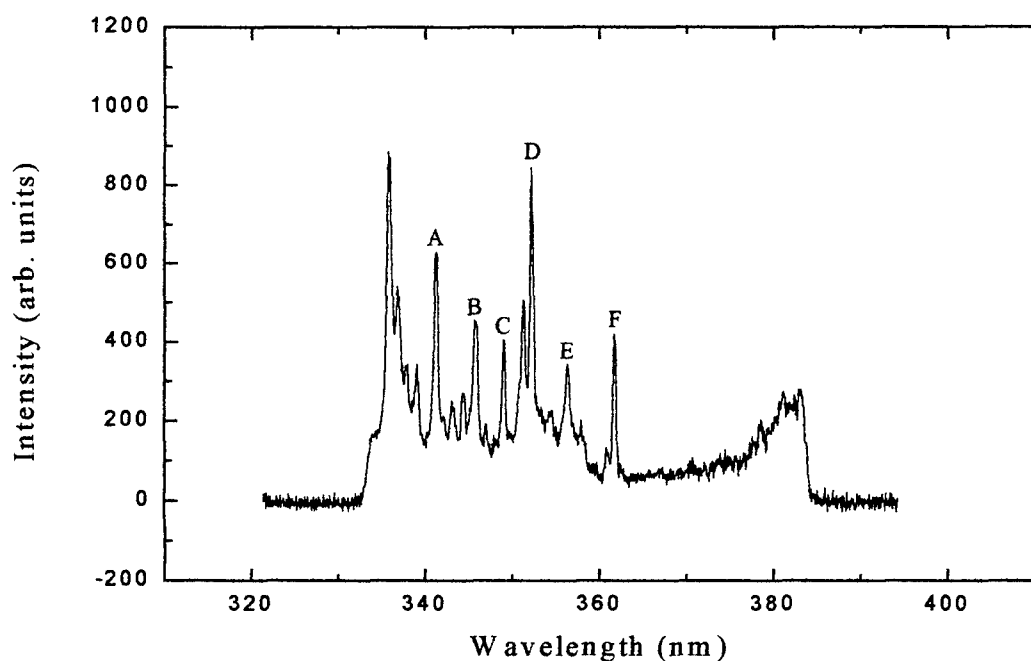


**Figure 4.1 Ni (1 g/l - IR) at 50  $\mu$ s Gate Width and 8  $\mu$ s Time Delay**

**Table 4.1 Spectrum Line Assignments for Figure 4.1**

Letter	Wavelength (nm)	Transition
A	341.48 nm	$4s\ ^3D - 4p\ ^3F^o$
B	345.85 nm	$4s\ ^3D - 4p\ ^3F^o$
C	349.30 nm	$4s\ ^3D - 4p\ ^3P^o$
D	352.45 nm	$4s\ ^3D - 4p\ ^3P^o$
E	356.64 nm	$4s\ ^1D - 4p\ ^1D^o$
F	361.94 nm	$4s\ ^1D - 4p\ ^1F^o$

This was the logical choice as it had a very high intensity as that compared to the others. Also note that water plays an integral part in it's contribution to the spectrum. This can be seen from Figure 4.2. However, only one peak is clearly discernible in the water spectrum. It is due to NH ( $A\ ^3\Pi - X\ ^3\Sigma^-$  system).<sup>33,34</sup> Note that as one decreases the time delay, the continuum background due to Bremsstrahlung radiation becomes the dominant feature. This is shown in Figures 4.3 and 4.4. At the beginning of the experiment, the optimal conditions were not known. Using a pulse amplifier, spectra were gated and observation times were chosen. This was done to maximize S/N ratios. Since the optimum time is somewhat dependent on the species involved, it should be determined for each species investigated. The spectra were recorded and then a S/N ratio was determined for each plot. The signal can be determined in one of many different

ways. One could use the value of the intensity at the peak height. But this does not take into account how much of the intensity is due to the continuum background nor does it consider the variation of the background as a function of concentration. It is much better to use the difference between peak and base heights as a measure of the signal. Alternatively, one could use the area under the curve as a measure of the signal. The problem with this method is where does the spectral line start and the continuum background end. One must be very careful in choosing which spectral line to use for elemental analysis.<sup>3</sup> The noise was

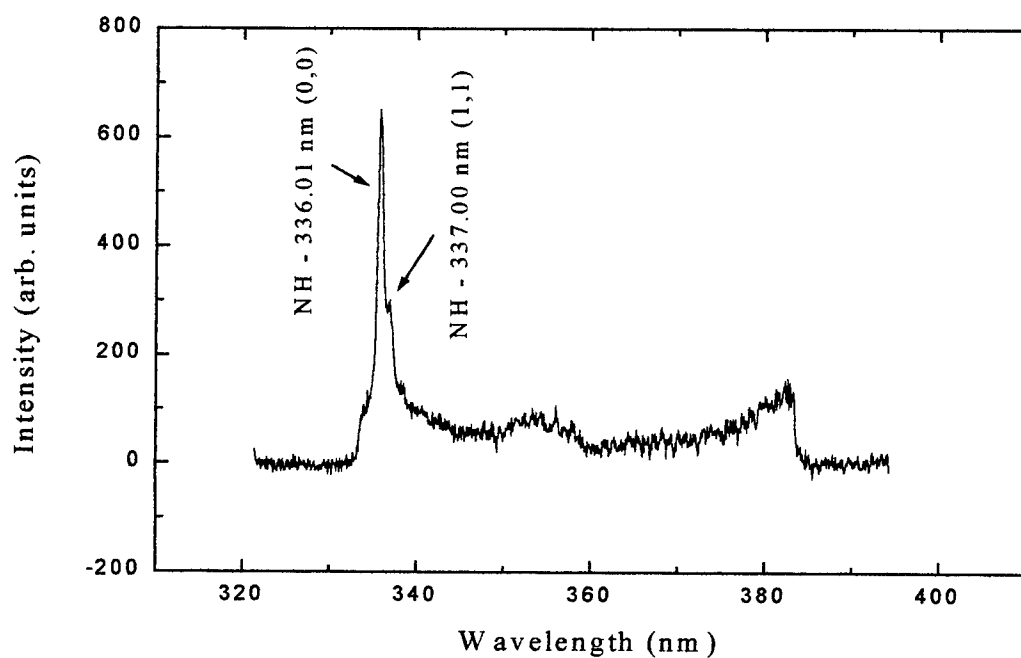


**Figure 4.2 Deionized Water (IR) at 50  $\mu$ s Gate Width and 8  $\mu$ s Time Delay**

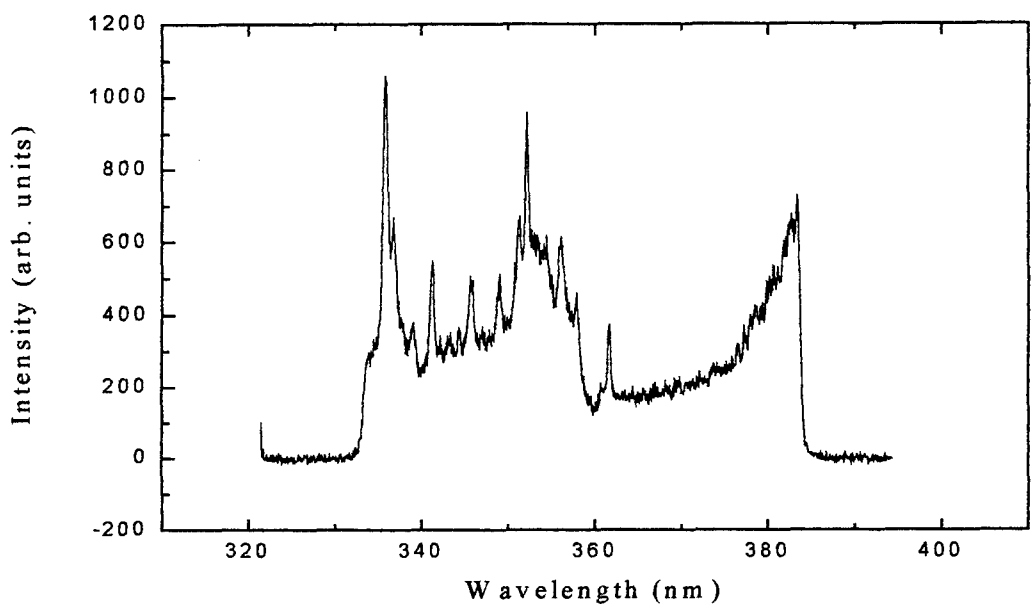


**Figure 4.3** Ni (1 g/l - IR) at 50  $\mu$ s Gate Width and 4  $\mu$ s Time Delay

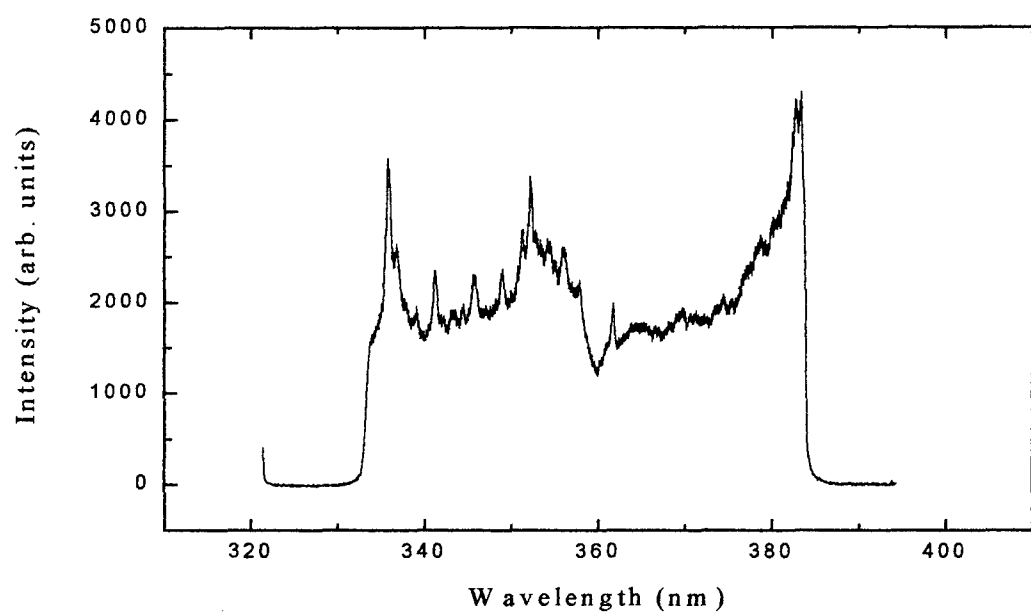


**Figure 4.4** Ni (1g/l - IR) at 50  $\mu$ s Gate Width and 1  $\mu$ s Time Delay

estimated by calculating the standard deviation of the continuum background (RMS noise) in a portion of the spectrum that was essentially featureless. The value of the intensities in that region were known so that the standard deviation was easily obtainable. In comparing S/N ratios with area/noise ratios, one obtained a much higher value for the S/N ratio. This is shown in Appendix A. Hence, it was easily justifiable to use the differencing technique as the measure of the signal in this research. It can be seen from Figure 4.5 that the trend shows that somewhere between 6 and 10  $\mu$ s gives maximized S/N ratios. A value of 8  $\mu$ s was chosen as the optimal delay time. Note that the curve follows a quadratic nature. The statistical error is also plotted as error bars in the figure. (Another source of error in the experiment is systematic error. This is briefly discussed in Appendix B.) Differing gate widths were also examined. There came a point when the S/N ratio dropped as one increased the gate width. This was probably due to increased noise as the gate width was increased. Table 4.2 summarizes the different time delays and gate widths that were looked at. The calibration curve for nickel in solution was taken by monitoring the atomic line at 352.45 nm 8  $\mu$ s after plasma initiation. It is shown in Figure 4.6. Diluted solutions spanned from 100 to 1000 mg/l. The curve had a correlation coefficient of 0.999. Detection limits were established by the following formula:

$$C_L = \frac{3N}{S} \quad (4.1)$$

where N, as before, is the standard deviation of the continuum background and S is the slope of the calibration curve.<sup>6</sup> Slope of the curve was 0.556 l/mg while the standard deviation of the background (from the 100 mg/l solution) was 10.4. (Noise levels at the other concentrations are shown in Appendix C.) Detection limits for nickel in solution using IR excitation were about 56.1 mg/l.

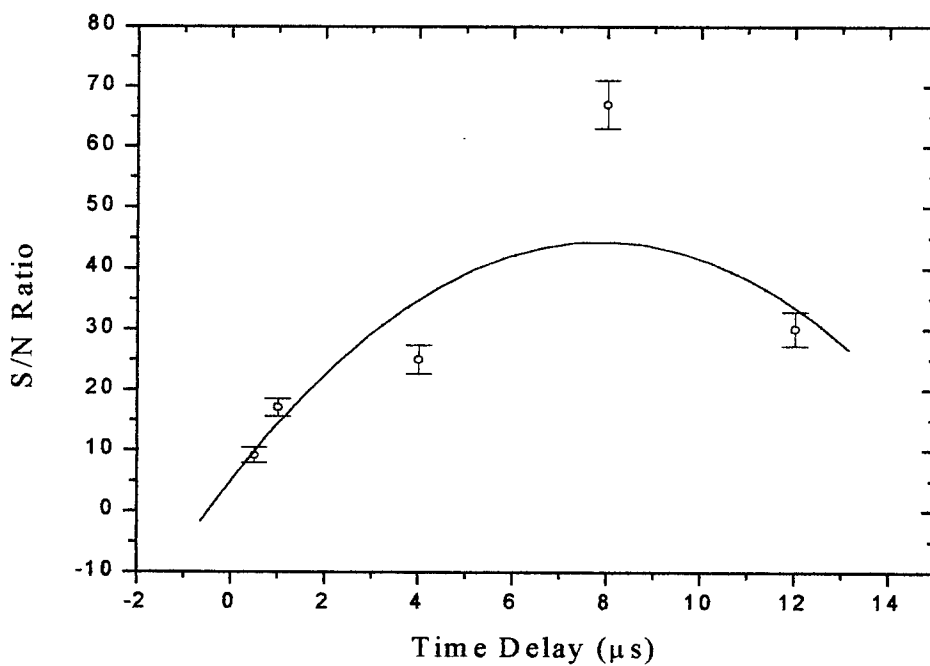


**Figure 4.5 S/N Ratio Versus Time Delay at 352.45 nm**

**Table 4.2 Results from Gate Width Experiment for Ni (IR)**

Gate Width ( $\mu\text{s}$ )	Time Delay ( $\mu\text{s}$ )	Signal	Noise	S/N Ratio
50	0	904	118	7.66
50	0.5	569	61.8	9.21
50	1	902	52.8	17.1
50	4	409	16.3	25.1
<b>50</b>	<b>8</b>	<b>561</b>	<b>8.38</b>	<b>66.9</b>
50	12	202	6.72	30.1
1	8	40.0	8.22	4.87
10	8	122	9.58	12.7
25	8	332	13.4	24.8
75	8	341	9.11	37.4

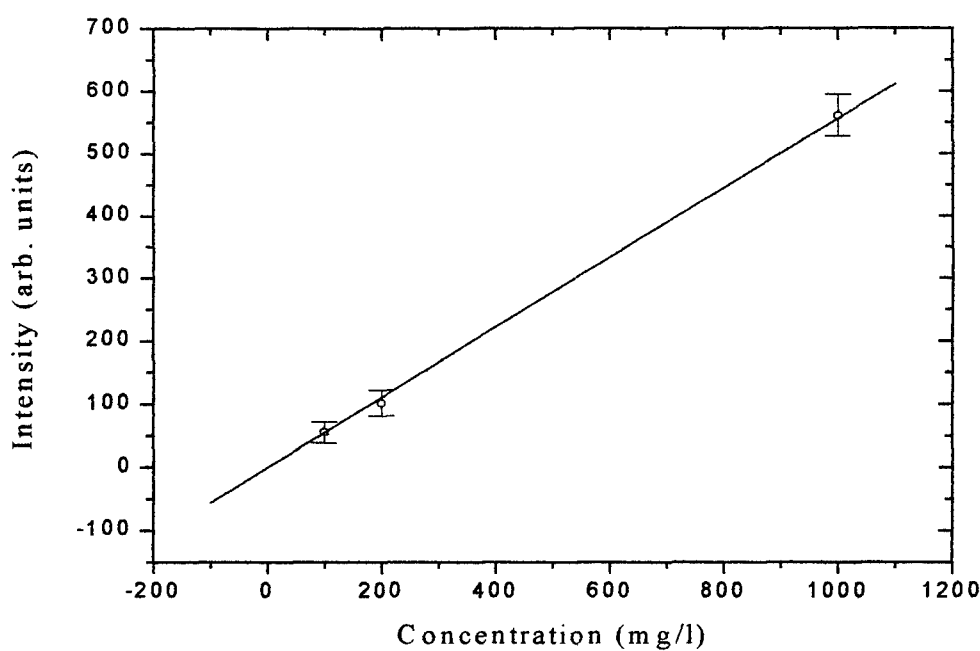


**Figure 4.6 Calibration Curve for Ni (IR) at 352.45 nm**

## 4.2 Nickel in Solution (UV Excitation at 355 nm)

A typical spectrum covering the wavelength region from 335 to 385 nm for nickel in solution is shown below in Figure 4.7. Spectral line assignments are shown in Table 4.3.<sup>32</sup> Again, analytical lines were atomic in nature. No ions were detected. Note that the intensity of these nickel lines are much greater than before - by a factor of 3 to 1. In addition to the 352.45 nm line, analytical lines at 341.48 and 361.94 nm were also chosen for elemental analysis. This was done because of possible interferences from the 355 nm laser line. Once more, the continuum background due to Bremsstrahlung radiation became the dominant feature as the

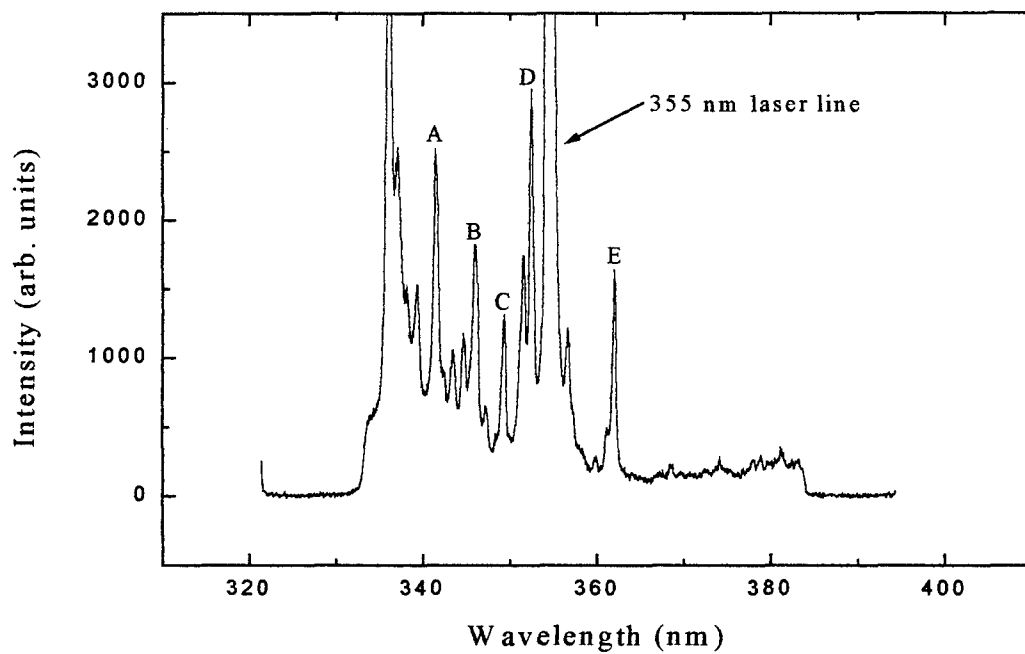


**Figure 4.7 Ni (1 g/l - UV) at 10  $\mu$ s Gate Width and 3  $\mu$ s Time Delay**

**Table 4.3 Spectrum Line Assignments for Figure 4.7**

Letter	Wavelength (nm)	Transition
A	341.48 nm	$4s\ ^3D - 4p\ ^3F^o$
B	345.85 nm	$4s\ ^3D - 4p\ ^3F^o$
C	349.30 nm	$4s\ ^3D - 4p\ ^3P^o$
D	352.45 nm	$4s\ ^3D - 4p\ ^3P^o$
E	361.94 nm	$4s\ ^1D - 4p\ ^1F^o$

time delay was decreased. This can be seen in Figure 4.8. Again, spectra were gated in order to determine an optimal delay time. This is shown in Figure 4.9. The trend clearly shows that somewhere around 3  $\mu$ s gave maximized S/N ratios. As before, the curve had a quadratic nature. Differing gate widths were also looked at. Table 4.4 summarizes these different conditions. (Data taken at 0.5  $\mu$ s time delay was at 10 Hz and 28 mJ.) Looking at Tables 4.2 and 4.4, one can see that there is no real wavelength dependence on the S/N ratios. Even though there was an increase in LIBS signal using UV excitation, noise had increased as well. The calibration curve for nickel in solution taken by monitoring the atomic line at 361.94 nm 3  $\mu$ s after plasma initiation is shown in Figure 4.10. Diluted solutions spanned from 50 to 1000 mg/l. The curve had a correlation coefficient of 0.994 while slope of the curve was 1.52 l/mg. The RMS noise (from the 50 mg/l solution) was 20.0. (Noise levels at the other concentrations are listed in

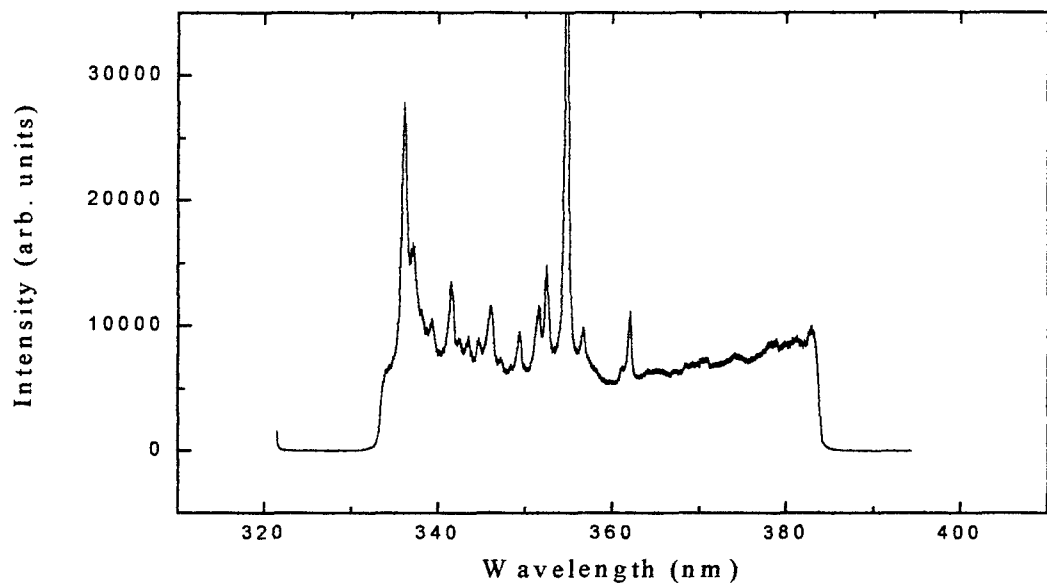


**Figure 4.8 Ni (1 g/l - UV) at 10  $\mu$ s Gate Width and 1  $\mu$ s Time Delay**

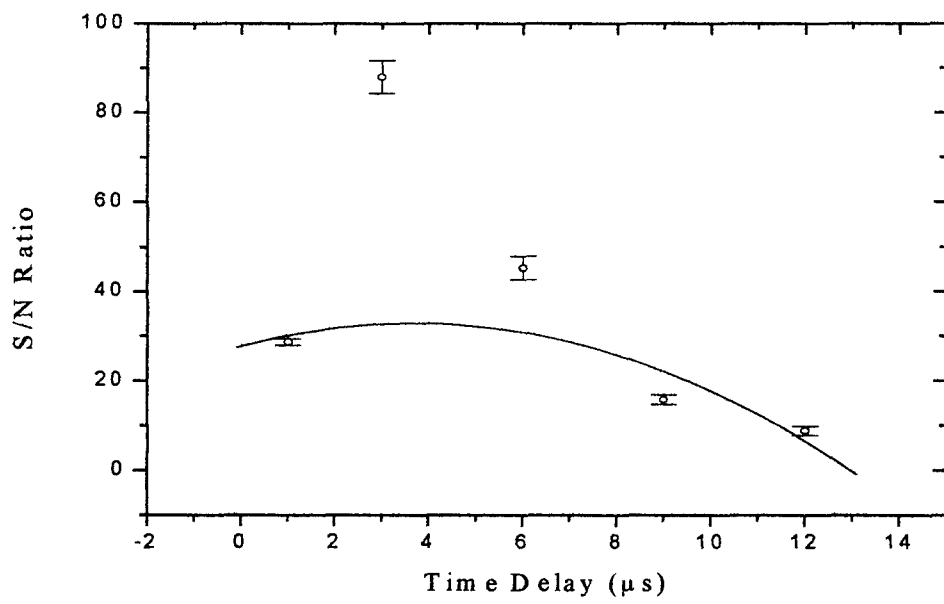


**Figure 4.9 S/N Ratio Versus Time Delay at 361.94 nm**

**Table 4.4 Results from Gate Width Experiment for Ni (UV)**

Gate Width ( $\mu\text{s}$ )	Time Delay ( $\mu\text{s}$ )	Signal	Noise	S/N Ratio
10	1	5318	186	28.6
<b>10</b>	<b>3</b>	<b>1416</b>	<b>16.1</b>	<b>88.0</b>
10	6	367	8.11	45.3
10	9	254	16.1	15.8
10	12	95	10.7	8.88
3	0.5	282	21.2	13.3
7	0.5	324	17.4	18.6
10	0.5	256	10.6	24.2
14	0.5	244	10.8	22.6
18	0.5	226	11.0	20.5

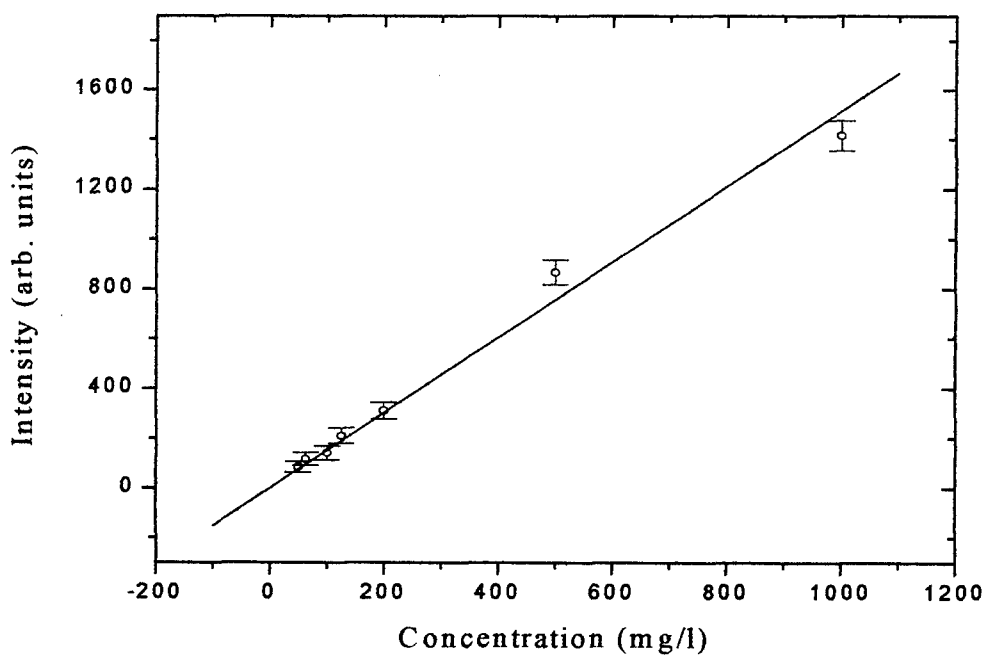


**Figure 4.10 Calibration Curve for Ni (UV) at 361.94 nm**

Appendix C.) The detection limit for this curve using UV excitation was about 39.5 mg/l. Data for all three calibration curves is shown in Table 4.5. The average detection limit was about 33.6 mg/l with a standard deviation of 5.26 mg/l.

**Table 4.5 Calibration Curve Data for Ni (UV)**

Wavelength	Correlation Coef.	Slope of Curve	Detection Limit
341.48 nm	0.988	1.88	31.9 mg/l
352.45 nm	0.984	2.04	29.4 mg/l
361.94 nm	0.994	1.52	39.5 mg/l
<b>Average</b>	---	---	$33.6 \pm 5.26$ mg/l

### 4.3 Pure Solvent Detection (UV Excitation)

Figure 4.11 is a spectrum for  $\text{CCl}_4$  covering the wavelength region of 705 to 805 nm. Two distinct chlorine lines can be seen at 725.66 and 754.71 nm.<sup>35,36</sup> They are atomic in nature and ions were not detected. Additionally, second order cyanogen lines (violet system,  $\text{B } 2\Sigma - \text{X } 2\Sigma$ ) as well as nitrogen lines were also discovered.<sup>34,37,38,39</sup> The nitrogen lines appear from the diffusion of air into the solution sample from the surface layer of air above it. Line assignments for this spectrum are listed in Table 4.6. A similar spectrum is also observed for  $\text{CHCl}_3$ ,  $\text{C}_2\text{Cl}_4$ , and  $\text{C}_2\text{HCl}_3$  (see Appendix D). One thing that was noticed, however, was

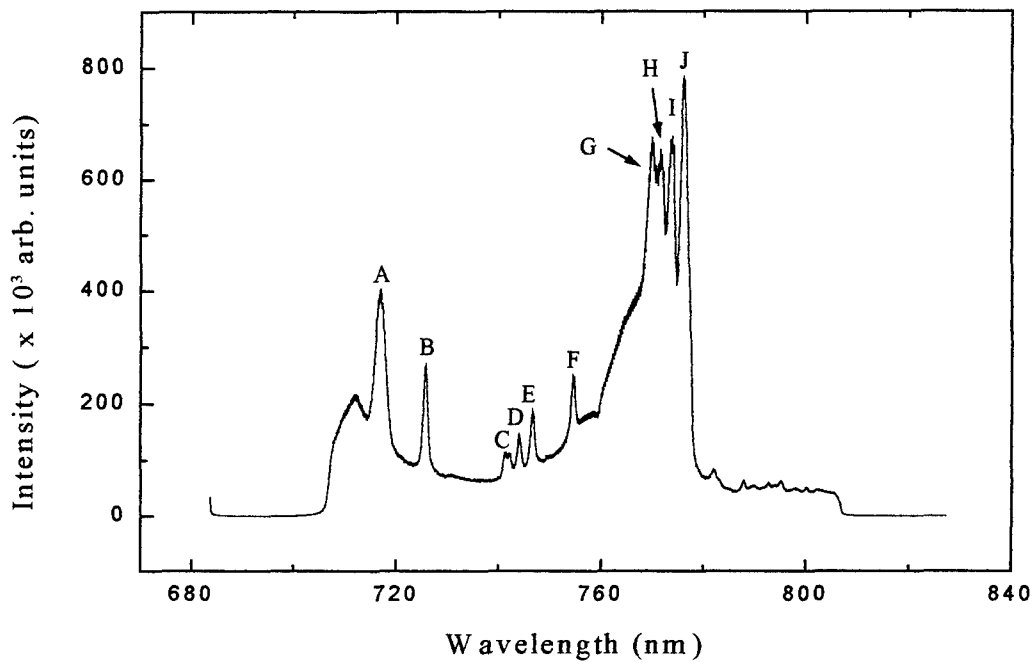


**Figure 4.11 CCl<sub>4</sub> Spectrum Covering 705 - 805 nm**

**Table 4.6 Spectrum Line Assignments for Figure 4.11**

Letter	Element	Wavelength	Transition	v'',v''
A	CN (2nd order)	359.04 nm	---	1,0
B	Cl I	725.66 nm	4s <sup>4</sup> P - 4p <sup>4</sup> S°	---
C	N I	742.36 nm	3s <sup>4</sup> P - 3p <sup>4</sup> S°	---
D	N I	744.23 nm	3s <sup>4</sup> P - 3p <sup>4</sup> S°	---
E	N I	746.83 nm	3s <sup>4</sup> P - 3p <sup>4</sup> S°	---
F	Cl I	754.71 nm	4s <sup>4</sup> P - 4p <sup>4</sup> S°	---
G	CN (2nd order)	385.47 nm	---	3,3
H	CN (2nd order)	386.19 nm	---	2,2
I	CN (2nd order)	387.14 nm	---	1,1
J	CN (2nd order)	388.34 nm	---	0,0

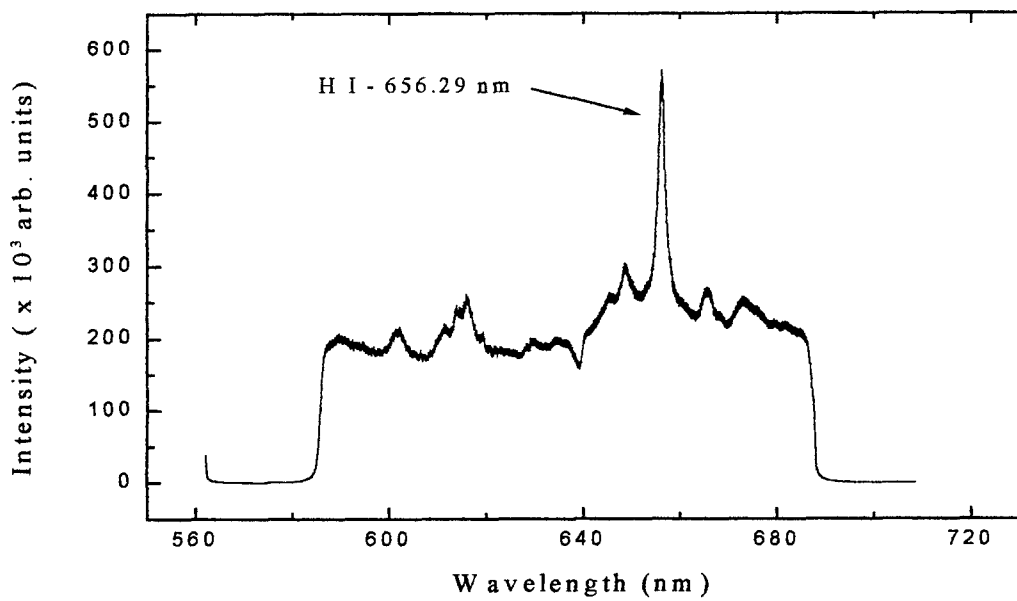
the fact that the intensities for the **chlorine** bands were not all the same. For example, it can be seen from Table 4.7 that single bond molecules have higher Cl line intensities than their double bond counterpart, i.e.,  $\text{CCl}_4 > \text{C}_2\text{Cl}_4$  and  $\text{CHCl}_3 > \text{C}_2\text{HCl}_3$ . Additionally, chlorocarbons have higher Cl line intensities than their hydrocarbon counterpart, i.e.,  $\text{CCl}_4 > \text{CHCl}_3$  or  $\text{C}_2\text{Cl}_4 > \text{C}_2\text{HCl}_3$ .

Figure 4.12 shows a  $\text{CCl}_4$  spectrum covering the wavelength region of 585 to 685 nm. Only one peak tends to stand out due to the large continuum background. Surprisingly, it is a hydrogen peak (at 656.29 nm).<sup>38,39</sup> But how could this be? Checking the bottle the  $\text{CCl}_4$  was stored in, it was noted that there were 10 ppm of water in the solution. Mystery solved! A similar peak is observed in the other solvents as well (see Appendix D).

Figure 4.13 is a  $\text{C}_2\text{Cl}_4$  spectrum covering the wavelength region of 465 to 565 nm. Note that there are three  $\text{C}_2$  Swan bands ( $d\ ^3\Pi_g - a\ ^3\Pi_u$  system) present in

**Table 4.7 Cl Line Intensities at 725.66 nm for Solvents Tested**

Solvent	Intensity (arb. units)
$\text{CCl}_4$	$1.79 \times 10^5 \pm 603$
$\text{CHCl}_3$	$8.69 \times 10^4 \pm 440$
$\text{C}_2\text{Cl}_4$	$3.32 \times 10^4 \pm 306$
$\text{C}_2\text{HCl}_3$	$2.49 \times 10^4 \pm 285$



**Figure 4.12  $\text{CCl}_4$  Spectrum Covering 585 - 685 nm (100  $\mu\text{m}$  slit width)**

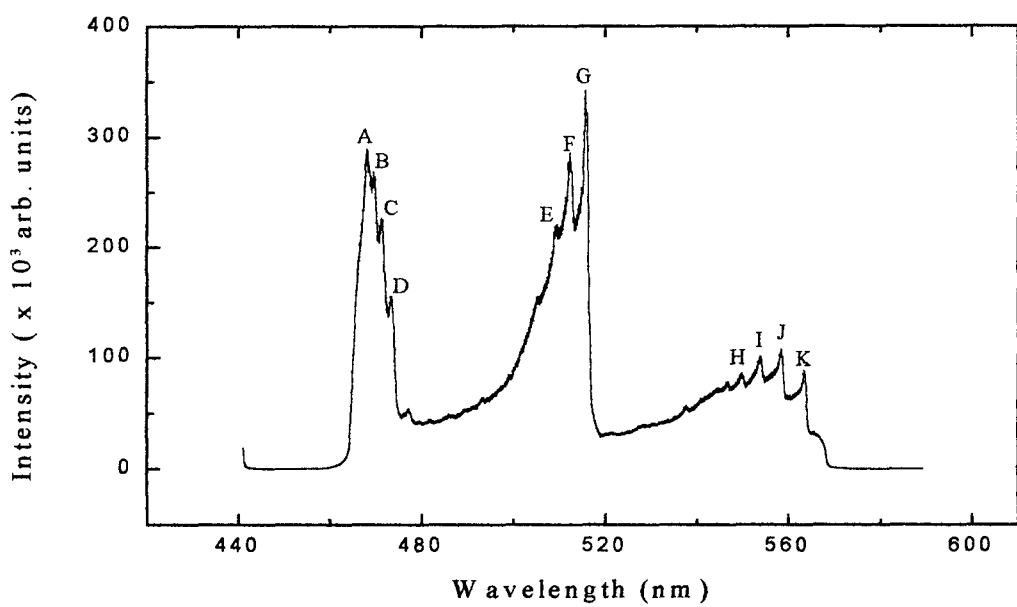


**Figure 4.13  $\text{C}_2\text{Cl}_4$  Spectrum Covering 465 - 565 nm**

the spectrum. (Spectra for  $\text{CCl}_4$  and  $\text{CHCl}_3$  had only the tiniest hint of the  $\text{C}_2$  Swan bands.) They arise from the photodissociation of the solvents and appear as photofragment emission spectra. Line assignments are given in Table 4.8.<sup>40</sup> Also notice that Figure 4.14 depicts a  $\text{C}_2\text{HCl}_3$  spectrum very similar to that found in Figure 4.13. But there is one difference, the 486.13 nm hydrogen peak.<sup>38,39</sup> At first glance, this does not appear to be seen in Figure 4.13. Nevertheless, one saw the 656.29 nm hydrogen peak in all the spectra. It would make sense that one should also see the 486.13 nm peak as well. In fact, it is there! But the continuum background is so large that it masks the peak. Remember that in the  $\text{C}_2\text{Cl}_4$

**Table 4.8 Spectrum Line Assignments for Figure 4.13**

Letter	Element	Wavelength	$v^{\prime}, v^{\prime \prime}$
A	$\text{C}_2$	468.48 nm	4,3
B	$\text{C}_2$	469.76 nm	3,2
C	$\text{C}_2$	471.52 nm	2,1
D	$\text{C}_2$	473.71 nm	1,0
E	$\text{C}_2$	509.77 nm	2,2
F	$\text{C}_2$	512.93 nm	1,1
G	$\text{C}_2$	516.52 nm	0,0
H	$\text{C}_2$	550.19 nm	3,4
I	$\text{C}_2$	554.07 nm	2,3
J	$\text{C}_2$	558.55 nm	1,2
K	$\text{C}_2$	563.55 nm	0,1

solution, hydrogen is only due to the 10 ppm of water in the solution. Since the number of emitters is quite low, the hydrogen peak most likely has an intensity much lower than that of the continuum background.

Figure 4.15 depicts a  $\text{CHCl}_3$  spectrum covering the wavelength region of 345 to 445 nm. Note that there are three distinct cyanogen peaks shown (violet system,  $\text{B}^2\Sigma - \text{X}^2\Sigma$ ). Line assignments are given in Table 4.9.<sup>34,37</sup> Also notice that the left two peaks were the second order peaks shown in Figure 4.11.  $\text{CCl}_4$ ,  $\text{C}_2\text{Cl}_4$ , and  $\text{C}_2\text{HCl}_3$  had similar spectra (see Appendix D).

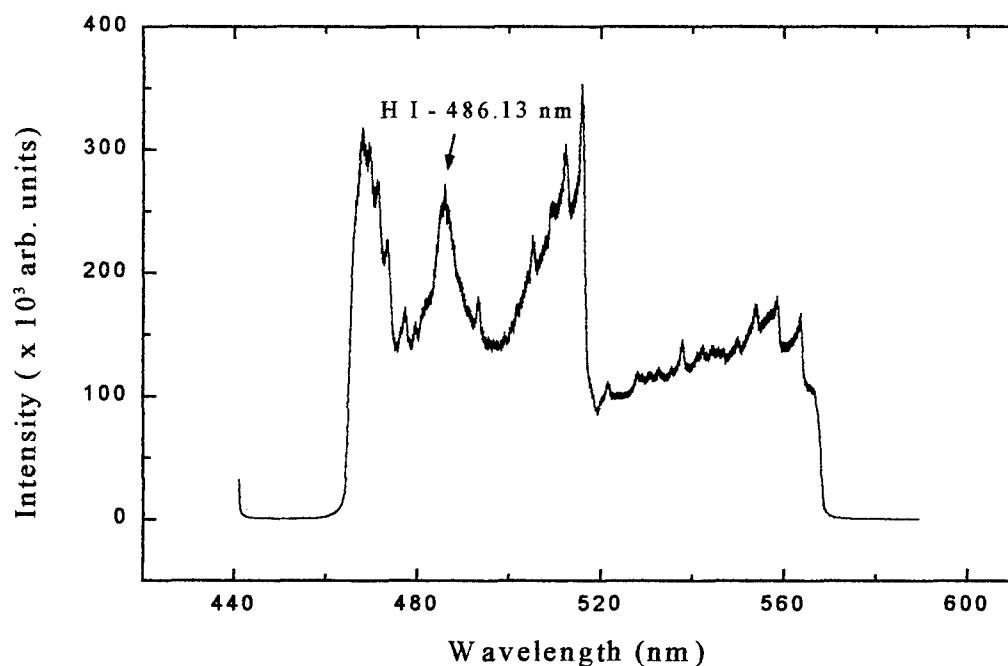


**Figure 4.14.  $\text{C}_2\text{HCl}_3$  Spectrum Covering 465 - 565 nm**

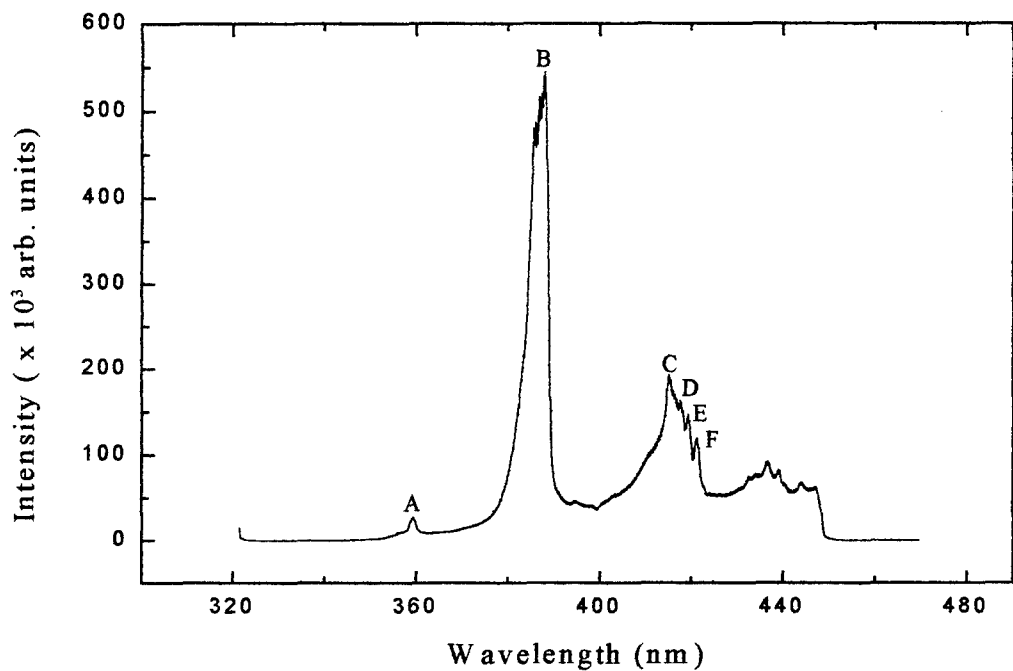


**Figure 4.15 CHCl<sub>3</sub> Spectrum Covering 345 - 445 nm (0.8 ND filter)**

**Table 4.9 Spectrum Line Assignments for Figure 4.15**

Letter	Element	Wavelength	v',v''
A	CN	359.04 nm	1,0
B	CN	388.34 nm	0,0
C	CN	416.78 nm	3,4
D	CN	418.10 nm	2,3
E	CN	419.72 nm	1,2
F	CN	421.60 nm	0,1

#### **4.4 Saturated Solvent Solutions (UV Excitation)**

Saturated solvent solutions were run at a 10  $\mu$ s gate width and a 1  $\mu$ s time delay. In every case, the chlorine bands were nonexistent. Even the CN bands were missing. This can be seen in the  $C_2HCl_3$  spectrum depicted in Figure 4.16. (Similar spectra were observed for  $CCl_4$ ,  $CHCl_3$ , and  $C_2HCl_3$  as well.) One will also note that this spectrum is very reminiscent of the deionized water spectrum shown in Figure 4.17. Line assignments are noted in Table 4.10.<sup>38,39</sup> The one surprising discovery was the fact that nitrogen appeared in every case. Now could it have been possible that the gating conditions were indeed not optimal? As a guide, the nitrogen peaks were used in a gating experiment (100  $\mu$ m slit width). Spectra were gated to determine an optimal delay time. Differing gate widths were also looked at. Sure enough, the trend showed that somewhere around a 10  $\mu$ s gate width and a 1  $\mu$ s time delay would give maximized S/N ratios. Results from the gate experiment are shown in Figure 4.18 and Table 4.11.

On a final note, it can be seen from Figures 4.16 and 4.17 that intensities in the water spectrum are about four times greater than that of the  $C_2HCl_3$  spectrum. However, the water spectrum was taken with a 100  $\mu$ m slit width (as opposed to 50  $\mu$ m). This will take care of a factor of two. So when slit widths are taken into account, intensities for the water spectrum double that of the  $C_2HCl_3$  spectrum. Quenching effects (due to the solvent) may be one possible explanation for this.

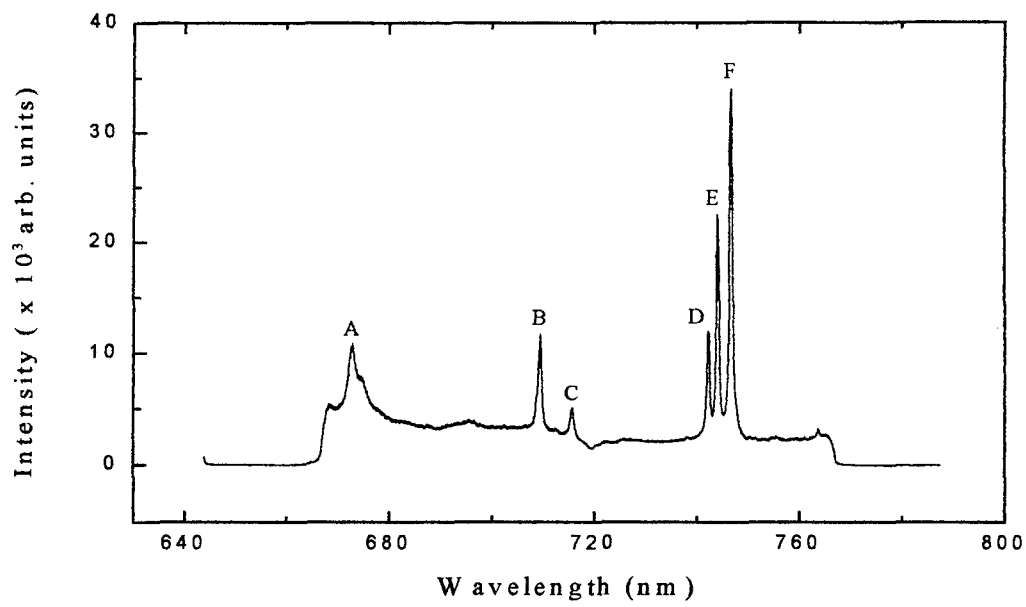


**Figure 4.16  $\text{C}_2\text{HCl}_3$  (1.20 g/l) Spectrum Covering 665 - 765 nm**

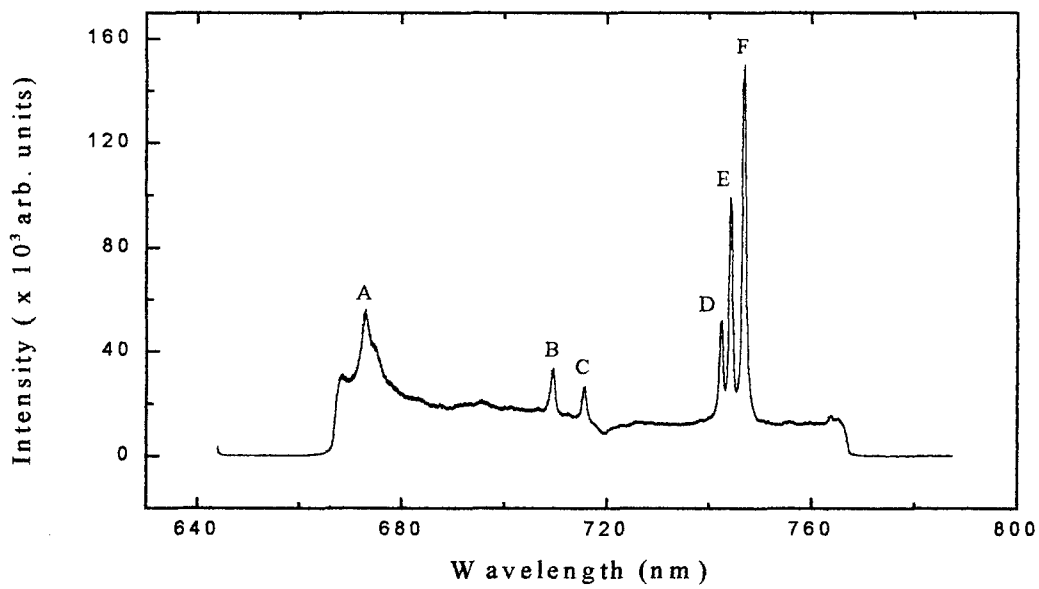


**Figure 4.17 Water Spectrum Covering 665 - 765 nm (100  $\mu\text{m}$  slit width)**

**Table 4.10 Spectrum Line Assignments for Figures 4.16 and 4.17**

Letter	Element	Wavelength	Transition
A	2nd order NH	336.01 nm	---
B	2nd order laser line	355.00 nm	---
C	O I	715.67 nm	$3s\ ^1D^o - 3p\ ^1D$
D	N I	742.36 nm	$3s\ ^4P - 3p\ ^4S^o$
E	N I	744.23 nm	$3s\ ^4P - 3p\ ^4S^o$
F	N I	746.83 nm	$3s\ ^4P - 3p\ ^4S^o$

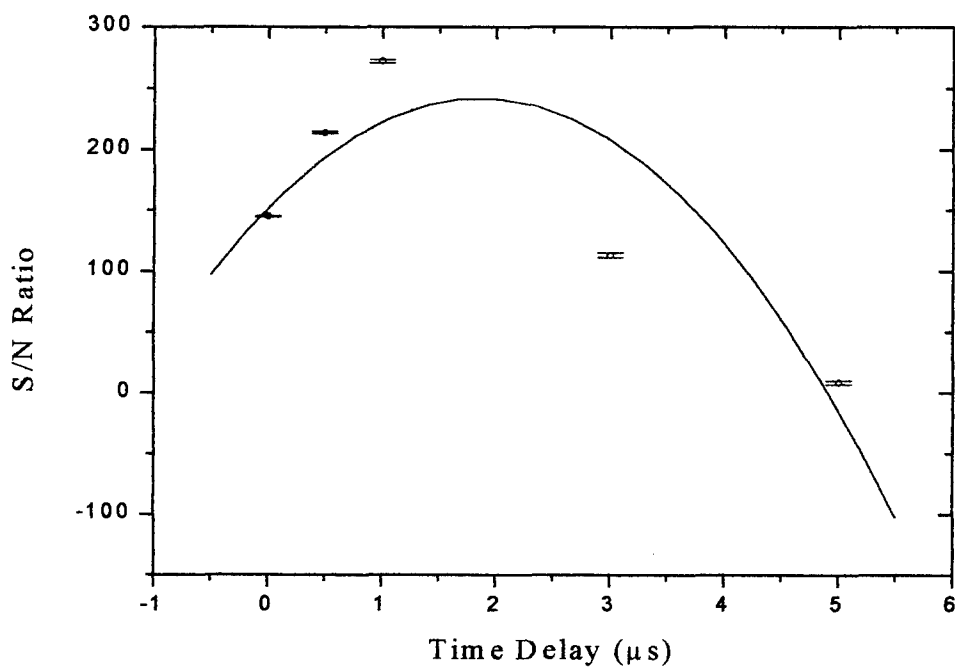


**Figure 4.18 S/N Ratio Versus Time Delay for N (UV) at 746.83 nm**

**Table 4.11 Results from Gate Width Experiment for CCl<sub>4</sub> (0.971 g/l)**

Gate Width (μs)	Time Delay (μs)	Signal	Noise	S/N Ratio
10	0	$1.55 \times 10^5$	$1.07 \times 10^3$	145
10	0.5	$7.06 \times 10^4$	330	214
10	1	$5.49 \times 10^4$	202	272
10	3	$4.74 \times 10^3$	41.8	113
10	5	88.0	10.2	8.63
3	1	$2.75 \times 10^4$	103	267
8	1	$2.23 \times 10^4$	107	208
12	1	$2.09 \times 10^4$	66.5	314
18	1	$2.66 \times 10^4$	105	253

## V. Discussion

### 5.1 General

As can be seen from Figure 4.4, the continuum background due to Bremsstrahlung radiation is emitted very early in the lifetime of the plasma. These results indicate (see Table 4.2) that by gating the signal, one can significantly improve the S/N ratio. Note that the analytical lines start to emerge from the continuum background and successively dominate the spectrum as the time delay is increased. Additionally, Figures 4.1 and 4.3 show, that at later times, these analytical lines are better resolved. This is due to the fact that the electron density decreases as the plasma cools.<sup>42</sup>

The data shown in Chapter 4 was a direct result of surface excitation (as opposed to bulk excitation) of the liquid sample and for good reason. As the focus of the laser waist was moved further into the bulk of the solution, the spark would start to fluctuate and eventually disappear. Consequently, the focus was kept at the surface of the liquid sample. There were also some other advantages to using surface excitation. First, any particles suspended in the solution would not hamper spark formation. Second, these particles would not scatter light to any great extent.<sup>23</sup>

One might recall that the choice was made to run the laser at 355 nm shortly after the experiment began. This was done to look at the wavelength dependencies on LIBS signal and detection limits. First, it is apparent from Figures 4.1 and 4.7 that the LIBS signal is much greater in the UV than in the IR. This made sense as absorption processes are more efficient in the UV.<sup>43</sup> But looking at Tables 4.2 and 4.4, it can be seen that the maximized S/N ratios from UV and IR excitation were virtually the same. Even the detection limits were very close. Initially, this seemed very puzzling as the LIBS signal in the UV was 3 times as large as that in the IR. But looking even closer, one sees that the noise level has also increased in the UV. This explains the almost identical S/N ratios. So while it seems that UV excitation will give a larger LIBS signal, there seems to be no wavelength dependence on detection limits.

One practical reason, however, for using UV excitation would be to decrease splashing effects. In the IR, the underside of the prism became coated with liquid soon after the start of the experiment thus causing the laser spark to quickly disintegrate. However, this effect was much less pronounced in the ultraviolet. The reason for this is that UV excitation is more efficient than IR excitation in the sense that more of the energy goes into vaporizing the liquid than heating it.<sup>3</sup>

## 5.2 Nickel in Solution

In looking through the literature, one will notice that there are very few publications available on the laser-induced breakdown of liquids. However, it might be instructive to compare the results of this study with what's out there. This research has shown detection limits for nickel in solution to be as low as 29.4 mg/l (in the UV). Cespedes et. al. also looked at heavy metals in solution (Cd, Co, Cr, Cu, Fe, Mn, Ni, Pb, Tl, Zn Au, and Hg). Their experimental setup was essentially the same as that used in this study, but for most of the metals tested, their results yielded far worse detection limits. In fact, a detection limit of 1500 mg/l was obtained for Fe. Some metals, such as Ni and Cr, were not even detectable. But why the discrepancy? The most likely answer for this is the fact that Cespedes et. al. used bulk excitation of the solution sample.<sup>26</sup> According to Wachter et. al., surface excitation gives far better detection limits. As discussed in Chapter 2, their study lowered detection limits for uranium in solution by 3 orders of magnitude (from 300 g/l to 0.1 g/l) from using surface excitation. Detection limits are improved by surface excitation because the solution is vaporized into hot plasma formed above the liquid surface where the sample is more efficiently excited.<sup>23</sup>

Cremers et. al looked at alkali metals in solution (Li, Na, K, Rb, and Cs) and found detection limits generally better than that of this research (0.006 - 1.2 mg/l).

As discussed in Chapter 2, their experimental setup differed only in the fact that they used a photomultiplier tube for detection purposes.<sup>21</sup> However, this was probably not the reason for their success. The fact of the matter is that alkali metals are easily ionized and thus should provide for low detection limits.<sup>44</sup> Additionally, it should be pointed out that 2N/S was used for their definition of detection limit. This alone would lower their results significantly.<sup>21</sup>

Knopp et. al looked at LIBS for the detection of metal ions ( $\text{Cd}^{2+}$ ,  $\text{Pb}^{2+}$ ,  $\text{Ba}^{2+}$ ,  $\text{Ca}^{2+}$ ,  $\text{Li}^{2+}$ ,  $\text{Na}^+$ ,  $\text{Hg}^{2+}$ , and  $\text{Er}^{3+}$ ). Since ions were not detected in this study, a direct comparison is not possible. But it is worth taking a look at. As mentioned in Chapter 2, their experimental setup was virtually the same as that used in this research, but with one minor exception. Their choice of excitation was an excimer ( $\lambda = 308 \text{ nm}$ ) pumped dye laser system. Detection limits for the metal ions were generally on the same order as for that found in this analysis (except for  $\text{Hg}^{2+}$  and  $\text{Er}^{3+}$  which were not detectable). However, as with Cremers et. al., their lighter elements ( $\text{Ca}^{2+}$ ,  $\text{Li}^+$ , and  $\text{Na}^+$ ) had much lower detection limits (in the  $\mu\text{g/l}$  range).<sup>27</sup>

Now how does nickel in solution compare to solid nickel? Thiem et. al. looked at solid nickel. Their experimental setup differed only in the fact that they used a fiber optic bundle to collect the light emitted by the plasma. They determined a detection limit of 10 ppm. This is slightly better than that found in this study (29.4 mg/l ~ 29.4 ppm). Additionally, Thiem et. al. performed their

experiment in an ultra-high vacuum. If anything, this helped to lower their detection limits as the vacuum would reduce the background signal found at atmospheric pressure.<sup>19</sup>

On a final note, the detection limits for nickel in solution were found to be in the mg/l range. Hence, this technique would be ideal in resolving such EPA compliance issues as groundwater contamination. It's relative simplicity and low cost offers significant advantages for in situ monitoring of groundwater runoff where sample preparation may not be an option. The equipment is fairly portable and analysis can be completed within 15 to 20 minutes.<sup>43</sup>

### **5.3 Pure Solvent Detection**

As noted in Chapter 4, the Cl line intensities at 725.66 nm for the single bond molecule was much greater than that of their double bond counterpart, i.e.,  $\text{CCl}_4 > \text{C}_2\text{Cl}_4$  or  $\text{CHCl}_3 > \text{C}_2\text{HCl}_3$ . Since the double carbon bond is stronger than the single carbon bond, it is only natural that it would take more energy (heat) to break the double bond. For example, as seen in Appendix E, the dissociation energy for  $\text{C}_2\text{Cl}_4$  is approximately 319 kcal/mole, while for  $\text{CCl}_4$ , it is 311 kcal/mole. Hence, it is not surprising that the Cl line intensity for the single bond molecule, e.g.,  $\text{CCl}_4$ , would have a larger peak intensity than that found for it's double bond counterpart.

Also mentioned in Chapter 4 was the fact that the Cl line intensities for the chlorocarbons were much higher than their hydrocarbon counterparts, i.e.,  $\text{CCl}_4 > \text{CHCl}_3$  or  $\text{C}_2\text{Cl}_4 > \text{C}_2\text{HCl}_3$ . One possibility is that hydrogen is scavenging some of the chlorine atoms to form hydrochloric acid. Unfortunately, emission lines for HCl were not detected. Emission for HCl usually takes place in the ultraviolet (198 - 237.5 nm) where it is often hard to detect. Pearse and Gayden quote that there is no available data on this transition but it is likely to be  $V\ ^1\Sigma - X\ ^1\Sigma$ .<sup>34</sup> Now if one assumes that the molar excitation efficiency for each solvent is the same, one would expect that the chlorine intensity of  $\text{CHCl}_3$  to be roughly 3/4 of  $\text{CCl}_4$ . If this assumption is true, one can see from Table 4.7 (at 725.66 nm) that  $\text{CHCl}_3$  should have an intensity of approximately  $1.34 \times 10^5 \pm 452$ . However, this estimate is too high. The experimental value was really  $8.69 \times 10^4 \pm 440$ . This leaves a difference of about  $4.71 \times 10^4$ . This discrepancy is most likely explained by the scavenging of Cl atoms spoken of earlier. Likewise,  $\text{C}_2\text{HCl}_3$  should have an intensity of around  $2.49 \times 10^4 \pm 230$ . Surprisingly, its experimental value was this number. Since the difference is zero, one notes that excitation efficiencies are probably not all the same and that scavenging of the Cl atom from  $\text{C}_2\text{HCl}_3$  is really minute at best.

There is one simple calculation that can be used to test this hypothesis. The rate law for the amount of HCl produced is:

$$\frac{d [HCl]}{dt} = k [Cl] [H] [M] \quad (5.1)$$

where  $[M]$  is the concentration of some arbitrary atom used to advance the 3-body reaction. This equation can be used to calculate the ratio of the amount of HCl produced from  $\text{CHCl}_3$  to that from  $\text{C}_2\text{HCl}_3$ . Using the Cl line intensities (proportional to the concentration involved) noted above, the ratio for the Cl atoms is  $8.69 \times 10^4 / 2.49 \times 10^4 = 3.49$ . Additionally, the ratio for the H atoms (at 486.13 nm) is  $4.72 \times 10^5 / 1.35 \times 10^5 = 3.50$ .

Hence,

$$\begin{aligned} \frac{d [\text{HCl}]_{\text{CHCl}_3} / dt}{d [\text{HCl}]_{\text{C}_2\text{HCl}_3} / dt} &\approx \frac{[\text{Cl}]_{\text{CHCl}_3} [\text{H}]_{\text{CHCl}_3}}{[\text{Cl}]_{\text{C}_2\text{HCl}_3} [\text{H}]_{\text{C}_2\text{HCl}_3}} \\ &\approx (3.49)(3.50) \\ &\approx 12.2 \end{aligned}$$

This means that  $\text{CHCl}_3$  is approximately 12 times more likely to get scavenged for Cl than  $\text{C}_2\text{HCl}_3$ .

There is one other way to determine if scavenging is going on. Let's start by calculating the approximate amount of chlorine in the solvent. The following formula may be used:

$$\text{concentration} \approx \frac{\text{density} \cdot \frac{\# \text{ chlorine}}{\text{per solvent}} \cdot \frac{\text{Mol. Weight chlorine}}{\text{Mol. Weight solvent}}}{(5.2)}$$

The results of this equation are tabulated in Table 5.1. Consider  $\text{CCl}_4$  and  $\text{CHCl}_3$ .

One notes that their concentrations are within 10 % of each other. Assuming their excitation efficiencies are the same, one would expect that their Cl line intensities should be within 10 % of each other. But in fact, this is not the case. One can use data from Tables 4.7 and 5.1 to generate a plot of intensity versus concentration.

This is shown in Figure 5.1. One can clearly see that the Cl line intensity for  $\text{CCl}_4$  is twice that for  $\text{CHCl}_3$ . One possible explanation for this is the scavenging of a Cl atom to form HCl.

Now one can also use equation 5.1 to look at the concentration of carbon in the solvent. Substituting for carbon into equation 5.1, one gets the results listed in Table 5.2. As expected, one notes that the double carbon bond has a carbon concentration of approximately twice that of its single bond counterpart. Now one can also use the data from Tables 5.2 and 5.3 to generate a plot of intensity versus concentration. (CN intensities can be used because carbon can only come from the solvent and for every carbon atom emitted, there is one nitrogen atom emitted.)

This plot is shown in Figure 5.2. Considering the fact that  $\text{CCl}_4$  and  $\text{CHCl}_3$  have

concentrations within approximately 15 % of each other, one would expect that their intensities would be very close to each other. And this is the case. But when one looks at  $C_2Cl_4$  and  $C_2HCl_3$ , there is a different story to tell.  $C_2HCl_3$  has a much higher intensity than that of  $C_2Cl_4$ . The author is not sure why this is happening. Further investigation will hopefully answer this mystery. Nevertheless, using the data from Tables 4.7 and 5.3, one can calculate Cl/CN intensity ratios. This is shown in Table 5.4. One notes that the ratios for the chlorocarbons are approximately twice that of the hydrocarbons. This would also suggest that scavenging of Cl is going on.<sup>31</sup>

**Table 5.1 Concentration of Chlorine in the Solvent Tested**

Solvent	Density of Solvent (g/ml) <sup>41</sup>	Mol. Weight of Solvent <sup>41</sup>	Cl Concentration (g/l)
$CCl_4$	1.58	154	$1.46 \times 10^3$
$CHCl_3$	1.48	119	$1.32 \times 10^3$
$C_2Cl_4$	1.61	166	$1.38 \times 10^3$
$C_2HCl_3$	1.46	131	$1.19 \times 10^3$

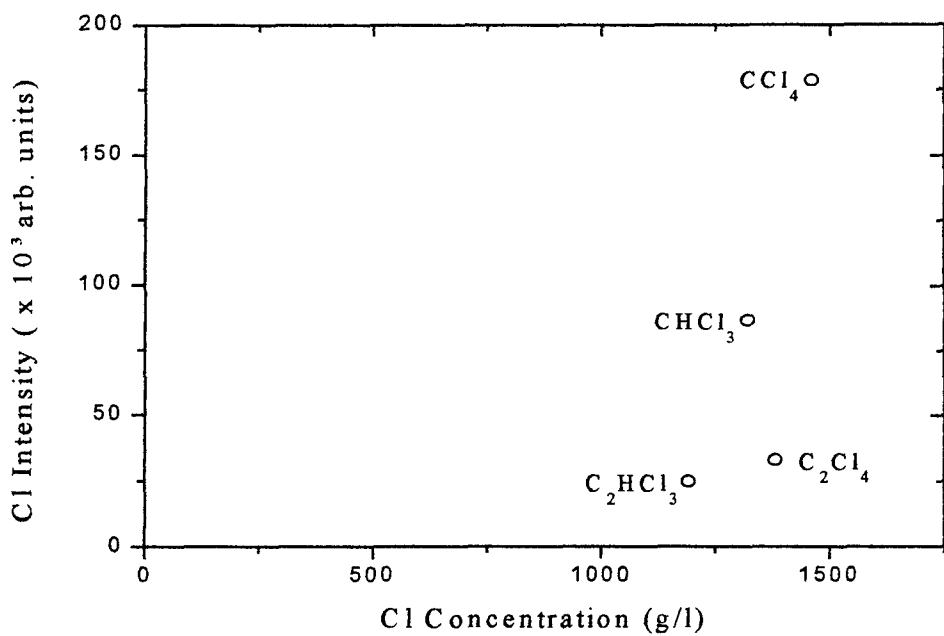


**Figure 5.1 Cl Intensity Versus Cl Concentration at 725.66 nm**

**Table 5.2 Concentration of Carbon in the Solvent Tested**

Solvent	Density of Solvent (g/ml) <sup>41</sup>	Mol. Weight of Solvent <sup>41</sup>	C Concentration (g/l)
CCl <sub>4</sub>	1.58	154	123
CHCl <sub>3</sub>	1.48	119	149
C <sub>2</sub> Cl <sub>4</sub>	1.61	166	233
C <sub>2</sub> HCl <sub>3</sub>	1.46	131	267

**Table 5.3 CN Line Intensities at 359.04 nm for Solvents Tested**

Solvent	Intensity (arb. units)
CCl <sub>4</sub>	$1.75 \times 10^4 \pm 211$
CHCl <sub>3</sub>	$1.66 \times 10^4 \pm 197$
C <sub>2</sub> Cl <sub>4</sub>	$1.24 \times 10^4 \pm 156$
C <sub>2</sub> HCl <sub>3</sub>	$2.36 \times 10^4 \pm 220$

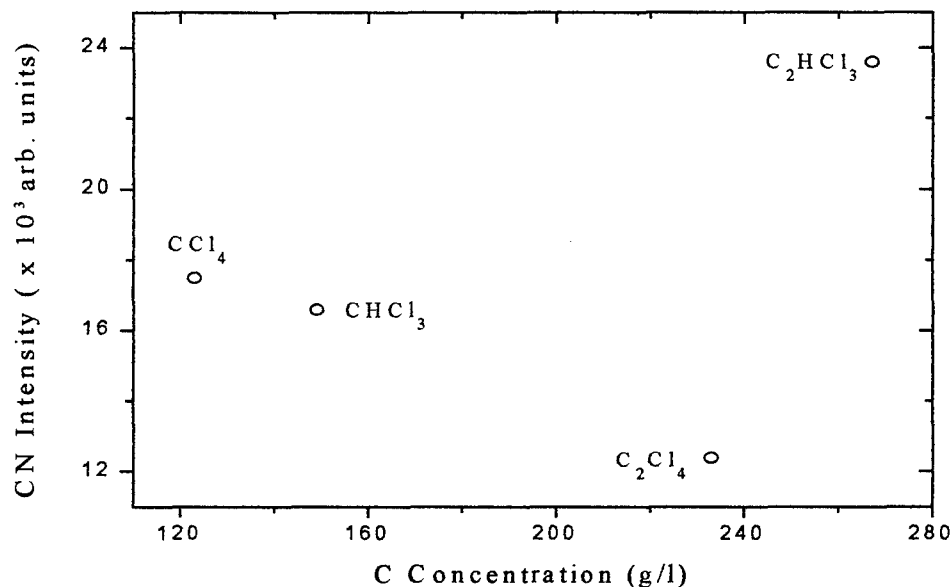


**Figure 5.2 CN Intensity Versus C Concentration**

**Table 5.4 Cl/CN Ratios for Solvents Tested**

Solvent	Cl/CN Ratio
CCl <sub>4</sub>	10.2
CHCl <sub>3</sub>	5.23
C <sub>2</sub> Cl <sub>4</sub>	2.68
C <sub>2</sub> HCl <sub>3</sub>	1.06

Let's revisit equation 5.1. Bauch et. al., using argon as the third body, expressed the rate constant as:<sup>45</sup>

$$k = 2.60 \times 10^{13} \exp(9940 / T) \text{ cm}^6 \text{ mole}^{-2} \text{ s}^{-1} \quad (5.3)$$

Assuming a temperature (upon recombination) of 1,000 K, the rate constant

$$k = 5.39 \times 10^{17} \text{ cm}^6 \text{ mole}^{-2} \text{ s}^{-1} \approx 1.49 \times 10^{-30} \text{ cm}^6 \text{ molecule}^{-2} \text{ s}^{-1}$$

equation 5.1 can be written as a pseudo-second order equation. If the concentration of argon is kept constant,

$$\frac{d[HCl]}{dt} \approx k' [H] [Cl] \quad (5.4)$$

where  $k' = k [Ar]$ . Using the ideal gas law ( $p = NkT$ ) with  $p = 1 \text{ atm}$  and  $T = 1,000 \text{ K}$ ,  $N \approx [Ar] = 7.34 \times 10^{18} \text{ cm}^{-3}$ . Hence,  $k' \approx 1.09 \times 10^{-11} \text{ cm}^3 \text{ molecule}^{-2} \text{ s}^{-1}$ . As one can see, this is a fairly fast rate constant and recombination should occur rather quickly. This lends credence to the idea that H is scavenging Cl to form  $\text{HCl}$ .<sup>3,31,46</sup>

Back in Chapter 4, it was revealed that  $\text{CCl}_4$  and  $\text{CHCl}_3$  had only the tiniest hint of the  $\text{C}_2$  Swan bands. This should come as no surprise. When  $\text{C}_2\text{Cl}_4$  and  $\text{C}_2\text{HCl}_3$  dissociate, there will be excess  $\text{C}_2$  molecules around to form the  $\text{C}_2$  Swan bands. However, when  $\text{CCl}_4$  and  $\text{CHCl}_3$  dissociate, there are only C atoms available, not  $\text{C}_2$ . To form the  $\text{C}_2$  Swan bands from  $\text{CCl}_4$  and  $\text{CHCl}_3$ , these C atoms must recombine to form  $\text{C}_2$ . The chance of this happening is relatively low because carbon is most likely to recombine with H (Cl) to form CH (CCl), i.e., the heats of formation (enthalpy) are  $\Delta H_{\text{CCl}} = 111 \text{ kcal/mole}$ ,  $\Delta H_{\text{CH}} = 142 \text{ kcal/mole}$ , and  $\Delta H_{\text{C}_2} = 200 \text{ kcal/mole}$ .<sup>47</sup> Unfortunately, neither CH or CCl were detected by this technique.

## 5.4 Saturated Solvent Detection

As seen in Chapter 4, saturated solvent solutions were not detectable with LIBS. They basically mirrored the water spectrum. However, there is a way to determine if saturated solvent detection was even possible in the first place. Using data from Table 4.7 along with the origin as a data point, one can generate a calibration curve for each solvent in question. This is shown in Figures 5.3 through 5.6. Detection limits can be calculated using equation 4.1 and are shown in Table 5.5. Looking back in Ch. 3, one can see that the detection limits for the solvents (chlorine) in question are much higher than their solubility limits. Hence, one would not be able to detect the solvent (chlorine) in the saturated solution.<sup>31</sup>

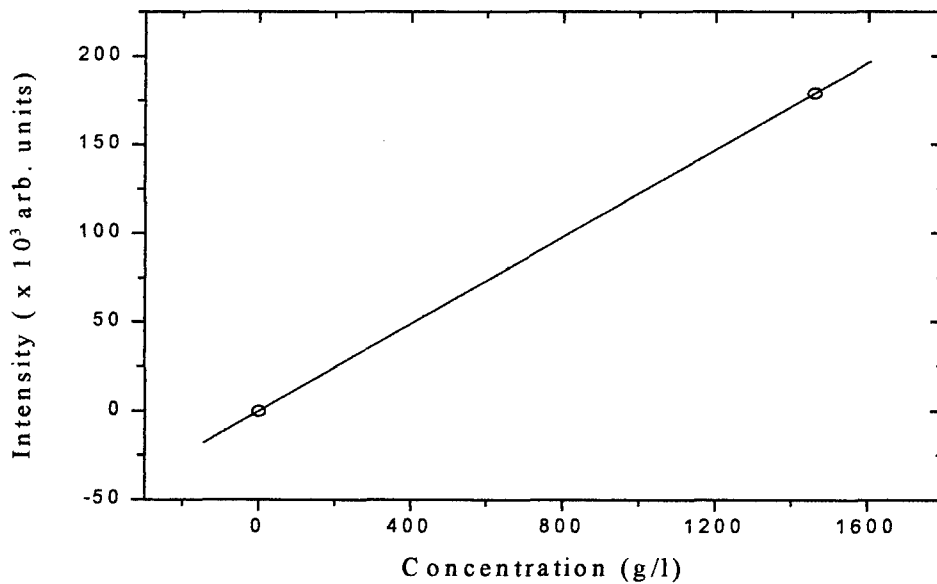


**Figure 5.3 Simulated Calibration Curve for CCl<sub>4</sub>**

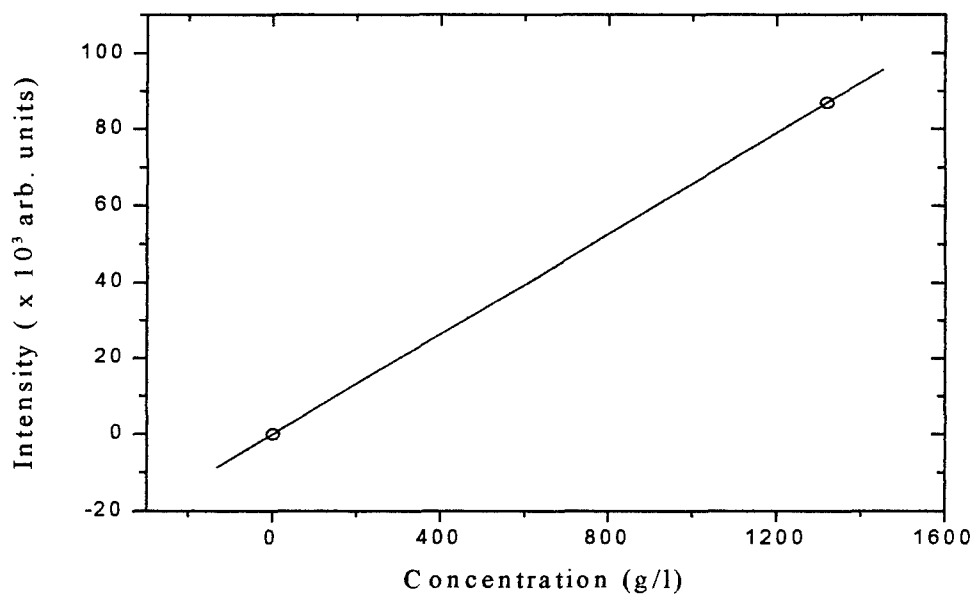


**Figure 5.4 Simulated Calibration Curve for  $\text{CHCl}_3$**

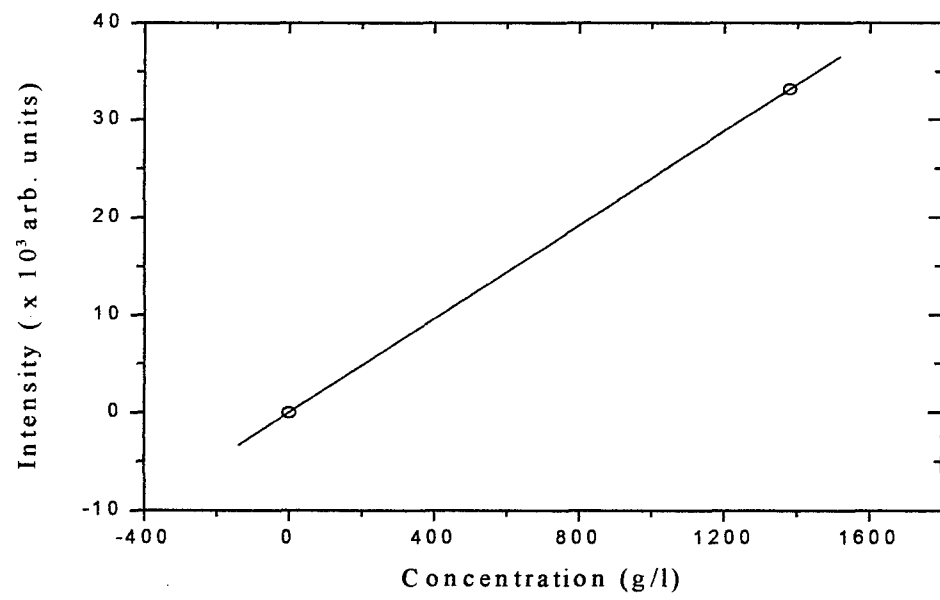


**Figure 5.5 Simulated Calibration Curve for  $\text{C}_2\text{Cl}_4$**

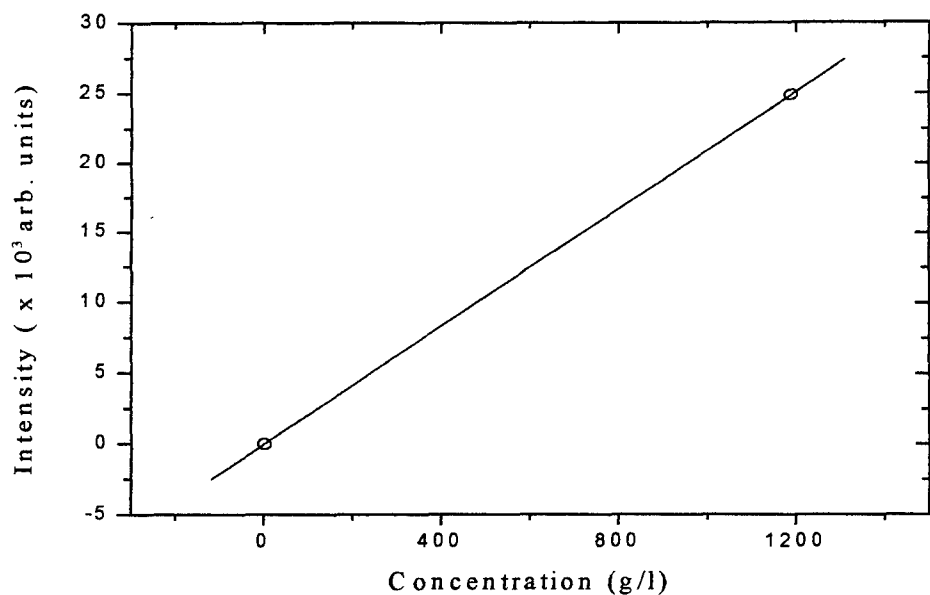


**Figure 5.6 Simulated Calibration Curve for  $\text{C}_2\text{HCl}_3$**

**Table 5.5 Calibration Curve Data for Chlorine**

Solvent	Noise N	Slope S (l/g)	$C_L$ (g/l)
$\text{CCl}_4$	$1.62 \times 10^3$	123	39.5
$\text{CHCl}_3$	$1.01 \times 10^3$	65.8	46.0
$\text{C}_2\text{Cl}_4$	588	24.1	73.2
$\text{C}_2\text{HCl}_3$	588	20.9	84.4

## **VI. Conclusions and Recommendations**

This study has presented the spectroscopic technique known as Laser-Induced Breakdown Spectroscopy. It has been applied to nickel in solution. Limits of detection ranged between 29.4 and 56.1 mg/l. Detection limits of the sort should provide a moderate degree of analytical performance for such EPA compliance issues as groundwater monitoring. LIBS was also applied to solvents such as  $\text{CCl}_4$ ,  $\text{CHCl}_3$ ,  $\text{C}_2\text{Cl}_4$ , and  $\text{C}_2\text{HCl}_3$ . Cl, C<sub>2</sub>, and CN bands were detected in the pure solvent solutions. However, solvent detection was not possible for the saturated solutions. Continued work with pure solvent solutions may lead to future work with saturated solvent solutions.

As with any experiment, there probably are some improvements that can be made to the equipment. The following recommendations are suggestions that might even help lower detection limits.

1. A Nd:YAG laser has served as the main source of excitation throughout the entire course of this experiment. While it has fulfilled its role, the addition of a second laser could be used to increase emission from the plasma and thereby lower detection limits. Once the plasma has been initiated by the first pulse, a second pulse would be used to further excite the plasma. However, the second pulse would only interact with the plasma above the sample. Of course, necessary steps would have to be taken to ensure synchronization of the two-laser system.<sup>21</sup>
2. Optical alignment of the laser axis is the key to good quantitative results. The use of focusing lenses and 2-D translation stages to perform this task was difficult at best. One might instead use a fiber optic cable both to deliver laser radiation to the solution sample and to collect light emitted from the focal volume.<sup>12</sup>

3. In this study, detection of the spark plasma was triggered off of the Nd:YAG laser. Unfortunately, the firing of the laser did not always result in breakdown of the liquid. Therefore, an optical trigger system may be more appropriate for this application. Signal processing would only take place when the laser spark was observed. An optical trigger detector is available commercially through EG&G PARC.<sup>44</sup>
4. For those who are not concerned with in situ detection, one might try performing this experiment in a vacuum. This should reduce the background signal found at atmospheric pressure and thus lower detection limits.<sup>19</sup>
5. Saturated solvent detection proved to be uneventful in this experiment. However, one might try running the experiment in reverse, starting with the pure solvent. Next, a small amount of water would be added to the solvent and the experiment would be run again. This would continue until the solvent itself was saturated. Any change in spectral features (from one solution to the next) could be indicative of the amount of solvent in the solution.<sup>3</sup>

## **Appendix A - Area/Noise Ratios**

The area/noise ratio is readily calculated. First of all, the area is simply the area under the curve (peak). A nice software package can easily perform the integration. For this study, the 361.94 nm peak for Ni (UV) was used. Next, noise is obtained from a portion of the Ni spectrum that's essentially featureless. For this region, the intensities and wavelengths are known so that the multiplication of the two give rise to an area for the noise. Finally, take the standard deviation of the noise values. Once completed, one can easily calculate the area/noise ratios as seen in the table below. Units for area and noise are in arb. units - nm.<sup>46</sup>

**Table A.1 Area/Noise Ratios for Ni (UV) at 361.94 nm**

<b>Gate Width (μs)</b>	<b>Time Delay (μs)</b>	<b>Area</b>	<b>Noise</b>	<b>A/N Ratio</b>
10	1	$4.40 \times 10^5$	$2.91 \times 10^4$	15.1
10	3	$4.84 \times 10^4$	$2.58 \times 10^3$	18.8
10	6	$1.92 \times 10^4$	$1.29 \times 10^3$	14.9
10	9	$9.30 \times 10^3$	$2.57 \times 10^3$	3.62
10	12	$4.65 \times 10^3$	$1.71 \times 10^3$	2.72
3	0.5	$1.37 \times 10^4$	$3.39 \times 10^3$	4.04
7	0.5	$1.54 \times 10^4$	$2.76 \times 10^3$	5.58
10	0.5	$1.75 \times 10^4$	$1.70 \times 10^3$	10.3
14	0.5	$1.63 \times 10^4$	$1.83 \times 10^3$	8.91
18	0.5	$1.30 \times 10^4$	$1.76 \times 10^3$	7.39

## **Appendix B - Systematic Error**

One source of error in the experiment is systematic error. They cause the results of replicate measurements to be either high or low. There are three types of systematic error. The first type is instrument error. They are caused by imperfections in the measuring devices used in the experiment. For example, pipets and volumetric flasks have volumes slightly different from that indicated by their graduations. The next type of error is the method error. They arise from the nonideal chemical behavior of the reagents upon which analysis is based. Sources of nonideality include instability of the species tested and the possible occurrence of side reactions that interfere with the measurement process. Finally, the last type of systematic error is personal error. They result from the carelessness and inattention of the experimenter. Additionally, personal error can arise from bias on the part of the observer. Most people have a natural tendency to estimate measurements in such a way as to improve their results.<sup>48</sup> The author of this study suspects that the systematic error in this experiment probably outweighs the statistical error inherent in the results.

## **Appendix C - Determination of Noise (N) at Various Concentrations**

Noise is calculated by the following means. For a portion of the Ni spectrum that is essentially featureless, intensity values are known. N is the standard deviation of those values.<sup>6</sup> Units for N are in arbitrary units.

**Table C.1 Noise Levels at Various Concentrations**

<b>Gate Width (μs)</b>	<b>Time Delay (μs)</b>	<b>Excitation</b>	<b>Concentration (mg/l)</b>	<b>N</b>
50	8	IR	1000	8.38
50	8	IR	200	12.0
50	8	IR	100	10.4
10	3	UV	1000	20.9
10	3	UV	500	17.2
10	3	UV	200	27.4
10	3	UV	125	14.6
10	3	UV	100	11.7
10	3	UV	62.5	18.9
10	3	UV	50	20.0

## **Appendix D - Spectra for Solvents Tested**

Displayed in this appendix is a series of 40 spectra taken of the four solvents studied in this research. All spectra are taken at a 50  $\mu\text{m}$  slit width unless otherwise noted. Figures D.1 through D.8 show two chlorine peaks at 725.66 and 754.71 nm. These figures also depict second order cyanogen bands as well as nitrogen lines. Line assignments are listed in Table 4.6. Figures D.9 through D.16 show the 656.29 hydrogen-alpha peak. Figures D.17 through D.28 introduce the C<sub>2</sub> Swan bands. Line assignments are given in Table 4.8. Note that Figures D.26 and D.28 picture the 486.13 nm hydrogen peak. Finally, Figures D.29 through D.40 show the cyanogen bands. Line assignments are listed in Table 4.9.

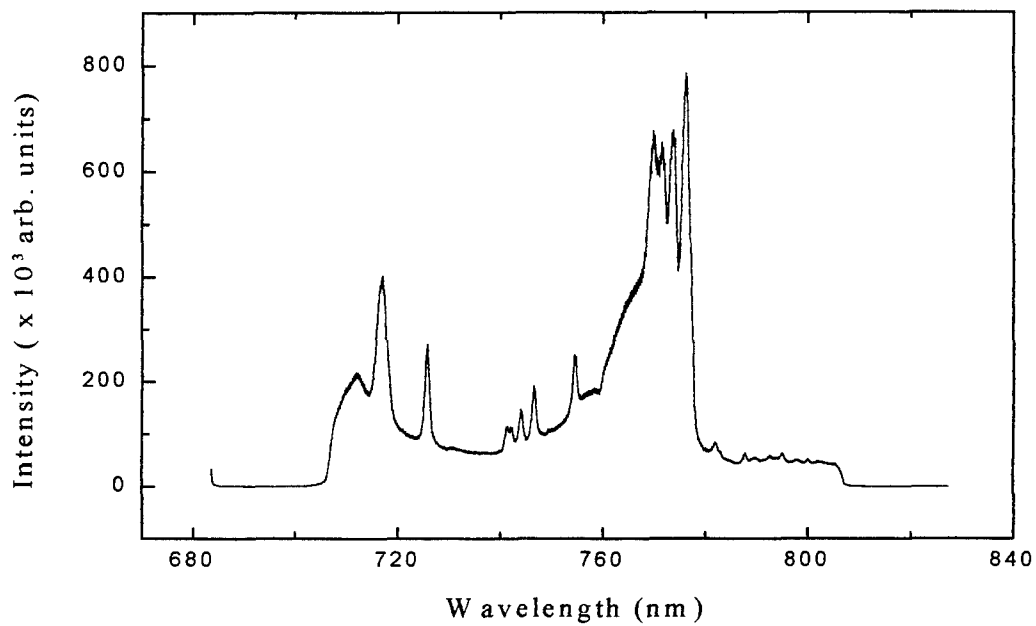


**Figure D.1**  $\text{CCl}_4$  Spectrum Covering 705 - 805 nm

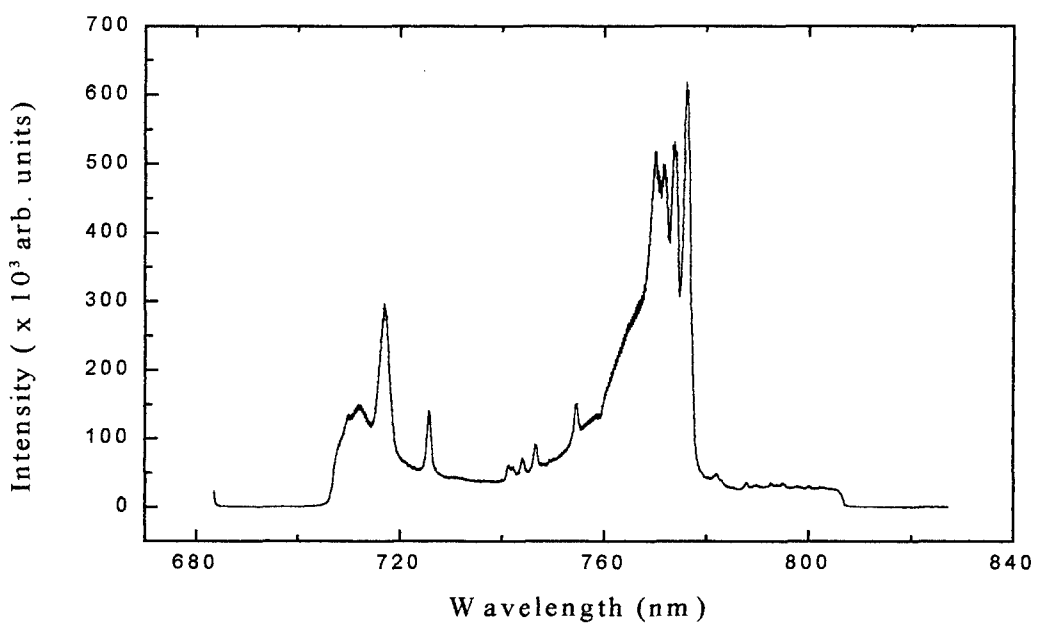


**Figure D.2**  $\text{CHCl}_3$  Spectrum Covering 705 - 805 nm

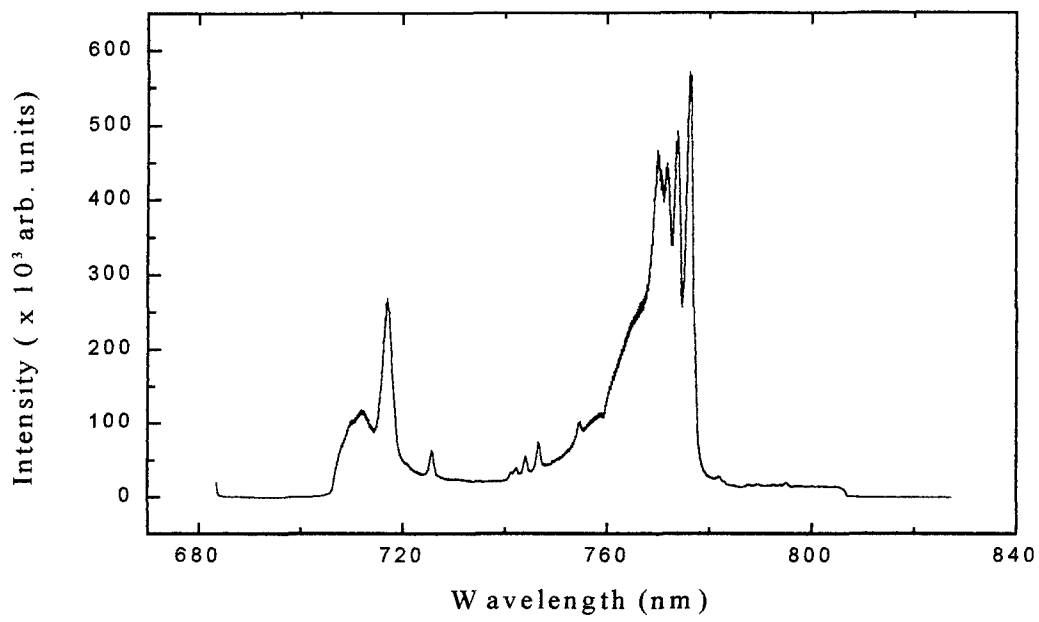


**Figure D.3  $\text{C}_2\text{Cl}_4$  Spectrum Covering 705 - 805 nm**

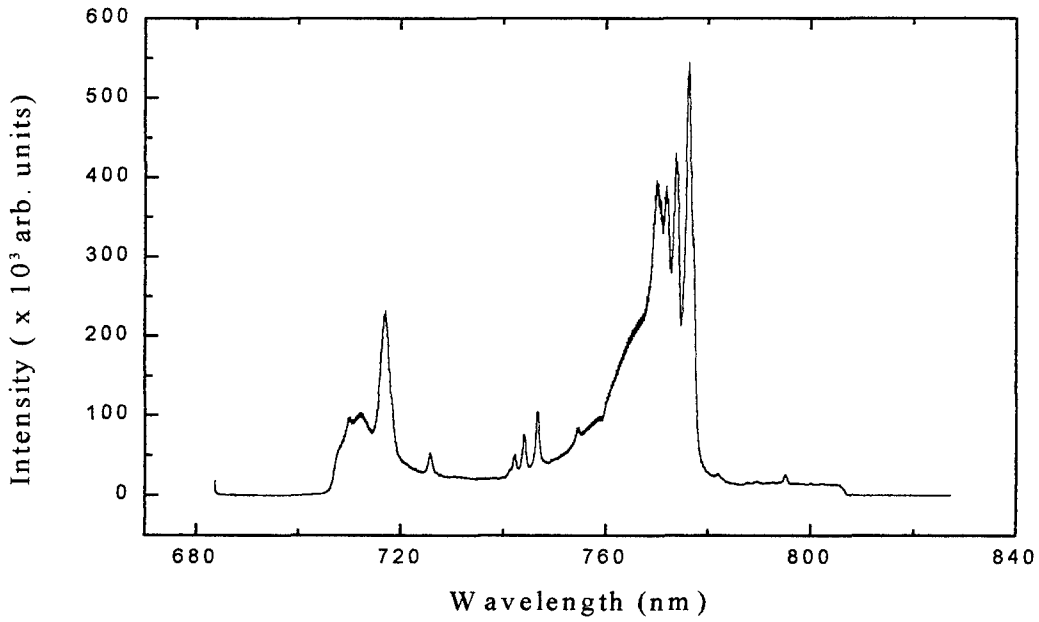


**Figure D.4  $\text{C}_2\text{HCl}_3$  Spectrum Covering 705 - 805 nm**

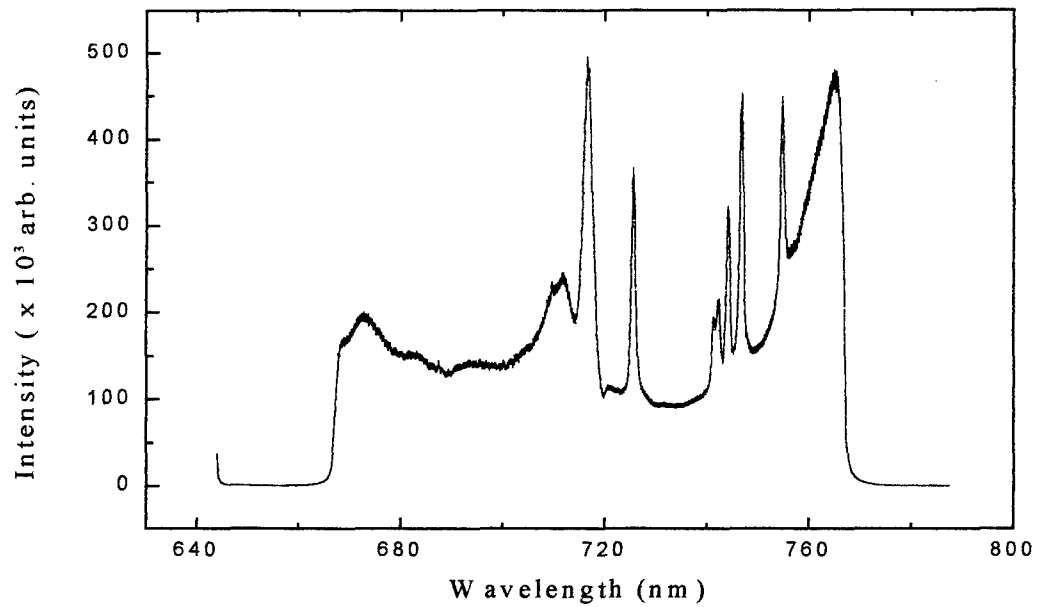


**Figure D.5  $\text{CCl}_4$  Spectrum Covering 665 -765 nm (100  $\mu\text{m}$  slit width)**

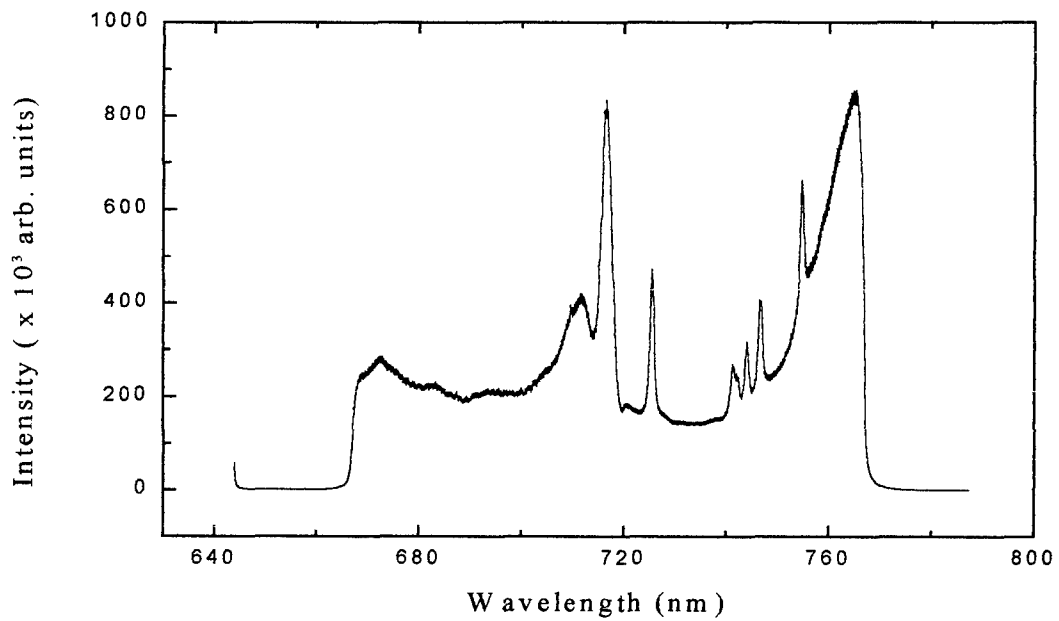


**Figure D.6  $\text{CHCl}_3$  Spectrum Covering 665 - 775 nm (100  $\mu\text{m}$  slit width)**

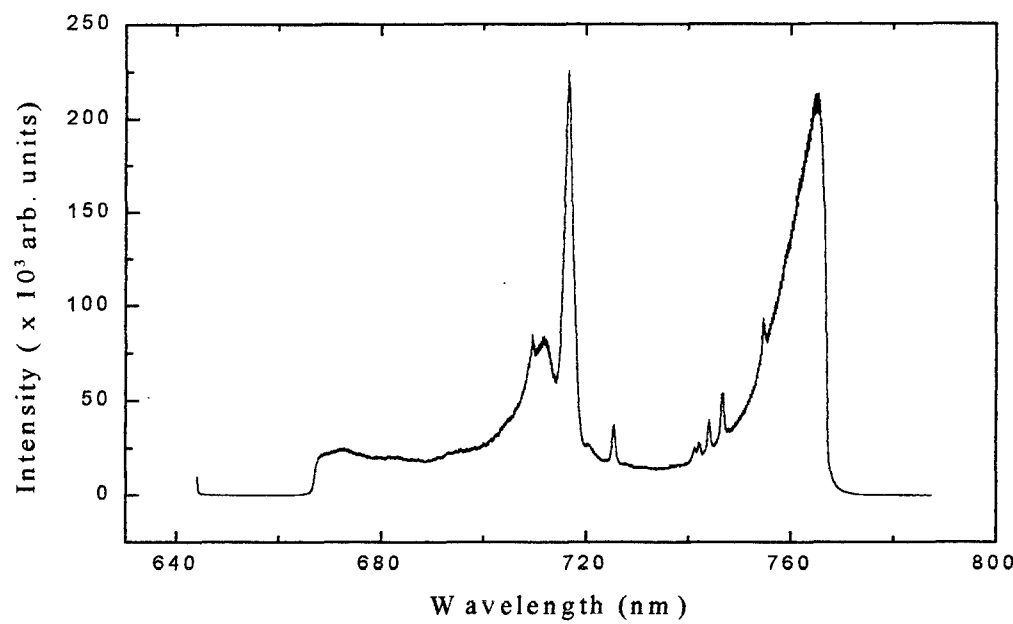


**Figure D.7**  $\text{C}_2\text{Cl}_4$  Spectrum Covering 665 - 775 nm

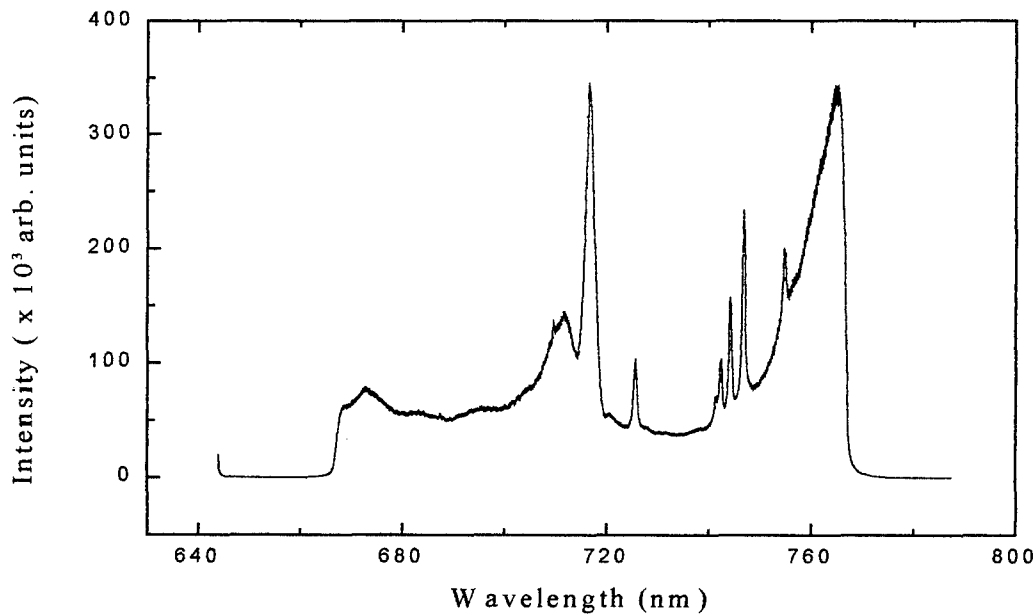


**Figure D.8**  $\text{C}_2\text{HCl}_3$  Spectrum Covering 665 - 775 nm

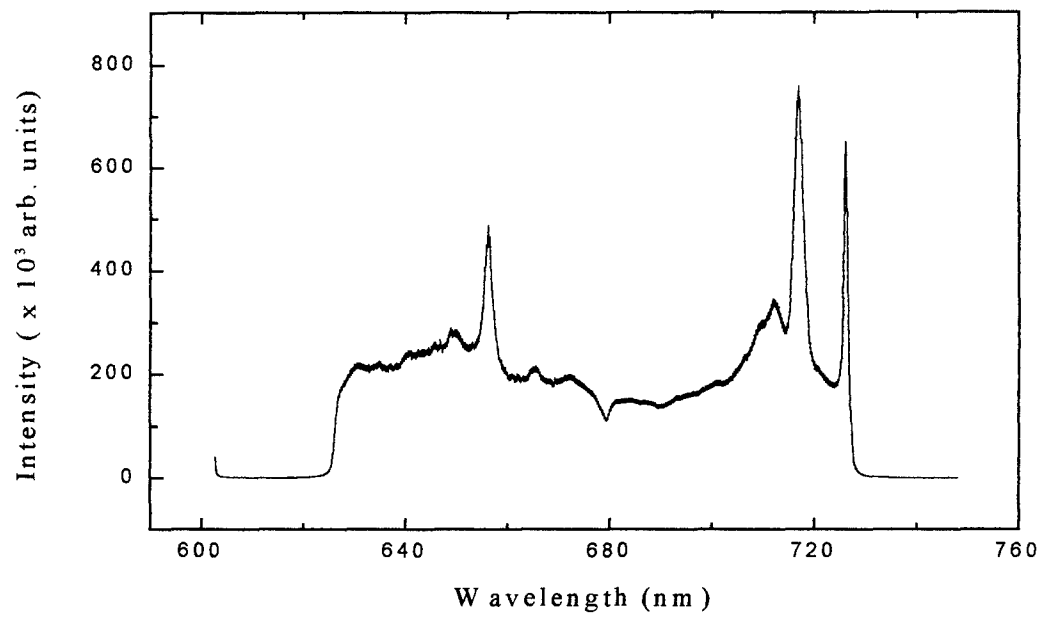


**Figure D.9 CCl<sub>4</sub> Spectrum Covering 625 - 725 nm (100  $\mu\text{m}$  slit width)**

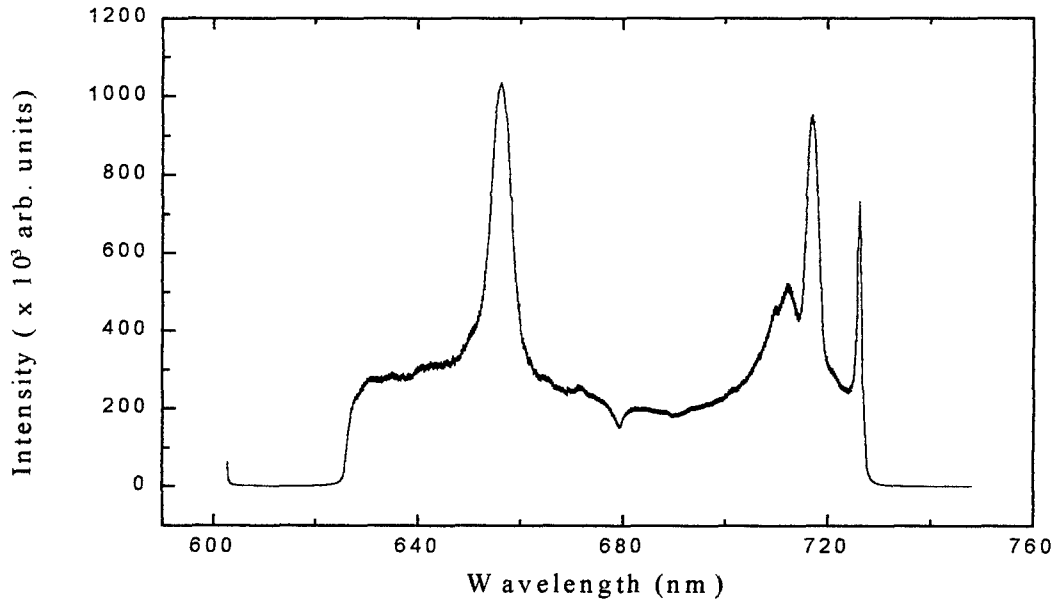


**Figure D.10 CHCl<sub>3</sub> Spectrum Covering 625 - 725 nm (100  $\mu\text{m}$  slit width)**

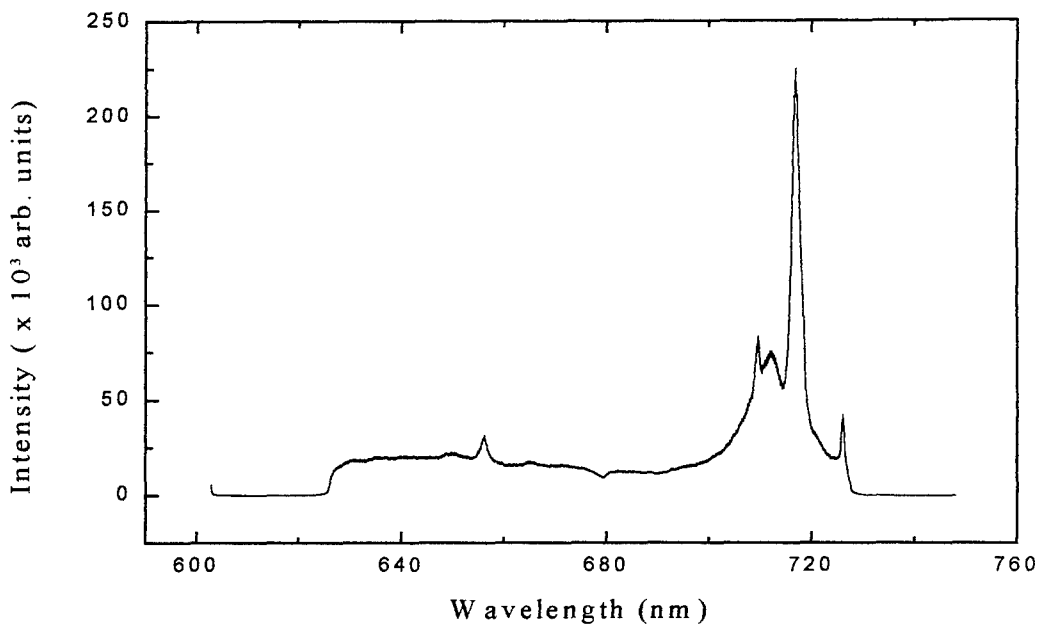


**Figure D.11  $\text{C}_2\text{Cl}_4$  Spectrum Covering 625 - 725 nm**

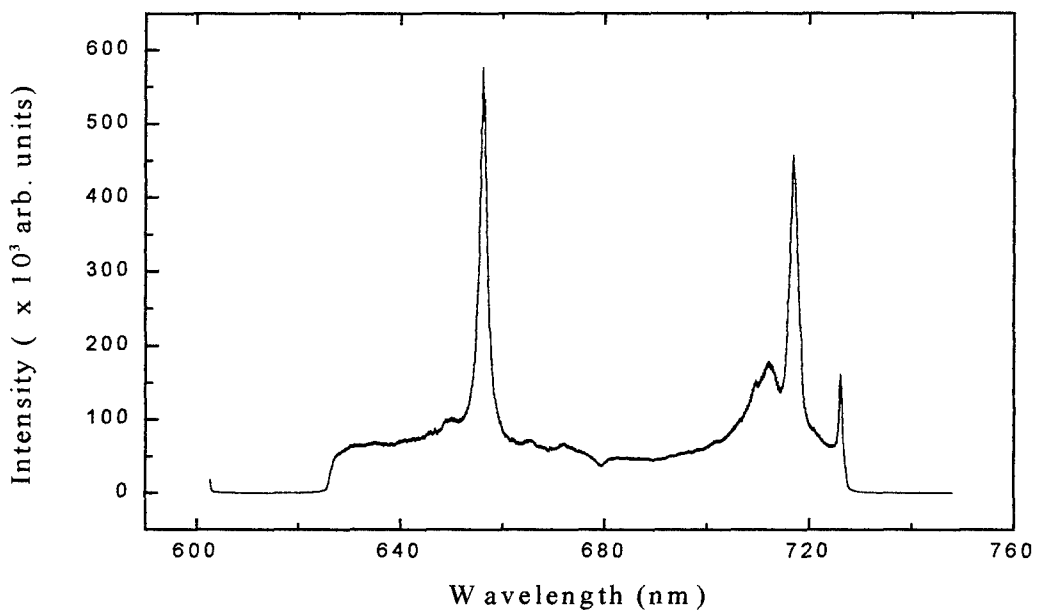


**Figure D.12  $\text{C}_2\text{HCl}_3$  Spectrum Covering 625 - 725 nm**

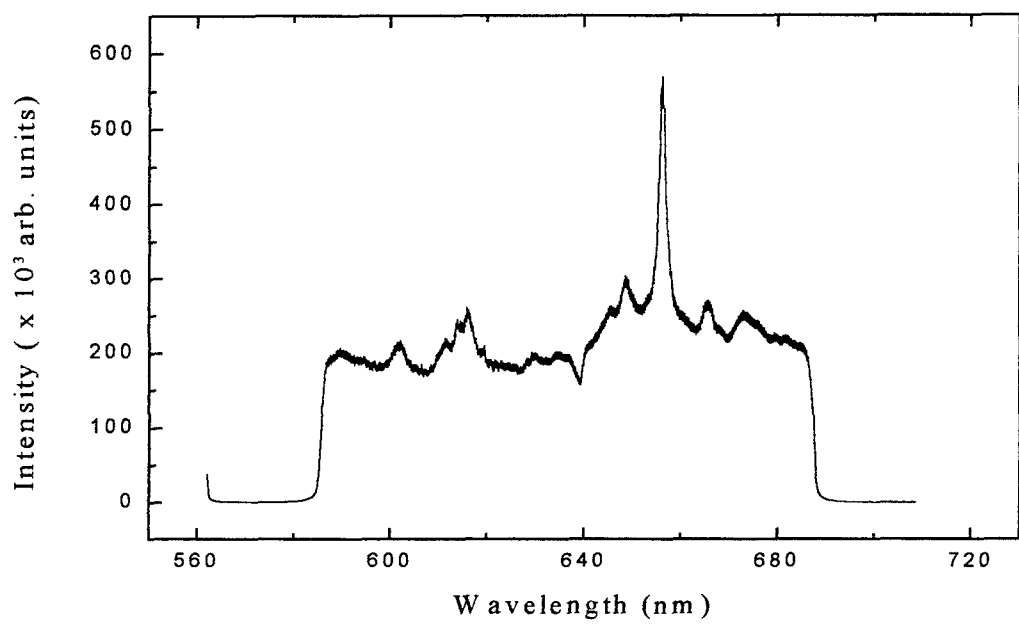


**Figure D.13 CCl<sub>4</sub> Spectrum Covering 585 - 685 nm (100  $\mu\text{m}$  slit width)**

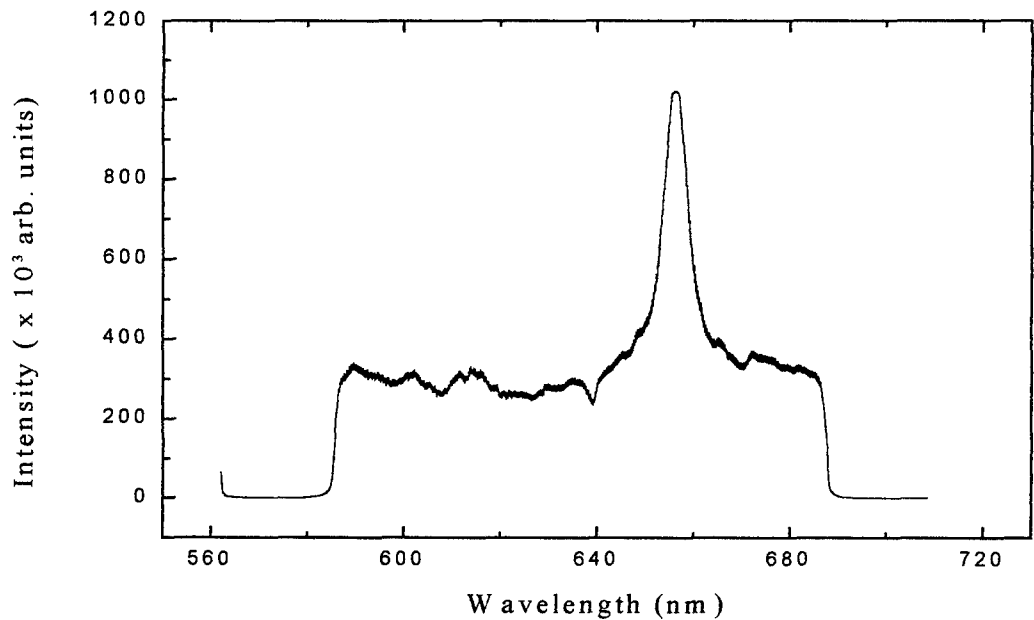


**Figure D.14 CHCl<sub>3</sub> Spectrum Covering 585 - 685 nm (100  $\mu\text{m}$  slit width)**

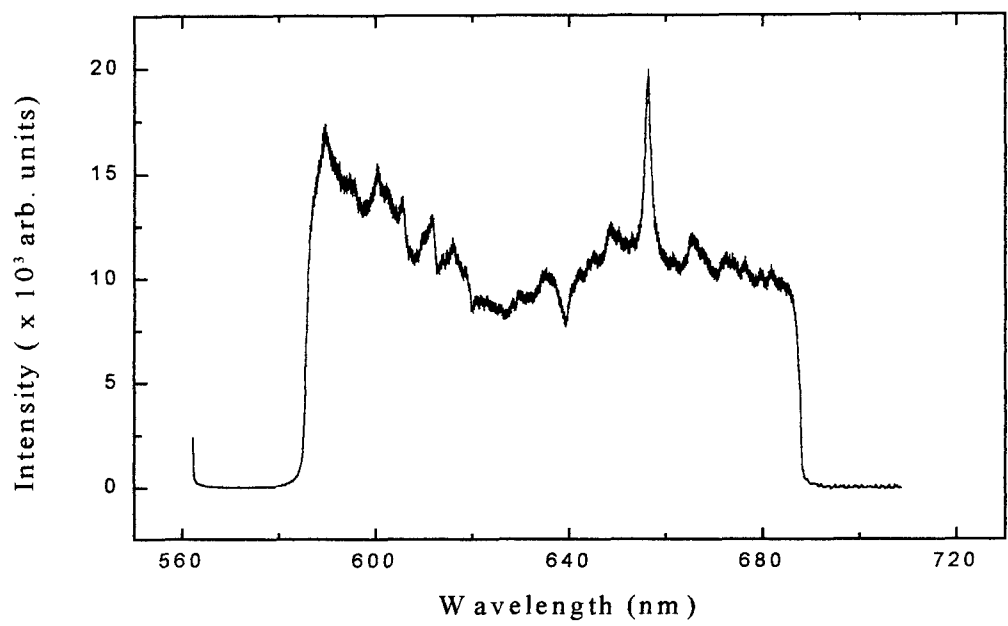


**Figure D.15**  $\text{C}_2\text{Cl}_4$  Spectrum Covering 585 - 685 nm

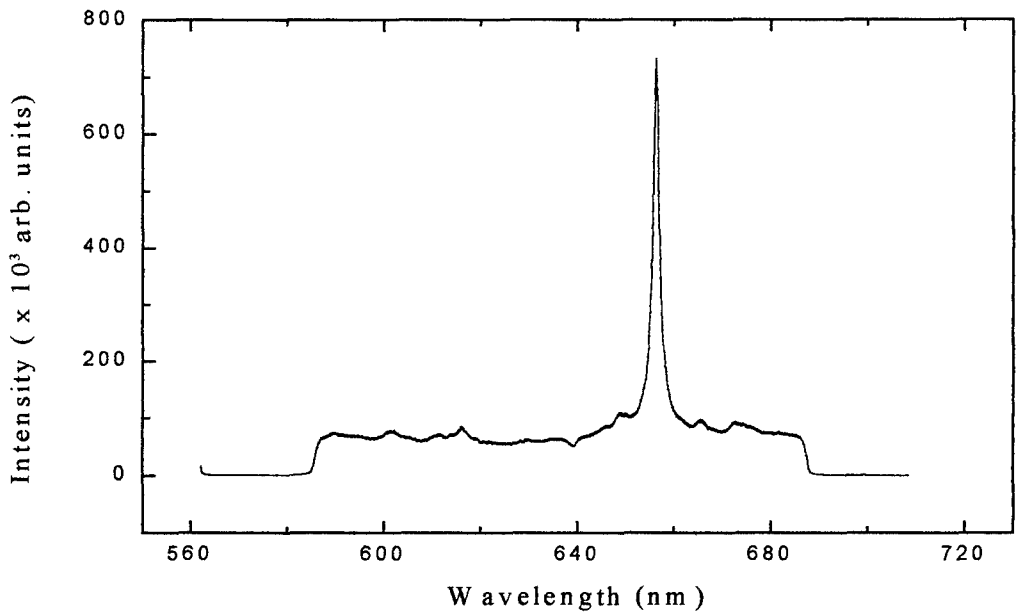


**Figure D.16**  $\text{C}_2\text{HCl}_3$  Spectrum Covering 585 - 685 nm

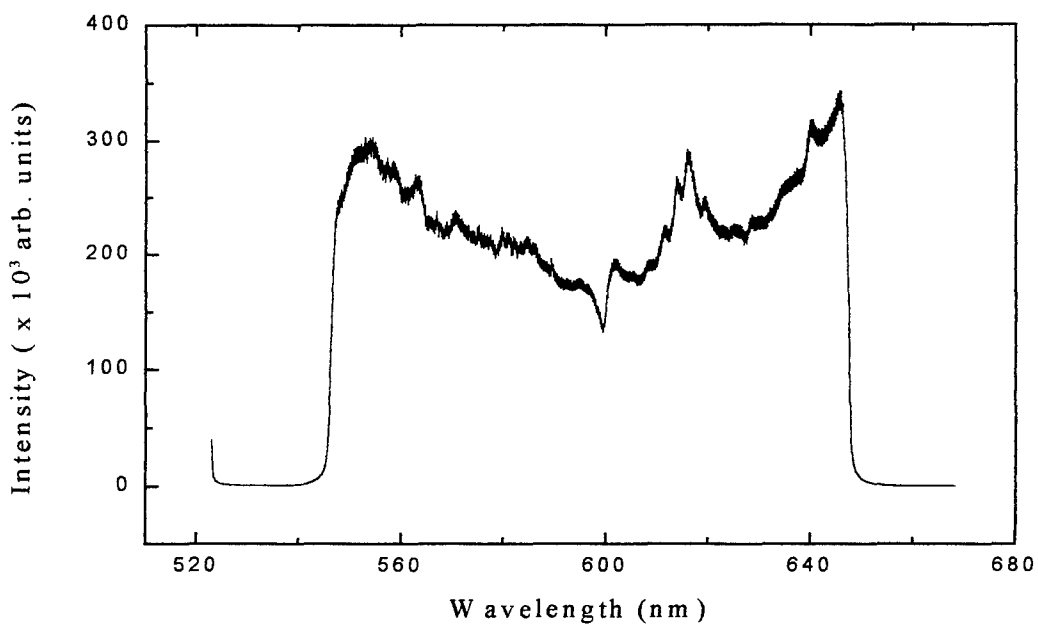


**Figure D.17 CCl<sub>4</sub> Spectrum Covering 545 - 645 nm (100  $\mu\text{m}$  slit width)**

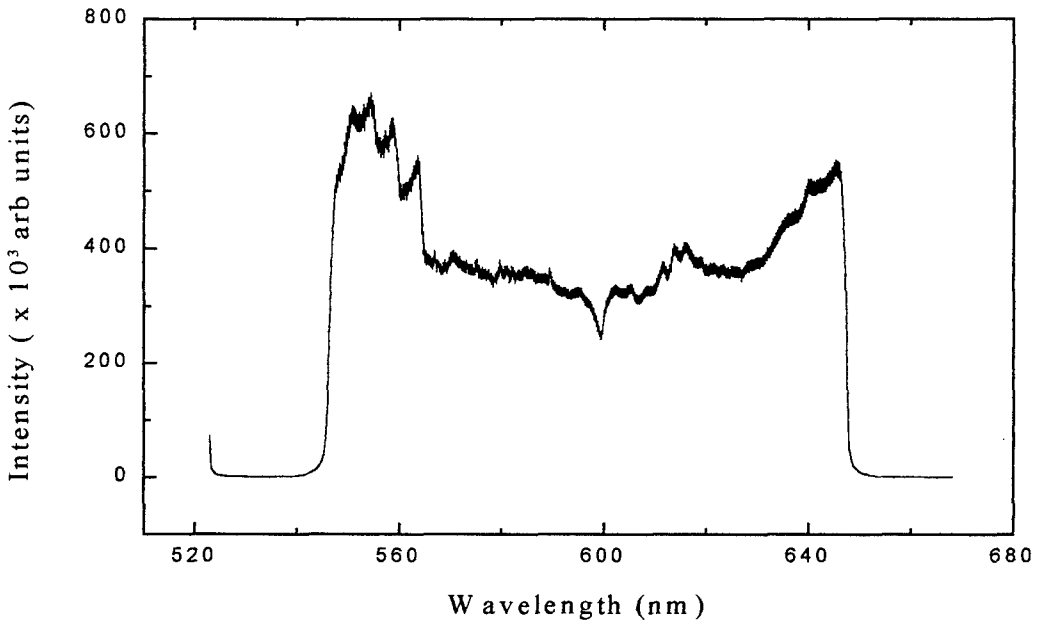


**Figure D.18 CHCl<sub>3</sub> Spectrum Covering 545 - 645 nm (100  $\mu\text{m}$  slit width)**

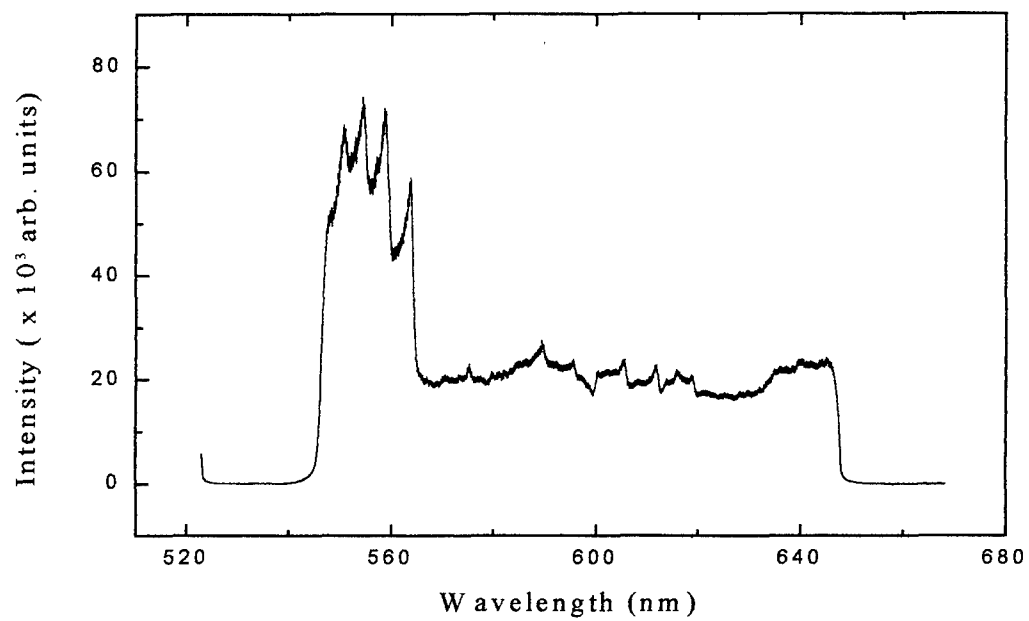


**Figure D.19  $\text{C}_2\text{Cl}_4$  Spectrum Covering 545 - 645 nm**

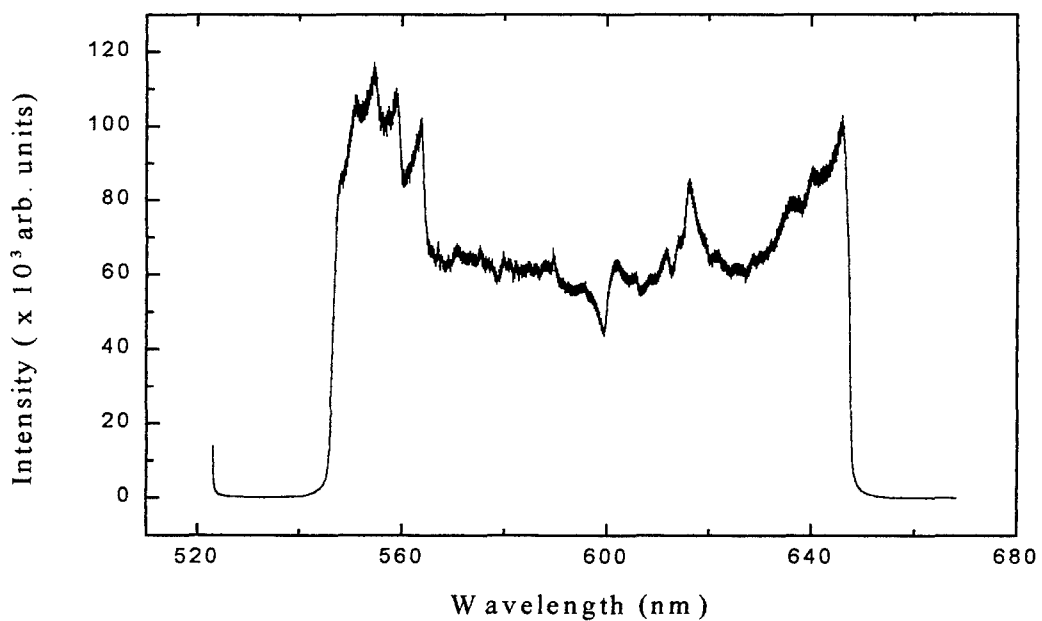


**Figure D.20  $\text{C}_2\text{HCl}_3$  Spectrum Covering 545 - 645 nm**

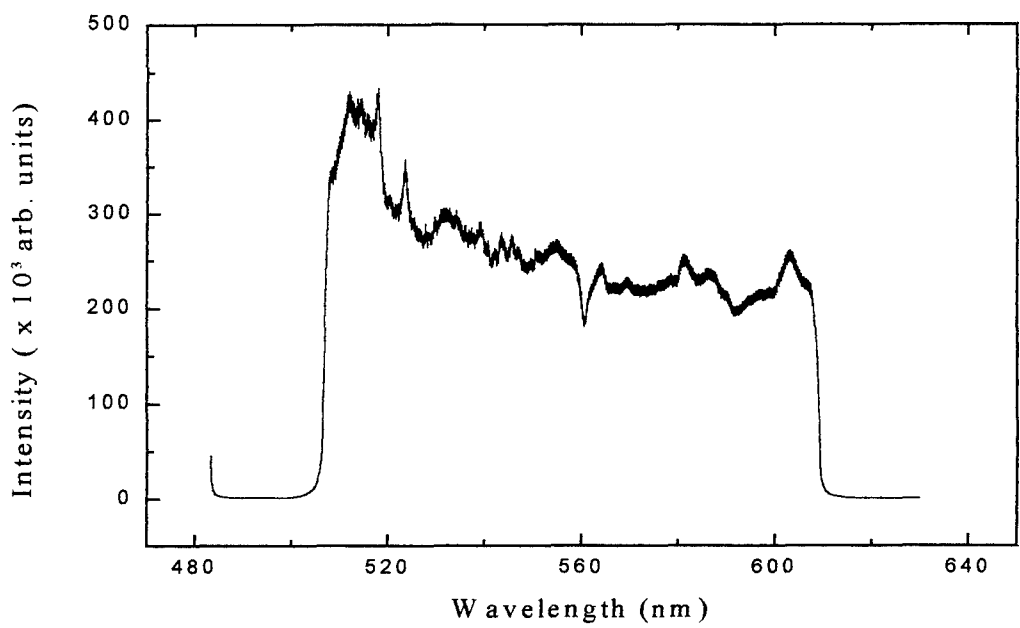


**Figure D.21 CCl<sub>4</sub> Spectrum Covering 505 - 605 nm (100  $\mu\text{m}$  slit width)**

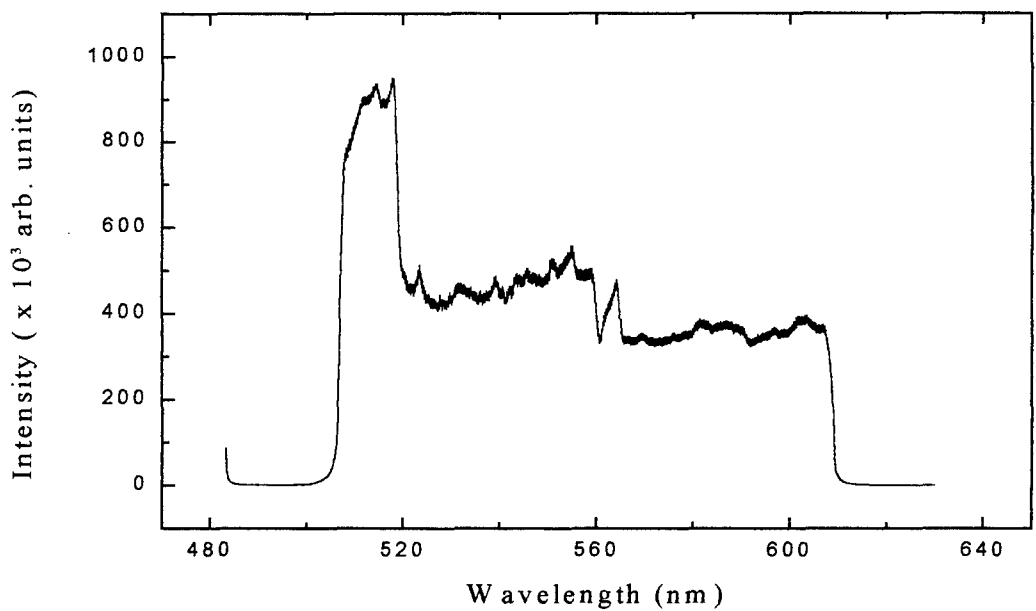


**Figure D.22 CHCl<sub>3</sub> Spectrum Covering 505 - 605 nm (100  $\mu\text{m}$  slit width)**

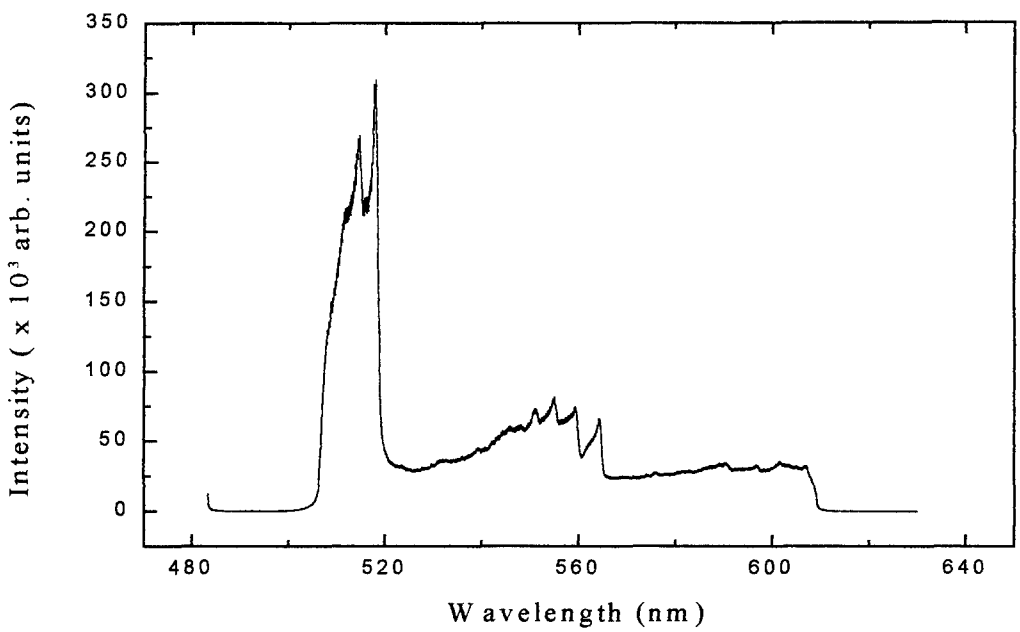


**Figure D.23**  $\text{C}_2\text{Cl}_4$  Spectrum Covering 505 - 605 nm

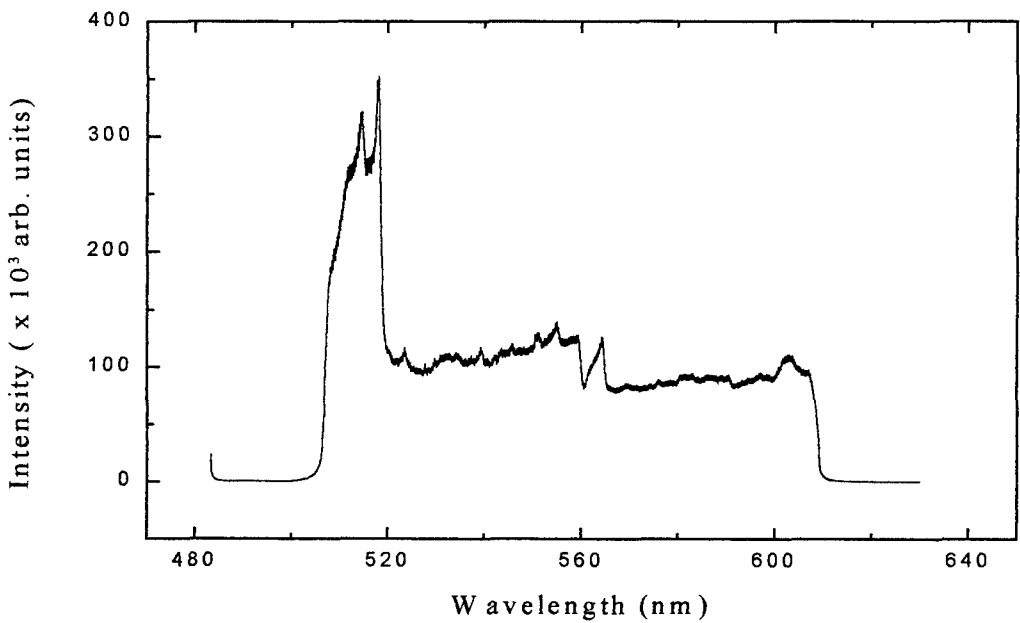


**Figure D.24**  $\text{C}_2\text{HCl}_3$  Spectrum Covering 505 - 605 nm

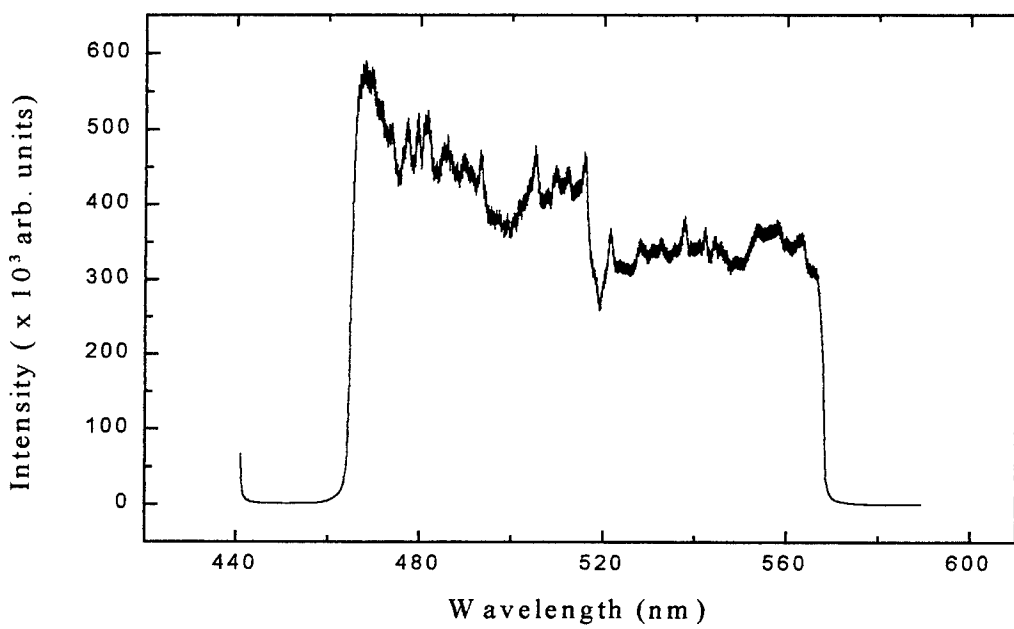


**Figure D.25 CCl<sub>4</sub> Spectrum Covering 465-565 nm (100  $\mu\text{m}$  slit width)**

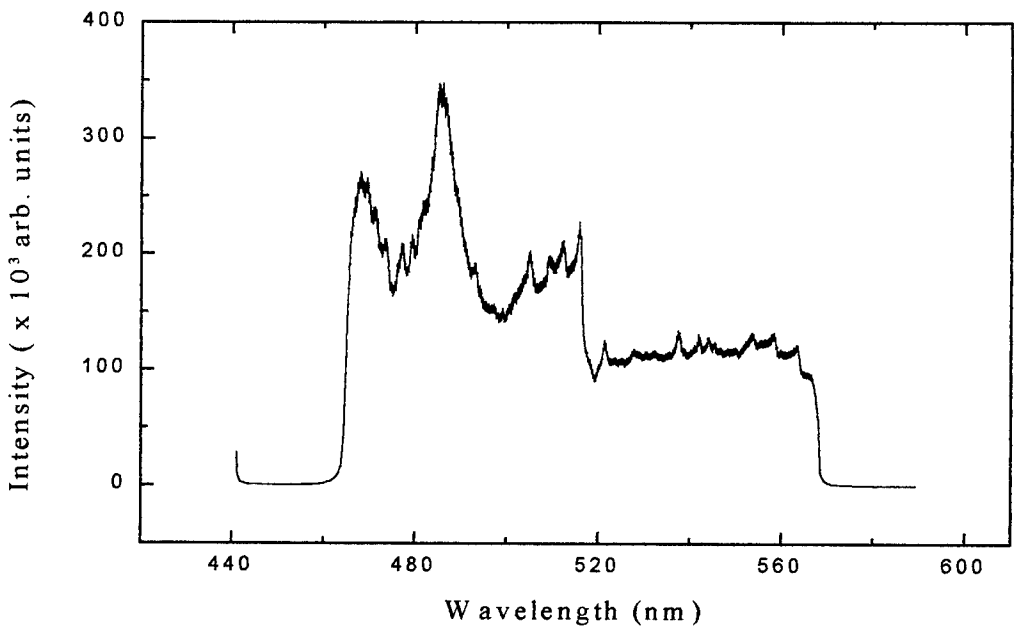


**Figure D.26 CHCl<sub>3</sub> Spectrum Covering 464-565 nm (20  $\mu\text{m}$  slit width)**

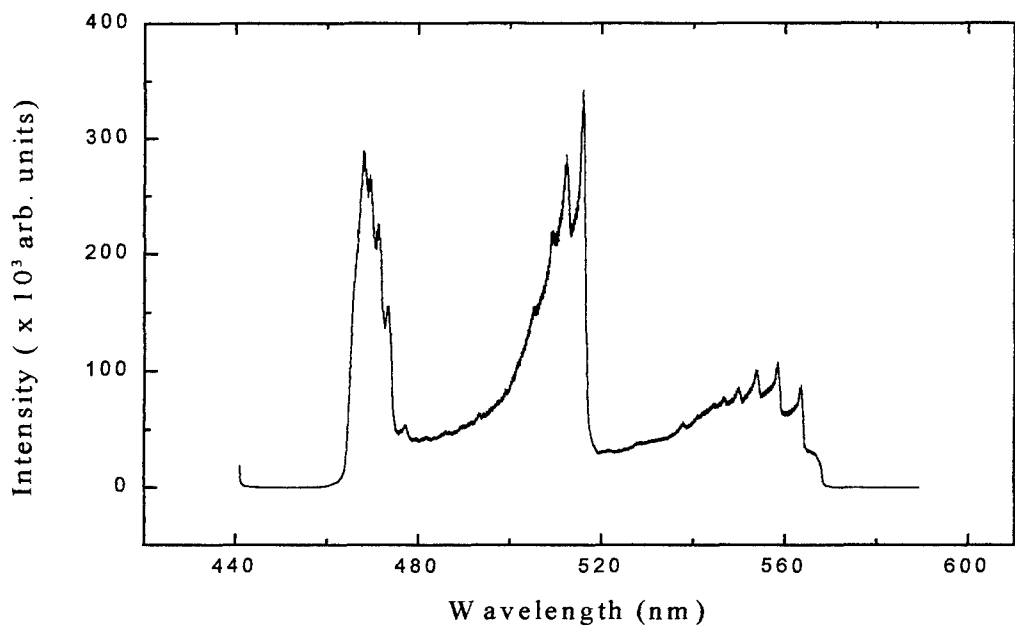


**Figure D.27  $\text{C}_2\text{Cl}_4$  Spectrum Covering 465-565 nm**

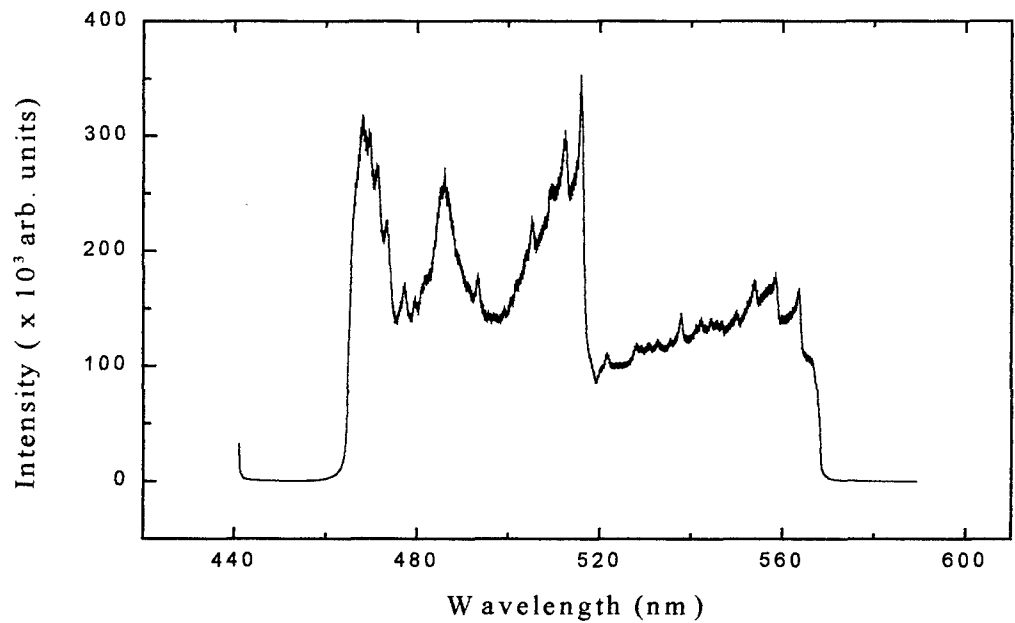


**Figure D.28  $\text{C}_2\text{HCl}_3$  Spectrum Covering 465 - 565 nm**

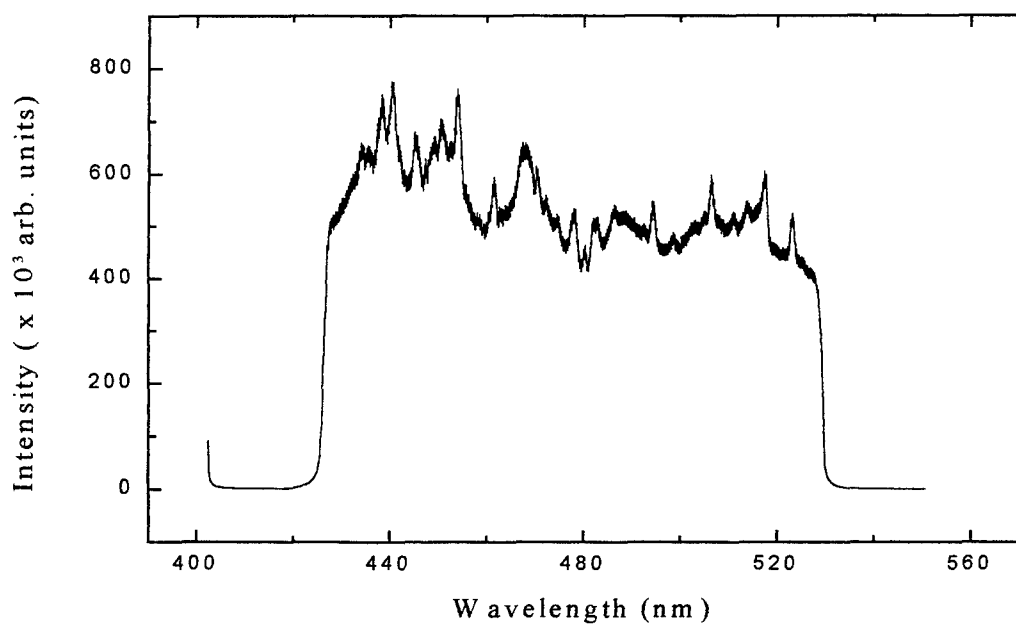


**Figure D.29**  $\text{CCl}_4$  Spectrum Covering 425 - 525 nm (100  $\mu\text{m}$  slit width)

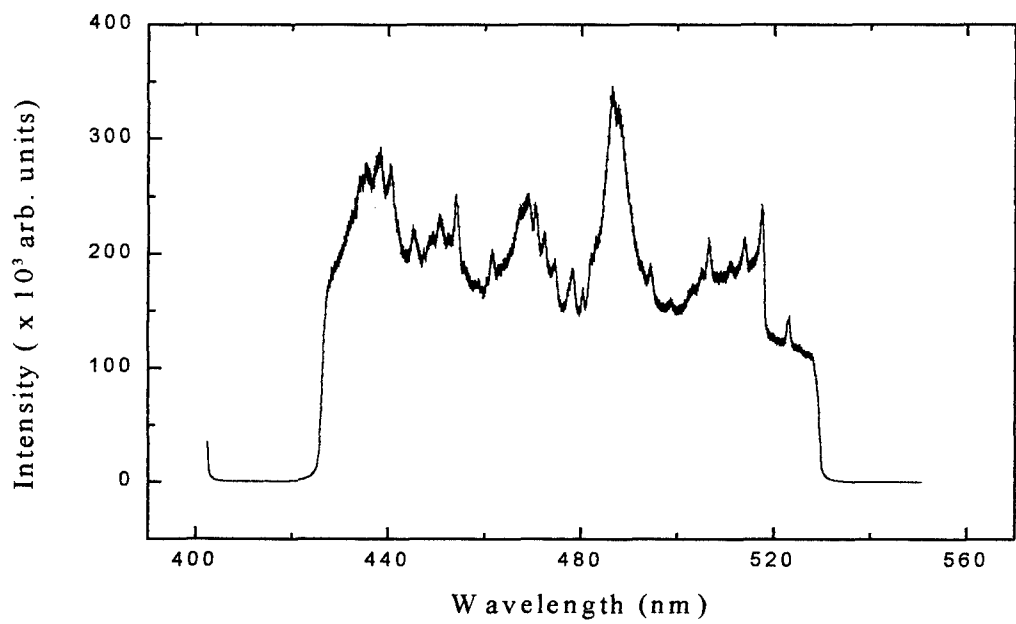


**Figure D.30**  $\text{CHCl}_3$  Spectrum Covering 425 - 525 nm (20  $\mu\text{m}$  slit width)

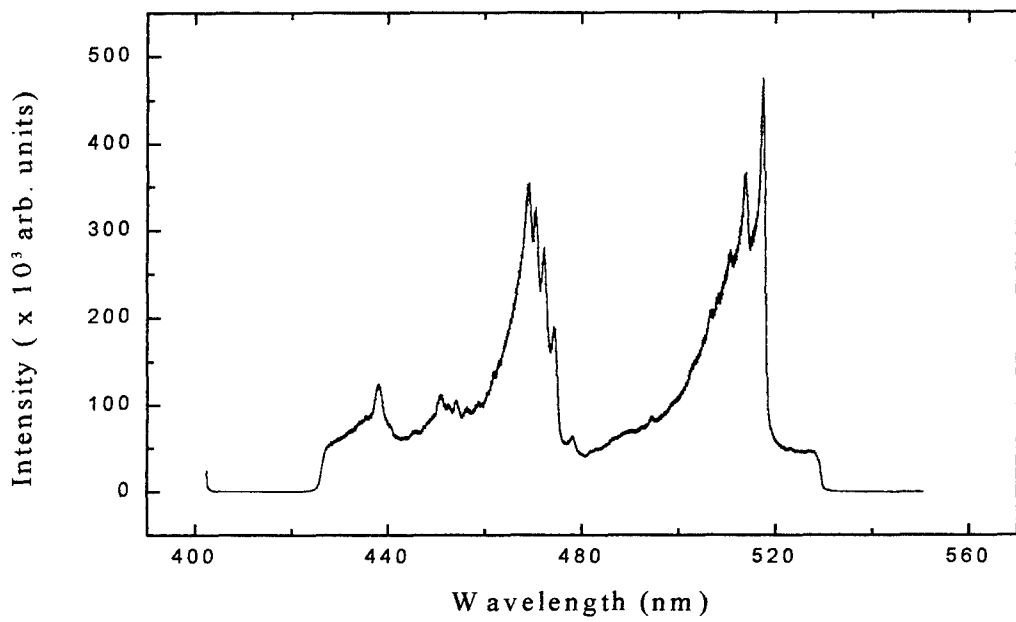


**Figure D.31**  $\text{C}_2\text{Cl}_4$  Spectrum Covering 425 - 525 nm

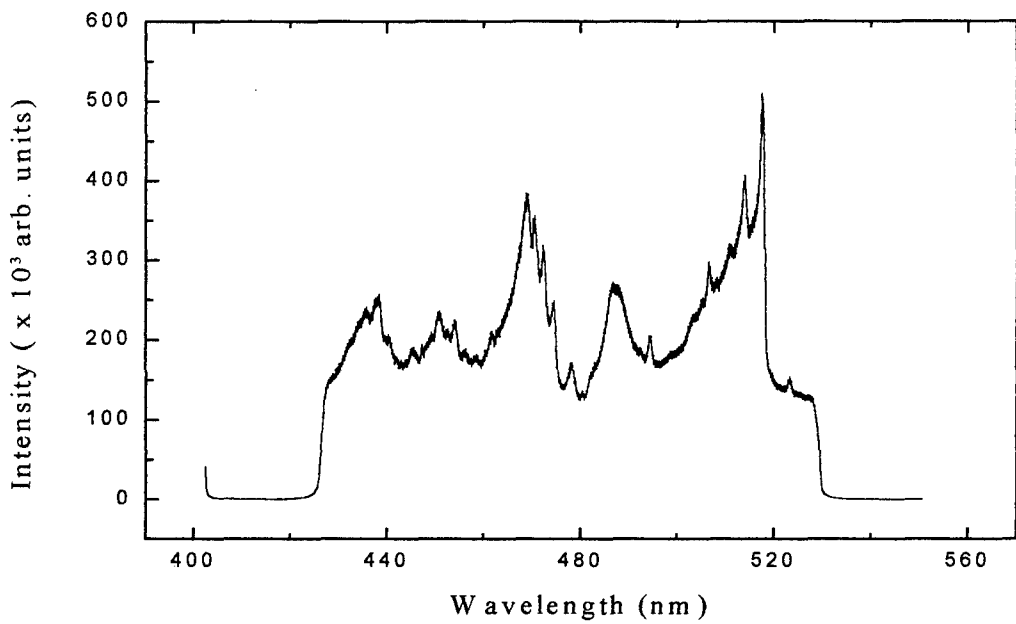


**Figure D.32**  $\text{C}_2\text{HCl}_3$  Spectrum Covering 425 - 525 nm

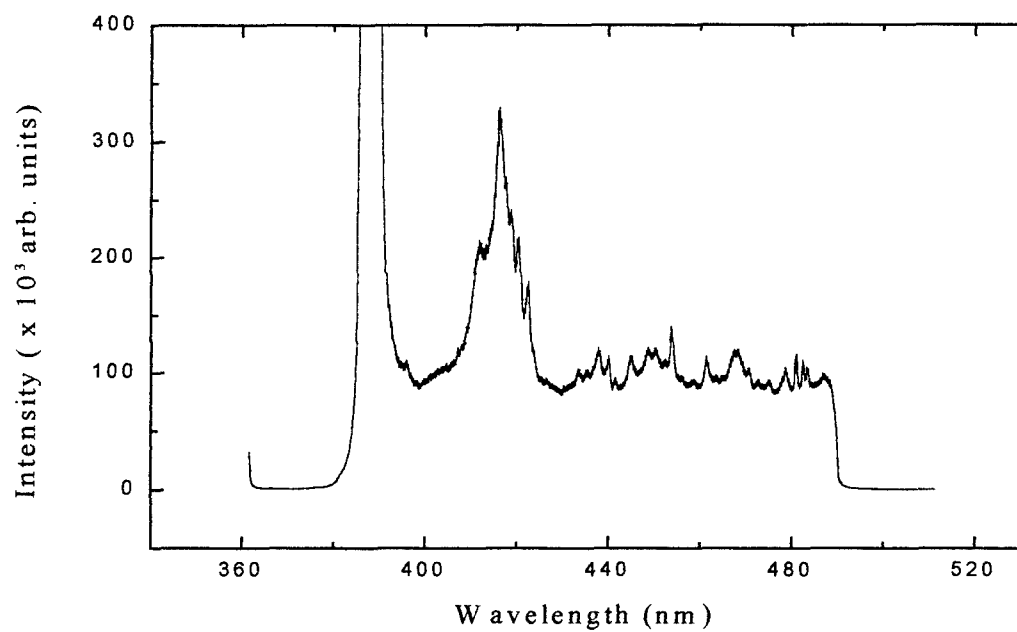


**Figure D.33 CCl<sub>4</sub> Spectrum Covering 385-485 nm (20  $\mu\text{m}$  slit width)**

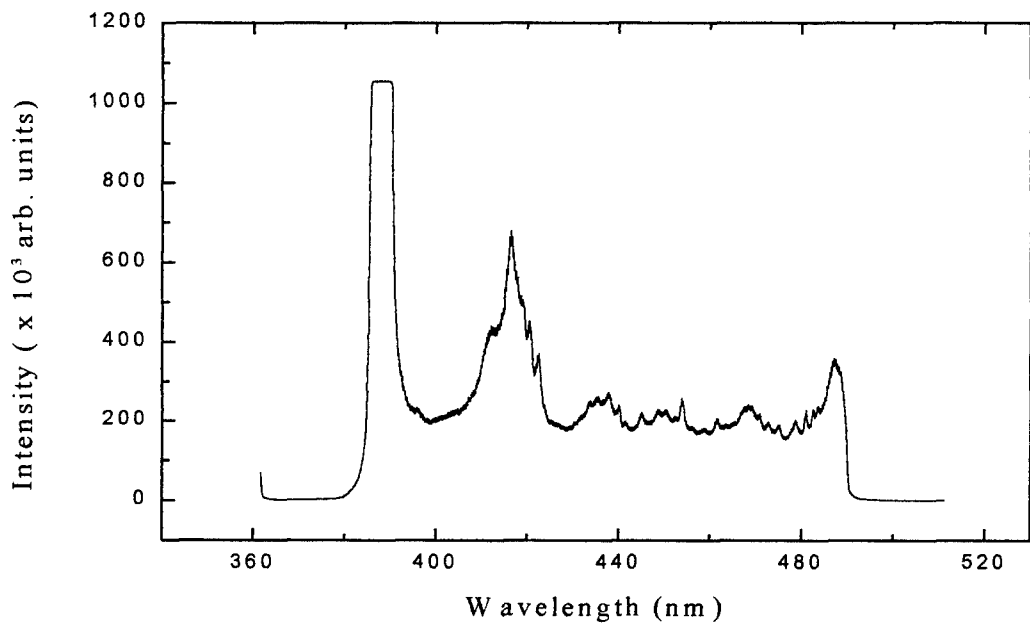


**Figure D.34 CHCl<sub>3</sub> Spectrum Covering 385 - 485 nm (20  $\mu\text{m}$  slit width)**

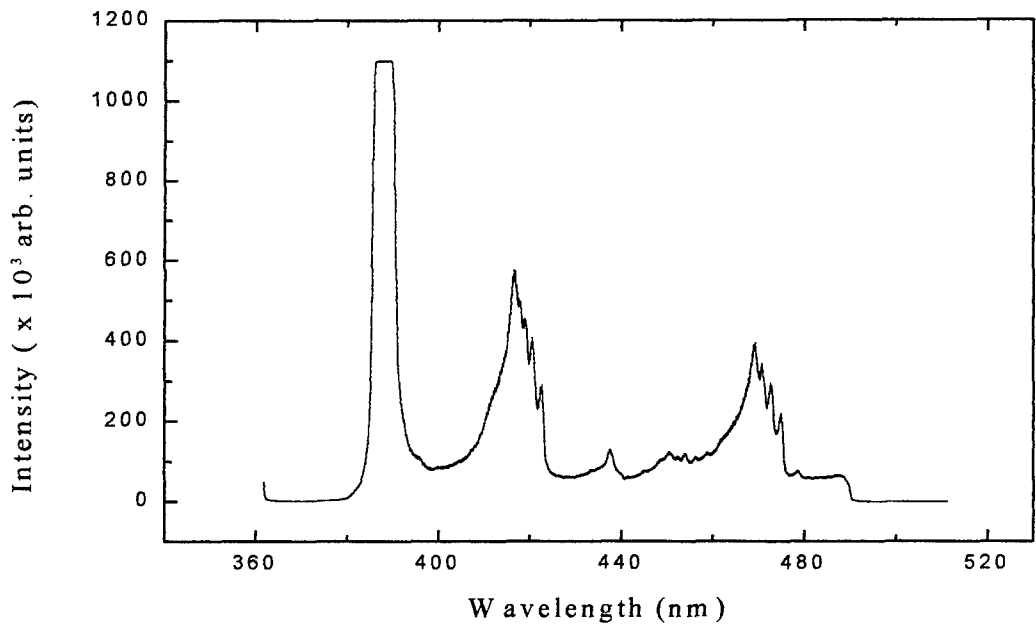


**Figure D.35**  $\text{C}_2\text{Cl}_4$  Spectrum Covering 385 - 485 nm

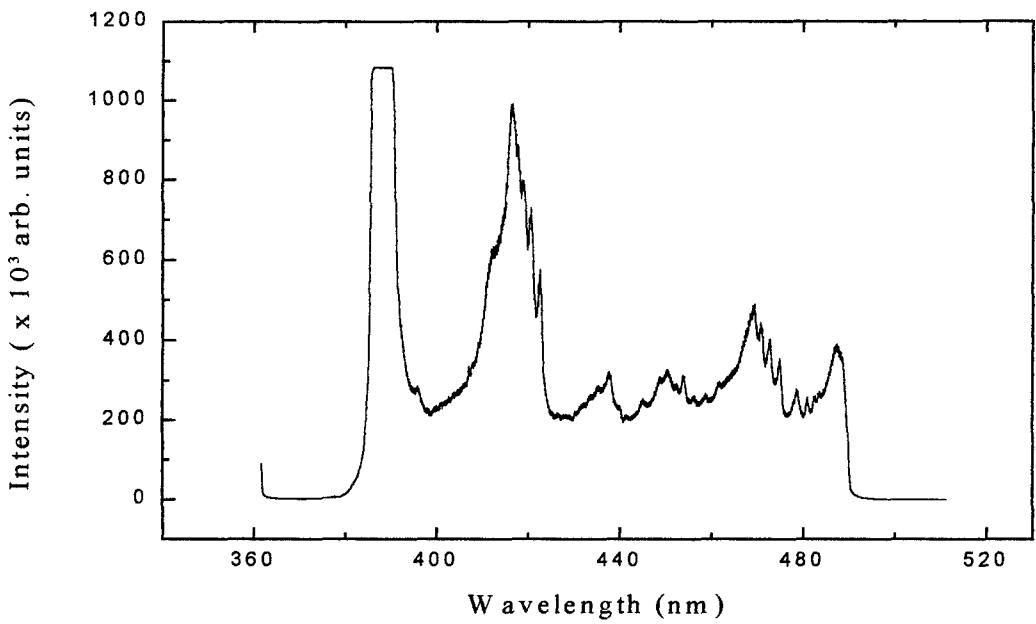


**Figure D.36**  $\text{C}_2\text{HCl}_3$  Spectrum Covering 385 - 485 nm

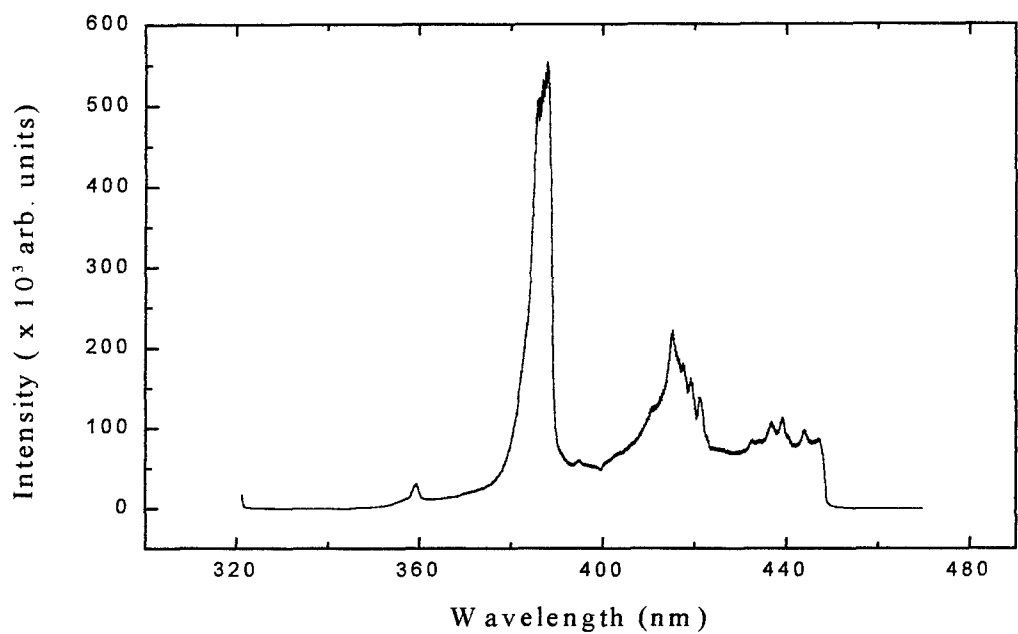


**Figure D.37 CCl<sub>4</sub> Spectrum Covering 345 - 445 nm (0.8 ND Filter)**

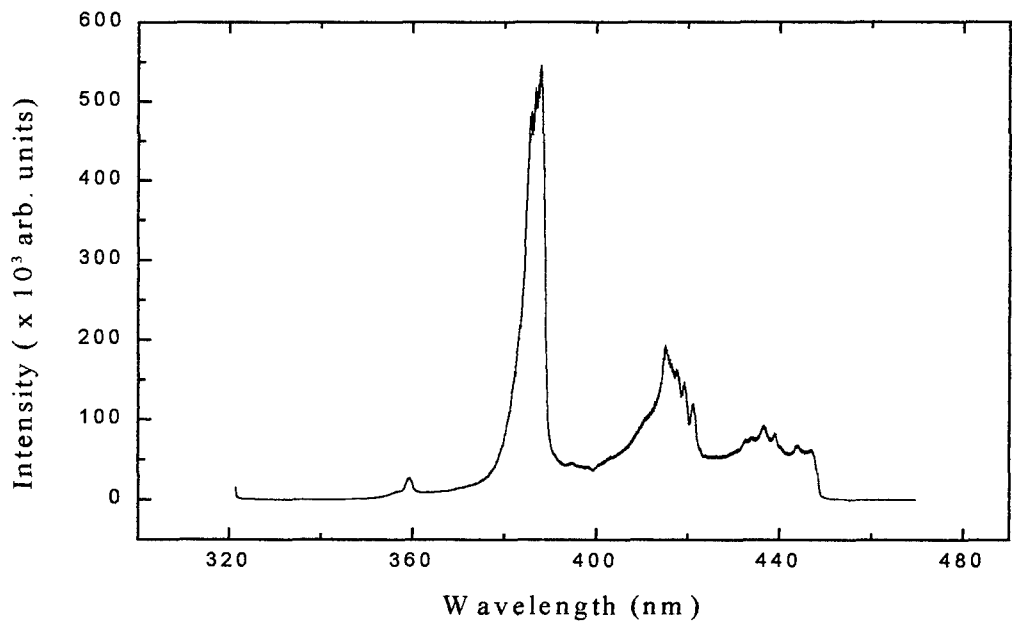


**Figure D.38 CHCl<sub>3</sub> Spectrum Covering 345 - 445 nm (0.8 ND Filter)**

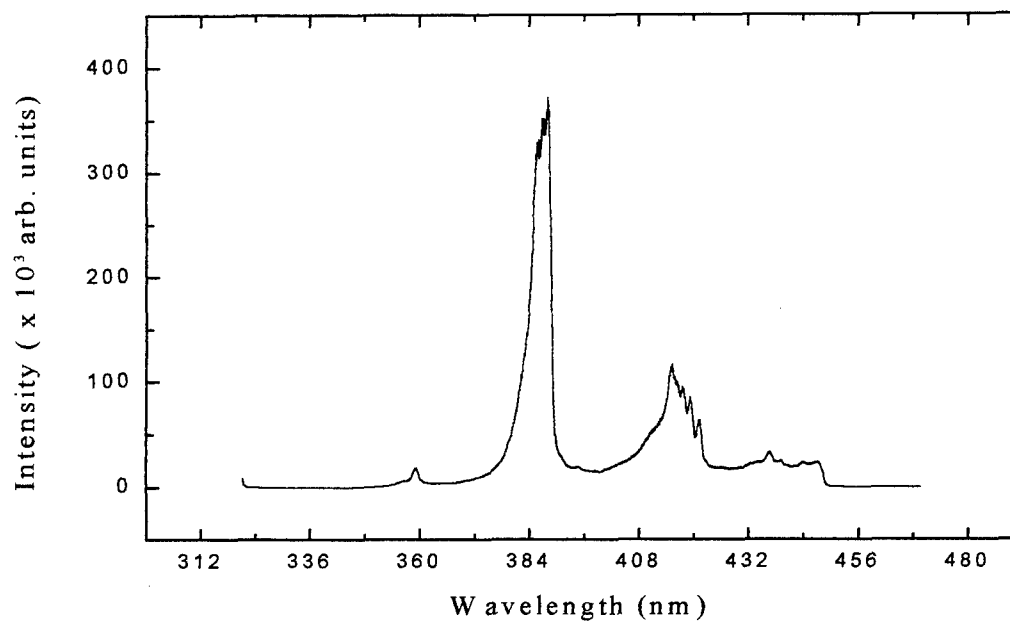


**Figure D.39  $\text{C}_2\text{Cl}_4$  Spectrum Covering 345 - 445 nm (0.8 ND Filter)**

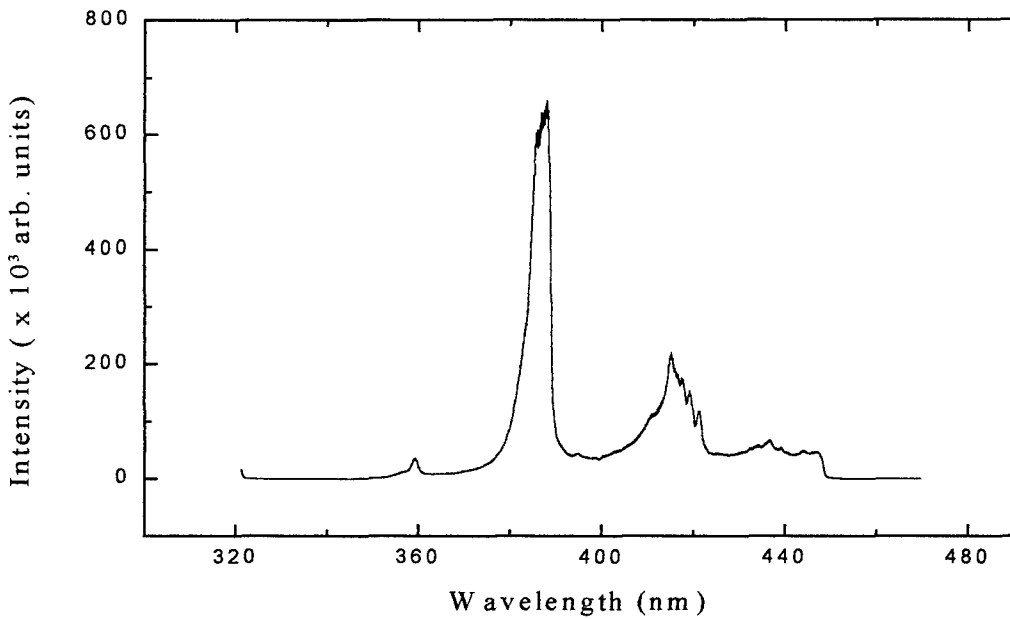


**Figure D.40  $\text{C}_2\text{HCl}_3$  Spectrum Covering 345 - 445 nm (0.8 ND Filter)**

## Appendix E - Bond Dissociation Energy

The bond dissociation energy for a molecule can be calculated from the heats of formation (enthalpy)  $\Delta H$  according to the following formula<sup>31</sup>:

$$\Delta H_{\text{reaction}} = \sum \Delta H_{\text{products}} - \sum \Delta H_{\text{reagents}} \quad (\text{E.1})$$

For the reaction (using data from Table E.1):  $\text{CCl}_4 \rightarrow \text{C} + 4\text{Cl}$

$$\Delta H_{\text{reaction}} = 311 \text{ kcal/mole}$$

For the reaction (using data from Table E.1):  $\text{C}_2\text{Cl}_4 \rightarrow \text{C}_2 + 4\text{Cl}$

$$\Delta H_{\text{reaction}} = 319 \text{ kcal/mole}$$

Table E.1 Heats of Formation for Several Atoms/Molecules

Atom/Molecule	Heat of Formation (kcal/mole) <sup>47</sup>
C	172
Cl	29.0
$\text{C}_2$	200
$\text{CCl}_4$	-22.9
$\text{C}_2\text{Cl}_4$	-2.70

## References

1. D.R. Alexander, D.E. Poulain, M.U. Ahmad, R.D. Kubic, and E.R. Cespedes, "Environmental Monitoring of Soil Contaminated with Heavy Metals Using Laser-Induced Breakdown Spectroscopy," in Proceedings of the IGARSS 1994 International Geoscience and Remote Sensing Symposium, (IEEE, New York, 1995) pp. 767-769.
2. R. Noll, R. Sattman, and V. Sturm, "Laser-Induced Breakdown Spectroscopy - A Versatile Tool for Process Control," SPIE **2248**, 50-62 (1994).
3. Paul J. Wolf (private communication).
4. R. Krska, K. Taga, and R. Kellner, "New IR Fiber-Optic Chemical Sensor for in Situ Measurements of Chlorinated Hydrocarbons in Water," Applied Spectroscopy **47** (9), 1484-1487 (1993).
5. Peter LaPuma, M.S. thesis, Air Force Institute of Technology (AU), 1994.
6. Kenneth J. Grant, George L. Paul, and James A. O'Neill, "Quantitative Elemental Analysis of Iron Ore by Laser-Induced Breakdown Spectroscopy," Applied Spectroscopy **45** (4), 701-705 (1991).
7. D.A. Cremers, "Overview of Applications of Laser-Induced Breakdown Spectroscopy (LIBS)," in Proceedings of the 6th International Congress on Applications of Lasers and Electro-optics ICALEO 1987, edited by G. Kychakoff (Springer-Verlag, Berlin, 1987), pp. 45-50.
8. David A. Cremers and Leon J. Radziemski, "Laser Plasmas for Chemical Analysis," in Laser Spectroscopy and Its Applications, edited by Leon J. Radziemski, R.W. Solarz, and J.A. Paisner (Marcel Dekker, New York, 1987), Chap. 5, pp. 351-415.
9. C. Lazzari, M. De Rosa, S. Rastelli, A. Ciucci, V. Palleschi, and A. Salvetti, "Detection of Mercury in Air by Time-Resolved Laser-Induced Breakdown Spectroscopy Technique," Laser and Particle Beams **12** (3), 525-530 (1994).

10. L.C. Jensen, S.C. Langford, J.T. Dickinson, and R.S. Addleman, "Mechanistic Studies of Laser-Induced Breakdown Spectroscopy of Model Environmental Samples," *Spectrochimica Acta Part B* **50**, 1501-1519 (1995).
11. R.S. Adrain and J. Watson, "Laser Microspectral Analysis: A Review of Principles and Applications," *Journal of Physics D: Applied Physics* **17**, 1915-1940 (1984).
12. C.M. Davies, H.H. Telle, D.J. Montgomery, and R.E. Corbett, "Quantitative Analysis Using Remote Laser-Induced Breakdown Spectroscopy (LIBS)," *Spectrochimica Acta Part B* **50**, 1059-1075 (1995).
13. N.F. Bunkin and F.V. Bunkin, "The New Concepts in the Optical Breakdown of Transparent Liquids," *Laser Physics* **3** (1), 63-78 (1993).
14. David A. Cremers and Leon J. Radziemski, "Detection of Chlorine and Fluorine in Air by Laser-Induced Breakdown Spectrometry," *Analytical Chemistry* **55** (8), 1252-1256 (1983).
15. M. Casini, M.A. Harinth, V. Palleschi, A. Salvetti, D.P. Singh, and M. Vaselli, "Time-Resolved LIBS Experiment for Quantitative Determination of Pollutant Concentrations in Air," *Laser and Particle Beams* **9** (2), 633-639 (1991).
16. Robert J. Nordstrom, "Study of Laser-Induced Plasma Emission Spectra of N<sub>2</sub>, O<sub>2</sub>, and Ambient Air in the Region 350 nm to 950 nm," *Applied Spectroscopy* **49** (10), 1490-1499 (1995).
17. J. Belliveau, L. Cadwell, K. Coleman, L. Huwel, and H. Griffin, "Laser-Induced Breakdown Spectroscopy of Steels at Atmospheric Pressure and in Air," *Applied Spectroscopy* **39** (4), 727-729 (1985).
18. David A. Cremers, "The Analysis of Metals at a Distance Using Laser-Induced Breakdown Spectroscopy," *Applied Spectroscopy* **41** (4), 572-579 (1987).
19. T.L. Thiem, R.H. Salter, J.A. Gardner, Y.I. Lewe, and J. Sneddon, "Quantitative Simultaneous Elemental Determinations in Alloys Using Laser-Induced Breakdown Spectroscopy (LIBS) in an Ultra-High Vacuum," *Applied Spectroscopy* **48** (1), 58-64 (1994).

20. Andrew V. Pakhomov, William Nichols, and Jacek Borysow, "Laser-Induced Breakdown Spectroscopy for Detection of Lead in Concrete," *Applied Spectroscopy* **50** (7), 880-884 (1996).
21. David A Cremers, Leon J. Radziemski, and Thomas R. Loree, "Spectrochemical Analysis of Liquids Using the Laser Spark," *Applied Spectroscopy* **38** (5), 721-729 (1984).
22. David J. Stolarski, Jennifer Hardman, Craig M. Bramlette, Gary D. Noonjin, Robert J. Thomas, Benjamin A. Rockwell, and W.P. Roach, "Integrated Light Spectroscopy of Laser Induced Breakdown Spectroscopy in Aqueous Media," *SPIE* **2391**, 100-109 (1995).
23. Joseph R. Wachter and David A. Cremers, "Determination of Uranium in Solution Using Laser-Induced Breakdown Spectroscopy," *Applied Spectroscopy* **41** (6), 1042-1048 (1987).
24. R.G. Gutmacher, D.A. Cremers, and J.R. Wachter, "Continuous Measurement of Uranium Concentrations with the Laser Spark," *Transactions of the American Nuclear Society* **55**, Suppl. 1, 19-20 (1987).
25. D.V. Vlasov, A.M. Prokhorov, D. Yu. Tsipenyuk, and P.I. Ivashkin, "Analytical Possibilities of Elemental Analysis of Water Solutions Based on the Emission Spectrum of a Laser Spark on the Surface," *Journal of Applied Spectroscopy* **55** (6), 1206-1213 (1991).
26. Ernesto R. Cespedes, Brian H. Miles, and Stephen H. Lieberman, "Development of Optical Sensors for the Site Characterization and Analysis Penetrometer System (SCAPS)," in Optical Sensing for Environmental Monitoring: Proceedings of an International Specialty Conference, (Air and Waste Management Association, Pittsburgh, 1994), pp. 621-632.
27. R. Knopp, F.J. Scherbaum, and J.I. Kim, "Laser Induced Breakdown Spectroscopy (LIBS) as an Analytical Tool for the Detection of Metal Ions in Aqueous Solutions," *Fresenius Journal of Analytical Chemistry* **355**, 16-20 (1996).
28. Typical Spectra of Oriel Spectral Calibration Lamps, (Oriel Corporation, Stratford, 1990), pp. 7-23.

29. John Kenkel, Analytical Chemistry for Technicians, (Lewis Publishers, Inc., Chelsea, Michigan, 1988), pp 70-71.
30. Rene P. Schwarzenbach, Philip M. Gschwend, and Dieter M. Imboden, Environmental Organic Chemistry, (John Wiley & Sons, Inc, New York, 1993), pg. 622.
31. Larry W. Burggraf (private communication).
32. J.R. Fuhr, G.A. Martin, W.L Wiese, and S.M Younger, "Atomic Transition Probabilities for Iron, Cobalt, and Nickel," *Journal of Physical Chemical Reference Data* **10** (2), 306-563 (1981).
33. H. Biehl and F. Stuhl, "Vacuum-Ultraviolet Photolysis of N<sub>2</sub>H<sub>2</sub>: Generation of NH Fragments," *Journal of Chemical Physics* **100** (1), 141-145 (1994).
34. R.W.B. Pearse and A.G. Gaydon, The Identification of Molecular Spectra, (Chapman and Hall, Ltd., London, 1976), pp. 103-106, 232-233.
35. Andrew D. Sappey and Jay B. Jeffries, "Detection of Cl in RF Plasmas by Laser-Excited Stimulated Emission," *Applied Physics Letters* **55** (12), 1182-1184 (1989).
36. W.L.Wiese, M.W. Smith, and B.M. Miles, Atomic Transition Probabilities: Volume II Sodium Through Calcium, (U.S. Department of Commerce, National Bureau of Standards, Washington D.C., 1969), pp. 158-170.
37. O.J. Orient, A. Chutjian, and K.E. Martus, "Observation of CN A→X and B→X Emissions in Gas-Phase Collisions of Fast O(<sup>3</sup>P) Atoms with HCN," *Physical Review A* **48** (1), 427-431 (1993).
38. Stanley Bashkin and John O. Stoner, Jr., Atomic Energy Levels and Grotrian Diagrams: Volume I Hydrogen I - Phosphorous XV, (North-Holland Publishing Company, Amsterdam, 1975), pp. 1-6, 100-130, 158-174.
39. Charlotte E. Moore, Atomic Energy Levels as Derived from the Analyses of Optical Spectra: Volume I, (U.S. Department of Commerce, National Bureau of Standards, Washington D.C., 1949), pp. 1-2, 32-37, 45-50.

40. J.B. Jeffries, G.A. Raiche, and L.E. Jusinski, "Detection of Chlorinated Hydrocarbons via Laser-Atomization/Laser-Induced Fluorescence," *Applied Physics B* **55**, 76-83 (1992).
41. CRC Handbook of Chemistry and Physics, 73<sup>rd</sup> Edition, edited by David R. Lide (CRC Press, Inc., Boca Raton, 1992), pp. 10-44, 49.
42. Kenneth J. Grant, George L. Paul, and James A. O'Neill, "Time-Resolved Laser-Induced Breakdown Spectroscopy of Iron Ore," *Applied Spectroscopy* **44** (10), 1711-1714 (1990).
43. Terry L. Thiem and Paul J. Wolf, "Analysis of National Institute of Standards and Technology Ore and United States Geological Survey Samples by Inductively Coupled Plasma Spectroscopy/Laser-Induced Breakdown Spectroscopy," *Microchemical Journal* **50**, 244-252 (1994).
44. Helen A. Archontaki, PhD dissertation, Michigan State University, 1987.
45. D.L. Bauch, J. Duxbury, S.J. Grant, and D.C. Montague, "Evaluated Kinetic Data for High Temperature Reaction," *Journal of Physical and Chemical Reference Data* **10**, Suppl. 1, 140-144 (1981).
46. Glen P. Perram (private communication).
47. James J.P. Stewart, MOPAC 93 Manual, (Fujitsu Limited, 1993), pp. 229, 238, 240.
48. Douglas A. Skoog, Donald M. West, and F. James Holler, Fundamentals of Analytical Chemistry, (Saunders College Publishing, Fort Worth, 1992), pp. 13-15.

**Vita**

**Leonard M. Berman** [REDACTED]

[REDACTED] Shortly thereafter, his family moved to Peoria, IL. After graduating from Richwoods H.S., Leonard enrolled in Illinois Central College. He later graduated in May 1985 with an A.A.S. After this, Leonard enrolled in Southern Illinois University (SIU) to continue his education in physics. He graduated with a B.S. in Physics in December 1987 and soon enrolled into the graduate program at SIU. Being unfulfilled, Leonard applied to OTS for admission. On August 8, 1989, Leonard reported for duty at Lackland AFB, TX. A few months later, he was commissioned a 2nd Lieutenant. Upon completion of his first assignment (Basic Meteorology Program), Leonard was sent to Scott AFB, IL as a Weather Forecaster for the MAC Weather Support Unit. While at Scott AFB, Leonard completed his second Bachelors, a B.S. in Meteorology from Texas A&M University. His next assignment was at Osan AB, Korea where he provided aircrew support as a Wing Weather Officer. After this, Leonard accepted an assignment to Barksdale AFB, LA as a Weather Plans Officer. Sixteen months into his tour, Leonard left for an assignment to AFIT where he is currently working on an M.S. in Applied Physics.

[REDACTED]  
P[REDACTED]

## **REPORT DOCUMENTATION PAGE**

*Form Approved*  
OMB No. 0704-0188

Public reporting burden for this collection of information is estimated to average 1 hour per response, including the time for reviewing instructions, searching existing data sources, gathering and maintaining the data needed, and completing and reviewing the collection of information. Send comments regarding this burden estimate or any other aspect of this collection of information, including suggestions for reducing this burden, to Washington Headquarters Services, Directorate for Information Operations and Reports, 1215 Jefferson Davis Highway, Suite 1204, Arlington, VA 22202-4302, and to the Office of Management and Budget, Paperwork Reduction Project (0704-0188), Washington, DC 20503.

1. AGENCY USE ONLY (Leave blank)	2. REPORT DATE December 1996	3. REPORT TYPE AND DATES COVERED Master's Thesis	
4. TITLE AND SUBTITLE  Laser-Induced Breakdown Spectroscopy on Solution Samples Using Surface Excitation		5. FUNDING NUMBERS	
6. AUTHOR(S) Leonard M. Berman, Capt, USAF			
7. PERFORMING ORGANIZATION NAME(S) AND ADDRESS(ES)  Air Force Institute of Technology 2750 P Street WPAFB OH 45433-6583		8. PERFORMING ORGANIZATION REPORT NUMBER  AFIT/GAP/ENP/96D-03	
9. SPONSORING / MONITORING AGENCY NAME(S) AND ADDRESS(ES)  U.S. Army Corps of Engineers Waterways Experiment Station (CEWES-EE-S) 3909 Halls Ferry Road Vicksburg, MS 39180		10. SPONSORING / MONITORING AGENCY REPORT NUMBER	
11. SUPPLEMENTARY NOTES			
12a. DISTRIBUTION / AVAILABILITY STATEMENT  Approved for public release; distribution unlimited		12b. DISTRIBUTION CODE	
13. ABSTRACT (Maximum 200 words)  Laser-induced breakdown spectroscopy (LIBS) is a spectroscopic technique where output from a pulsed laser is focused onto a target in order to create an intense plasma. The optical emission is characteristic of the elements in the focal volume and can be used for elemental analysis. Research on the detection of nickel in solution in addition to solvent detection of CCl <sub>4</sub> , CHCl <sub>3</sub> , C <sub>2</sub> Cl <sub>4</sub> , and C <sub>2</sub> HCl <sub>3</sub> has been performed. Breakdown was formed at the sample surface via a Q-switched Nd:YAG laser. Initially, operation of the laser was at 1064 nm/repetition rate of 5 Hz. Experiments were also performed using the third harmonic (355 nm)/repetition rate of 20 Hz. Pulse energy was maintained at 60 mJ. The spark light was spectrally resolved and detected by a time-gated photodiode array. A 50 µs gate width/8 µs time delay gave detection limits of 56.1 mg/l for nickel in solution. In the UV, a 10 µs gate width/3 µs time delay lowered detection limits down to 29.4 mg/l. Concentrations spanned from 50 to 1000 mg/l. Using UV excitation (10 µs gate width/1 µs time delay), saturated solvent solutions as high as 7.71 g/l were not detectable.			
14. SUBJECT TERMS  Emission Spectroscopy, Laser Spark, Spectrochemistry Laser Microspectral Analysis, Optical Breakdown		15. NUMBER OF PAGES 97	
		16. PRICE CODE	
17. SECURITY CLASSIFICATION OF REPORT Unclassified	18. SECURITY CLASSIFICATION OF THIS PAGE Unclassified	19. SECURITY CLASSIFICATION OF ABSTRACT Unclassified	20. LIMITATION OF ABSTRACT UL